IS-T--1506

DE91 009867

Hydrogen Diffusion and Microstructure in Undoped and Boron-dope Hydrogenated Amorphous Silicon: An IR and SIMS Study

by

Mitra, Saibal

PHD Thesis submitted to Iowa State University

Ames Laboratory, U.S. DOE

Iowa State University

Ames, Iowa 50011

Date Transmitted: March 12, 1991

PREPARED FOR THE U.S. DEPARTMENT OF ENERGY

UNDER CONTRACT NO. W-7405-Eng-82.

---

the hydrogen vibrational modes. The ESR gave information on the number of paramagnetic defects per unit volume in the samples.

The IR absorption of both as-deposited and annealed samples were closely monitored and the results clearly demonstrate a strong correlation between hydrogen diffusion and its microstructure. It is shown that microvoids in a-Si:H play a critical role in the process of diffusion by inducing deep hydrogen trapping sites that render them immobile. Consequently, as the microvoid density increases beyond a critical density (corresponding to $N_d \geq 6.5$ at. %) hydrogen diffusion is totally quenched. The diffusion results are discussed both in the context of multiple trapping transport of hydrogen in an exponential distribution of trapping sites and the floating bond model.

As expected the hydrogen diffusion in boron-doped a-Si:H is faster than undoped material by a few orders of magnitude. The diffusion results have shown a significant departure from the power-law time dependence upon prolonged annealing. Such a departure has not been reported before. It is suspected that this deviation is caused by structural relaxations of the silicon network.

Hydrogen Diffusion and Microstrucure in Undoped and Boron-doped Hydrogenated Amorphous Silicon: An IR and SIMS study

Saibal Mitra*

Under the supervision of Joseph Shinar

From the Department of Physics

Iowa State University

Hydrogenated amorphous silicon (a-Si:H) prepared by rf sputtering of a polycrystalline Si target at various rf powers $50 \leqslant P \leqslant 550$ W (0.27 - 2.97 W/cm^2), target to substrate distance $1 \leqslant d \leqslant 2$", and varying hydrogen partial pressures. Doping was accomplished by introducing diborane (B_2H_6) in the plasma. Hydrogen diffusion was studied from the depth profiles obtained from the SIMS on multilayered a-Si:H/a-Si:(H,D)/a-Si:H samples.

The properties of the samples were characterized by IR absorption, optical gap measurements and ESR. IR yielded quantitaive and qualitative information total hydrogen content and the nature of hydrogen bonding, respectively. Hence the hydrogen microstructure of the samples could be varied in a systematic manner and monitored from

---

*DOE Report IS-T-1506. This work was performed under contract No W-7405-Eng-82 with US Department of Energy.

TABLE OF CONTENTS

I. INTRODUCTION 1

A. A Brief Historical Background 1
B. Some Basic Features of Amorphous Semiconductors ...2
C. Role of Hydrogen 9
D. Stability and its Relation to Hydrogen Motion 13
1. The Staebler-Wronski Effect 13
2. Hydrogen motion in amorphous silicon 15
E. Scope of this Work 21

II. SAMPLE PREPARATION 23

III. SAMPLE CHARACTERIZATION 36

A. Thickness Measurements 36
B. Optical Measurements 36
C. Infrared Absorption 43
D. Electron Spin Resonance Measurements 50
E. Secondary Ion Mass Spectrometry 53

IV. RESULTS AND DISCUSSION 63
A. General Comments 63
B. Undoped a-Si:H 67
1. Sample characterization 67
2. Hydrogen diffusion results 77
C. Boron-doped a-Si:H 110
D. Concluding Remarks 120

V. REFERENCES 124

VI. ACKNOWLEDGEMENTS 129

I. INTRODUCTION

A. A Brief Historical Background

Solid state physics has been primarily concerned with the study of crystalline materials. As a result the physics and the technology of crystalline semiconductors is both well understood and highly developed. Over the past two decades, however, amorphous semiconductors have attracted increasing attention. This is due to the significant advances made in material preparation and the resulting lower cost and improved performance of amorphous semiconductor-based devices.

Hydrogenated amorphous silicon (a-Si:H) has now become the leading material in photovoltaic devices (e.g., solar cells) and is extensively used in xerographic copiers, thin film transistors (TFT), photodetectors, image sensors and optical mass memories.[1,2]

Amorphous silicon (a-Si) films were first deposited by the glow discharge decomposition of silane (SiH_4) by Chittick, Alexander and Sterling in 1969.[3] Early attempts to dope a-Si films failed. These samples had a large number of mid-gap states induced by three-fold coordinated Si "dangling bond" (db) defects effectively pinning the Fermi level at this energy. In 1975, Spear and LeComber[4] were able to dope a-Si both n- and p-type by addition of phosphine (PH_3) and diborane (B_2H_4) respectively. They did not, however, realize the crucial role played by hydrogen in this mechanism. In 1976, Paul et al. demonstrated that rf sputter deposited a-Si could be doped both n- and p-type when hydrogen was added to the plasma.[5] Hydrogen passivates almost all of the unsaturated dangling bonds and thus drastically lowers the mid-gap

density of states. The Fermi level can then be moved in either direction by doping. With the discovery that a-Si:H could be easily doped interest grew rapidly.

B. Some Basic Features of Amorphous Semiconductors

In crystalline materials all the atoms are placed in a periodic array with the bond lengths and bond angles between neighbouring atoms fixed. Crystalline silicon (c-Si), for example, is tetrahedrally coordinated having a bond length of 2.45 Å between neighbouring atoms and a bond-bond angle of $109^{o}30'$. Since these values are fixed, crystalline materials have not only short range order (SRO) but also long range order (LRO). One of the most important consequences of an electron moving in a periodic potential is the Bloch theorem in which the electronic wavefunction is forced to have the periodicity of the host crystal. This gives rise to an energy band structure of the electrons where the allowed energies are separated by gaps of forbidden energies.[6] As an example, c-Si is an indirect band gap material with an energy gap (E_g) of 1.12 eV.

Amorphous semiconductors are noncrystalline in the sense that they lack the LRO of their crystalline counterpart. Their X-ray diffraction pattern consists of diffuse rings rather than the sharply defined Bragg spots or rings characteristic of either single crystals or polycrystalline silicon. Though LRO is absent in both a-Si and a-Ge, SRO does indeed exist and this has been demonstrated by the experimental determination of the radial distribution function (RDF). The RDF, $J(r) = 4\pi r^2 \rho(r)$, is defined as the average number of atoms present in a thin

spherical shell of radius r and thickness dr with the center of the shell on an arbitrary atom. $\rho(r)$ is the density. The importance of $J(r)$ lies in the fact that it gives real space structural information on the values of both bond lengths and bond angles. The position of the peaks depends on the distance between the nearest neighbor (nn), next nearest neighbor (nnn) atoms and so on while the area under the peaks depends on the average coordination number. The RDF for a-Ge, as determined by Temkin and coworkers[7], is compared with that of c-Ge and is shown in Figure 1.1. The position and the sharpness of the first peak (nn distance) is identical in both cases implying that the bond lengths in a-Ge are similar to those of c-Ge and demonstrating the presence of SRO. The width of the first peak is caused only by thermal vibrations in the case of c-Ge, whereas additional broadening due to the presence of static disorder is present in the case a-Ge. The subsequent peaks become broader and less well defined with increasing r and are superimposed on the "average density parabola" given by $4\pi r^2\rho$. At large values of r the peaks tend to disappear and the RDF merges with the background since there are no long range atomic correlations. Knowledge of the nn and the nnn distance immediately gives the value of the bond angles which is given by

$$\theta = 2 \sin^{-1}(r_2/2r_1) \qquad 1.1$$

Here r_1 and r_2 are the nn and the nnn distances respectively. The width of the second peak is more smeared in the case of a-Ge reflecting the presence of a static variation in the bond angles (of the order of $\pm 10\%$) in addition to the thermal disorder. It is clear that in a-Ge (and similarly in a-Si), it is the variations of bond angles, rather than

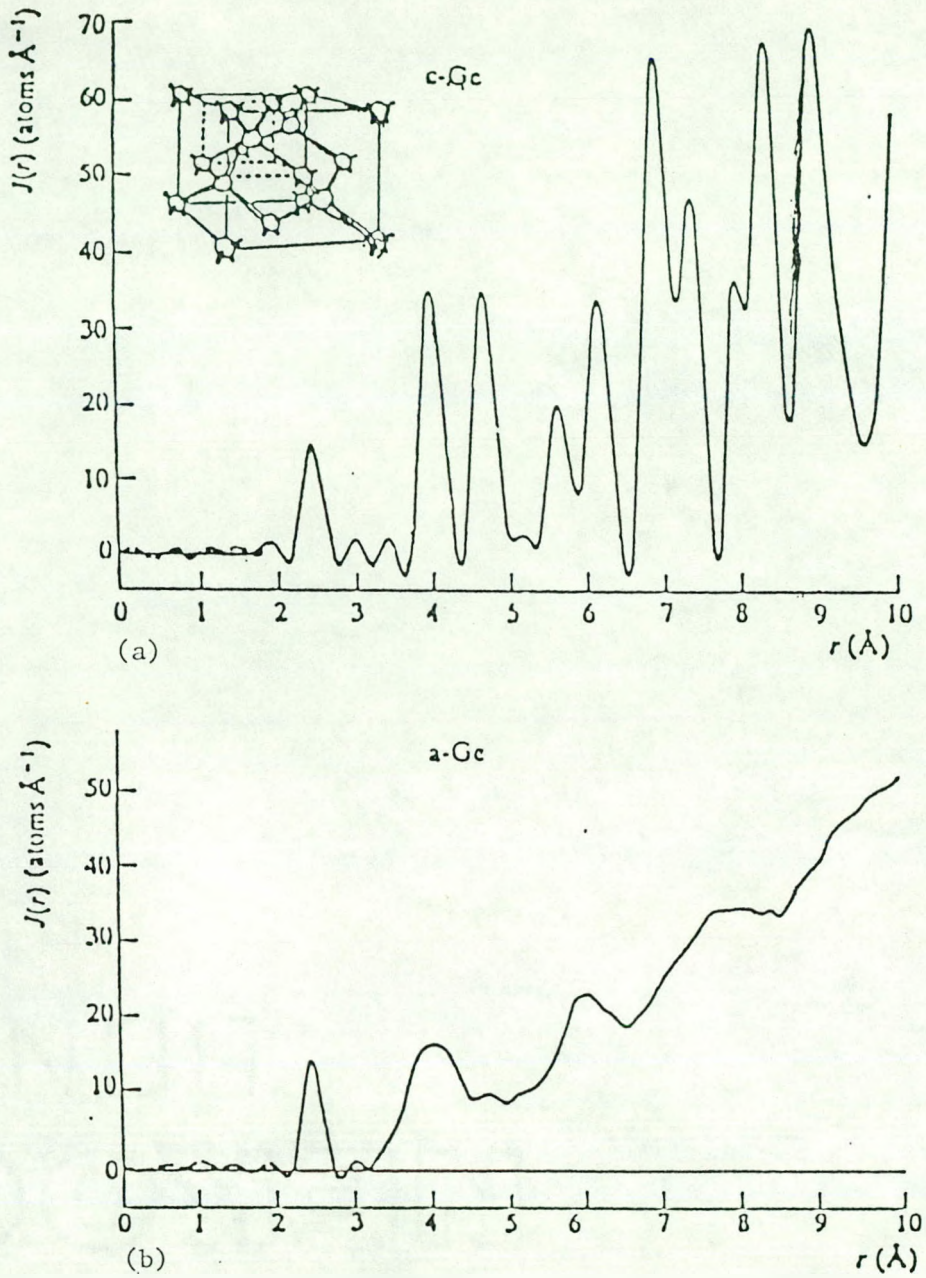

Fig. 1.1 X-ray derived RDFs for (a) crystalline Ge (with inset of diamond cubic lattice, and (b) amorphous Ge films (from ref. 7)

those of bond lengths, that contribute most to the positional disorder of atoms in these materials. Table I summarizes these differences for crystalline and amorphous silicon.

One of the most important consequences of the lack of long range order is in the energy band diagram. The electronic wave vector, **k**, is now no longer a good quantum number and hence the Bloch theorem no longer holds. However, as in crystalline semiconductors, the density of states N(E) in amorphous semiconductors can still be defined as the number of states per unit volume between E and E + dE. Due to the lack of LRO, the sharp features in the density of states, called the Van Hove singularities, are smeared out. Consequently, both a-Si and a-Ge effectively become direct band gap materials. Indeed, c-Si has an indirect gap of 1.12 eV while a-Si has a direct gap of about 1.4 eV. Yet optical absorption and photoconductivity measurements have shown the existence of many states in the gap of a-Si and a-Ge (Figure 1.2), which almost masks the gap.

Since the environment around each atom is different due to disorder, the Si-Si bond strengths vary. Some bonds are stretched and hence are weak. Others are weakened by severely distorted bond angles. These weak Si-Si bonds generate localized tail states, mostly in the top of the valence band where the electronic wavefunction is spatially confined in the vicinity of one atom. These states extend well into the mobility gap and were first theoretically described by Anderson.[8] The separation in energy between the delocalized states in the valence and the conduction band is called the mobility gap and is always smaller than the optical gap, E_g (see below). The decay constant of the density of

Table I. Structural Characteristics of the Continous Distorted Network (from K. Winer, Phys. Rev. B 35, 2366 (1987)

	ρ/ρ_o	Δr_{rms}	$\Delta\theta_{rms}$	ΔE (eV/atom)
F-2 Si	1.00	0.0%	0.0%	0.00
Keating ($\beta/\alpha = 0.285$)	1.04	2.6%	11.3°	0.32
Weber ($\beta/\alpha = 0.300$)	1.03	2.2%	11.3°	0.20
Experiment	0.90	1.6%	9.7°	0.25

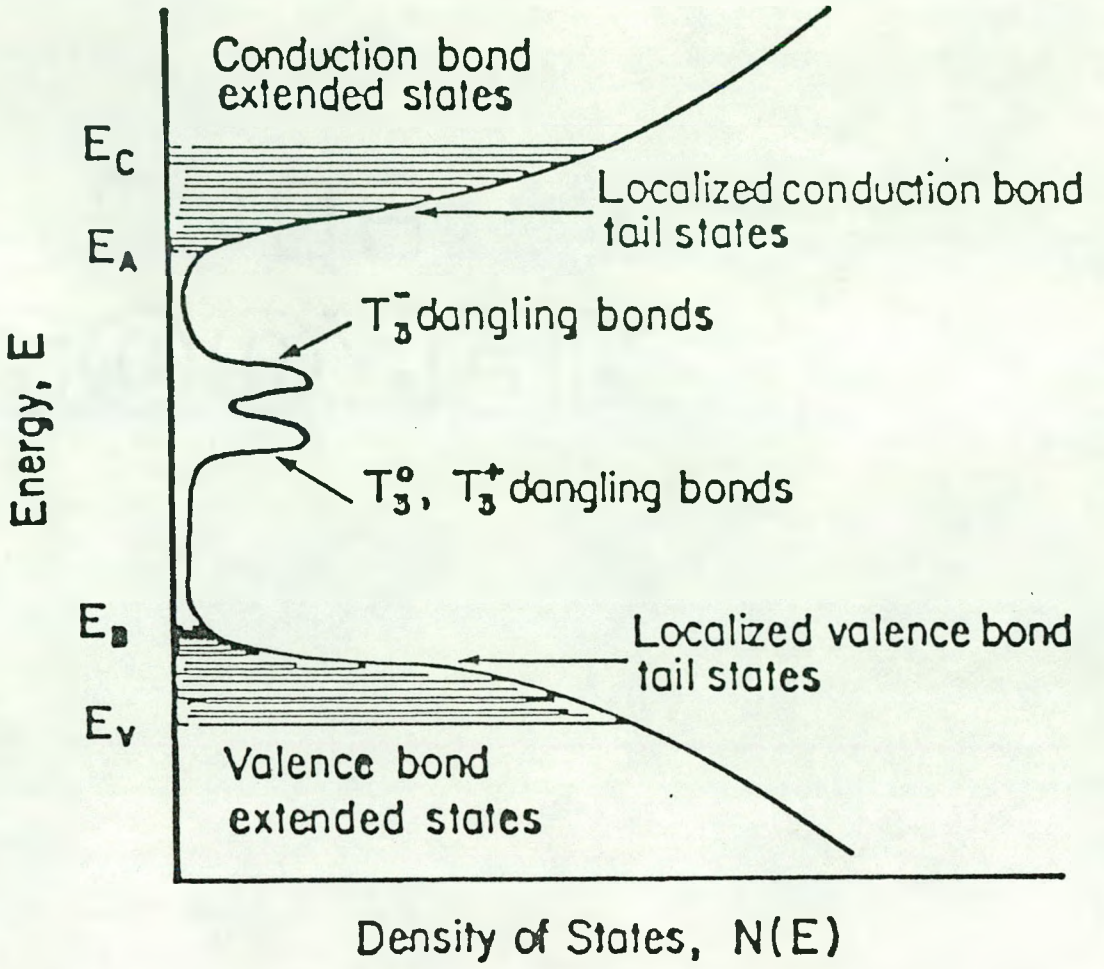

Fig. 1.2 Davis-Mott model of the electronic density of states in amorphous silicon

tail states decaying into the gap is a measure of the SRO and is defined by the Urbach energy E_o. It is directly measurable from absorption experiments. When photons with energies less than the optical gap are incident on the sample, bandtail to bandtail transitions dominate. The absorption coefficient $\alpha(E)$ can be written as

$$\alpha(E) = \alpha_o \exp\{(E - E')/E_o\} \qquad 1.2$$

where α_o, E_o and E' are material-dependent constants and E' has a value close to the optical gap. A large value of E_o indicates greater disorder and a larger density of tail states that extends deeply into the gap.

Another consequence of disorder is the presence of dangling bonds states ($T_3^{0,\pm}$). Here T denotes tetrahedral bonding, the subscript denotes coordination number and the superscript is the charge. A dangling bond is an sp^3 orbital that remains unpaired and hence attached to an undercoordinated silicon atom. The T_3^0 dangling bond has one electron in its orbital and is electrically neutral. Since the electron remains unpaired, it has a strong ESR signature. The g-value is experimentally found to be 2.0055. The T_3^- state is doubly occupied and has a net negative charge and no ESR signal. Since the correlation energy U, which is the energy required to put an extra electron in a neutral dangling bond, is positive,[9] the T_3^- state is located by an amount U higher above the T_3^0 state in the energy band diagram.

Recently, Pantelides[10] suggested that fivefold overcoordinated Si defects should be treated on an equal footing with the threefold dangling bonds. The fifth bond, called a floating bond, has a lone unpaired electron in the neutral state and hence also an ESR signature.

These floating bonds, however, should be mobile, moving from one silicon site to another simply by switching bonds. The migration of the floating bonds and the creation and annihilation of both floating and dangling bonds is schematically shown in Figure 1.3. A more detailed description of the various reactions involving the floating bonds is described later in this chapter.

Kelires and Tersoff[11] simulated the formation of a-Si by rapid quenching of the liquid. Their calculations suggest that the formation energy of the floating bond is broadly distributed about ~ 0.3 eV while that of the dangling bond peaks at ~ 0.6 eV. Pantelides[12] has suggested a value of 0.6 and 0.8 eV for the formation energy of fivefold and threefold defects respectively, while Bar-Yam, Adler, and Johannopoulos[13] have suggested a value of 0.7 eV for the formation energy of the paramagnetic defect (which they assumed to be threefold coordinated). Biswas, Grest, and Soukoulis[14] have also reported the formation of an equal number of floating and dangling bonds based on their molecular dynamics simulations of unhydrogenated amorphous silicon prepared by quenching from the melt.

C. Role of Hydrogen

Addition of hydrogen to both amorphous silicon and germanium greatly improves their opto-electronic properties. In both a-Si and a-Ge, large dangling bond defect densities result in poor opto-electronic properties. Incorporation of hydrogen significantly lowers the density of dangling bond states by forming Si-H bonds. This is clearly seen from the sharp drop in the ESR signal when hydrogen is added. In

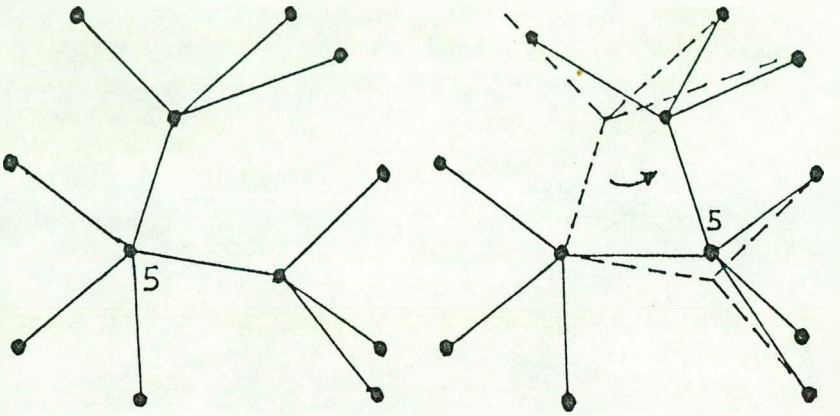

(a)

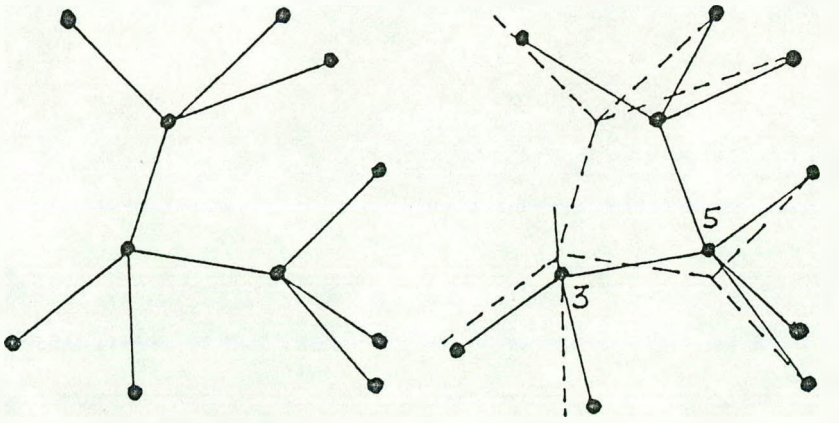

(b)

Fig. 1.3 Schematic illustration of (a) floating bond migration by bond switching, and (b) dangling- and floating-bond pair creation by bond switching (from ref. 12)

unhydrogenated a-Si, the typical spin density is ~ 10^{19}-10^{20} cm^{-3} while in device quality a-Si:H it is ~10^{15} cm^{-3}. The reduction in the midgap state density has two major beneficial effects. First, the Fermi level is no longer pinned and the material can be easily doped either n- or p-type. While there is no discernible effect in a-Si and a-Ge, doping increases the conductivity of a-Si:H and a-Ge:H by many orders of magnitude. Secondly, the midgap states also act as non-radiative recombination centers for both electrons and holes. Hence addition of hydrogen also vastly improves the opto-electronic properties of both a-Si/Ge by reducing the density of recombination centers and increasing the lifetime of excess carriers. Both photoluminescence and photoconductivity are easily observable in a-Si:H. A detailed comparison between a-Si and a-Si:H is given in Table II.

Addition of hydrogen also increases the energy gap of the material and produces sharper band tail edges.[15,16] The energy gap (E_g) of a-Si:H increases continuously from 1.4 eV to 2.0 eV with increasing content of hydrogen and is attributed to the silicon-hydrogen alloying effect. The tail states arise from the disorder in the material and are thought to be caused by (a) weak Si-Si bonds (b) microvoids and columnar morphology and (c) SiH_x complexes.

The origin of the weak Si-Si bonds is attributed to the variations in the local bond lengths and angles. Addition of hydrogen reduces these variations.[17] The addition of hydrogen in the plasma also yields some silicon atoms that are bonded to more than one hydrogen atom. The fact that one gets di- and tri-H bonds is to be expected from simple statistical considerations and Albers[18] has shown that the number of

Table II. A comparison of the properties of nominally pure and hydrogenated amorphous silicon

	Pure	Hydrogenated
Dangling Bonds	5×10^{19} cm^{-3}	$<10^{15}$ cm^{-3}
States in the gap	$10^{19} - 10^{20}$ cm^{-3} eV^{-1}	$10^{16} - 10^{17}$ cm^{-3} eV^{-1}
Conductivity	Hopping at Fermi Level $\exp[-(T_o/T)]^{1/4}$	Activated to Band or Band Tail $\exp(-\Delta E/kT)$
Optical Absorption	Tails into Infrared	Edge near 1.7 eV
Photoresponse	None	Photoconductive Photoluminescent
Doping Effects	Not Discernible	p- or n-type. Conductivity changes upto 10^{10} times.

silicon atoms with di-H bonds generally increases as the square of the total hydrogen content. The presence of microvoids and columnar morphologies has been correlated to the SiH_2 and SiH_3 complexes.[19-22] The formation of these complexes is thought to occur on the surfaces of these structural defects and hence it is difficult to separate the effect of one from the other. It has been demonstrated by Ross and Meisser[19,20] and Knights and his coworkers[21,22] that the surface area of these defects is proportional to the amount of SiH_2/SiH_3 complexes. It has been suggested by Albers[18] that some of the tail states are due to weakly reconstructed Si-Si bonds on surfaces of microvoids and columns.

D. Stability and its Relation to Hydrogen Motion

1. The Staebler-Wronski Effect

One of the outstanding problems in the physics and technology of a-Si:H is the reversible light induced degradation of a-Si:H known as the Staebler-Wronski Effect (SWE). In 1977, Staebler and Wronski[23] showed that the photoconductivity σ_{ph} and the dark conductivity σ_d of glow discharge deposited a-Si:H were reduced considerably upon illumination with intense light. While σ_{ph} was reduced by a factor of eight, σ_d decreased by four orders of magnitude. Upon annealing for 4 hours at 150°C, both σ_d and σ_{ph} recovered their original values and the entire cycle could be repeated. The obvious technological significance of the SWE has promoted considerable effort among scientists and engineers towards its resolution.

It should be pointed out that the process of illumination itself does not create defects in the midgap region. Rather the electron-hole pairs that are generated during illumination undergo nonradiative band-tail to band-tail recombination and sometimes the energy thus released creates these defects.[24] It is largely accepted that these defects, induced either by illumination, reverse bias or thermal generation, are dangling bonds. Direct evidence of creation of dangling bond states in the gap comes from a variety of experimental results: reversible change of field effect,[25,26] deep-level transient spectroscopy (DLTS),[27] defect luminescence,[28] subgap absorption,[29] and electron spin resonance (ESR) measurements.[30,31] However, the microscopic mechanism of stabilization of these metastable dangling bonds immediately after their generation or the annealing has not been clearly established.

A detailed study of the SWE was carried out by Stutzmann et al.[24] and the conclusions included: (a) The SWE is essentially an intrinsic bulk effect. The effect is independent of the concentration of major impurities like oxygen and nitrogen below 10^{19} cm^{-3}. (b) The rate of creation of these metastable defects does not depend on the energy of the incident photons in the range between 1.2 and 2.1 eV. This suggests that the defects are created after the thermalization of the optically excited carriers into the deep band tails.

It is now generally agreed that upon illumination with intense light additional metastable defects are created in the gap of amorphous silicon. This increase in the number of defects affects the opto-electronic properties of the material by decreasing the lifetime of excess carriers and shifting the position of the dark Fermi level in a

reversible manner. However, considerable controversy still remains as to the nature of these defects and the mechanism involved.

2. Hydrogen motion in amorphous silicon

The study of diffusion is important because it can yield information on the nature of intrinsic defects present in the host material. It is these defects that determine much of the physical and electronic properties of the material. In a-Si the basic nature of the intrinsic defects is still contested and hence the study of hydrogen migration remains an important issue. Various models based on changes in the hybridization of the dangling bonds,[32] impurities,[33] or silicon bond breaking[24,28,31,34-37] have been proposed to explain the origin of metastability in amorphous silicon. The first two models are now not widely accepted due to long term stability and lack of dependence on impurity concentration of these defects. Among the models that involve Si-Si bond breaking, those that involve hydrogen bonding rearrangements have gained acceptance more than others. Weak Si-Si bonds broken by the energy released from an electron-hole pair recombination would require a hop of a hydrogen from a neighbouring site to stabilize this newly formed defect and this may constitute the basic diffusion step for hydrogen.[38] Hence, the SWE may be viewed as the "light enhanced hydrogen diffusion". It is this possible role played by hydrogen in the origin of metastability that has provided an impetus to study the problem of hydrogen diffusion in these materials.

The diffusion constant of hydrogen in a-Si:H was found to obey a power-law time dependence given by[38-42]

$$D(t) = D_{oo}\ (\omega t)^{-\alpha} \qquad 1.3$$

where D_{oo} is the microscopic diffusion constant, ω is the attempt frequency and α is the temperature dependent dispersion parameter. The "Hydrogen Glass" model suggested that α is temperature dependent in the following manner:

$$\alpha = 1 - \beta = 1 - T/T_o \qquad 1.4$$

Here T is the anneal temperature and $k_B T_o$ is the characteristic energy decay constant of the exponential distribution of barriers to hopping. The energy distribution of these sites is then given by

$$N(E) = N_o \exp(-E/kT_o) \qquad 1.5$$

In this picture of multiple trapping (MT) transport of hydrogen, it is thought that as hydrogen migrates it samples deeper and deeper sites that are exponentially distributed in energy, its residence time increases and the diffusion constant decreases.

Since the diffusion constant is dispersive in time, the time t_L required for hydrogen to diffuse through a length L is given by

$$L^2 = \int_0^{t_L} 4D(t')\ dt' \qquad 1.6$$

Solving Eq. (1.6) for t_L and substituting in (1.3), the diffusion constant $D(t_L)$ can be written as

$$D(t_L) = D_o \exp(-E_{diff}/kT) \qquad 1.7$$

where

$$D_o = L^2\omega(1-\alpha)/4 \qquad 1.8$$

and

$$E_{diff} = kT_o \ln\{L^2\omega(1-\alpha)/4D_{oo}\}$$
$$= kT_o \ln(D_o/D_{oo}). \qquad 1.9$$

Thus

$$D_o = D_{oo} \exp(E_{diff}/kT_o) \qquad 1.10$$

This relation between the prefactor and the activation energy is called the Meyer-Neldel relation (MNR). It is evident that the MNR and MT process are closely related. Here E_{diff} is to be interpreted as the depth of the deepest site visited by hydrogen when diffusing through a length L and D_o, the diffusivity, is simply the attempt frequency without the thermally activated waiting time. The significance of the MNR is, however, questionable and great caution is required in assessing its meaning.[43]

The Xerox group[38-41] has argued that the decay of the excess density of band tail carriers is closely related to the diffusion of hydrogen. They suggest that

$$d\Delta n(t)/dt = - bD(t)\Delta n(t) \qquad 1.11$$

where $\Delta n(t)$ is the density of excess band tail carriers, b is a constant and D(t) is the dispersive diffusion constant of hydrogen defined in Eq. (1.3). The solution of the above equation is

$$\Delta n(t) = \Delta n_o \exp[-(t/\tau)^{\beta}) \qquad 1.12$$

Here τ is a characteristic time and $\beta = 1 - \alpha$. The decay of the excess carriers at different temperatures and the corresponding dependence of β with temperature is shown in Figures 1.4a and 1.4b. τ exhibits an Arrhenius dependence on T

$$\tau = \tau_o \exp(E_a/kT) \qquad 1.13$$

with $\tau_o = 2 \times 10^{-10}$ sec and $E_a = 0.95$ eV. For some glow discharge boron and phosphorous doped samples, electronic relaxation measurements indeed exhibited an excellent agreement with Eqs. (1.4) and (1.12) and H

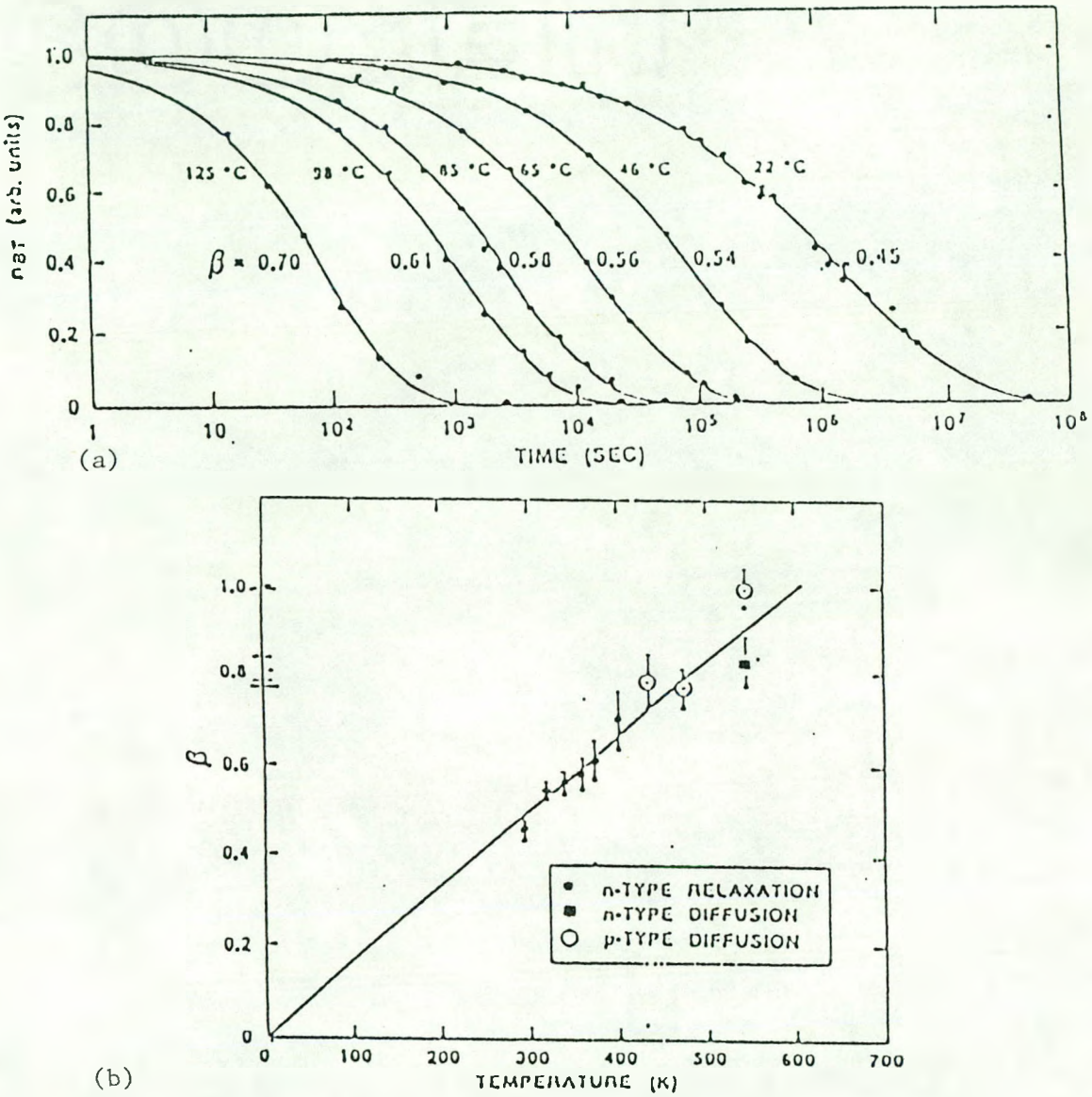

Fig. 1.4 Connection between electronic relaxations and hydrogen diffusion in a-Si:H (a) Time dependence of the density of shallow occupied band tail carriers for n-type a-Si:H, and (b) the temperature dependence of β from electronic relaxation measurements and hydrogen diffusion (from ref. 39)

diffusion measurements were consistent with the electronic relaxation measurements. However, the diffusion results were too limited in scope to verify Eq.(1.4) independently.

As mentioned earlier, Pantelides[10,12] has suggested that the five-fold coordinated silicon floating bond (FB) is likely to be a major type of defect and should at least be treated at par with dangling bonds (DB). The time dependence of the diffusion constant (Eq. 1.3) is then due to the annihilation of excess defects as the system approaches (quasi)equilibrium.

Floating bonds should be very mobile and move from one site to another simply by switching bonds (Figure 1.3a), requiring only slight movements of silicon atoms. It is important to realize that a five-fold coordinated silicon atom does not itself move through the bulk. A migrating floating bond can undergo several reactions:

$$FB + SiH \Leftrightarrow T_4 + H_i \qquad 1.14$$

$$H_i + FB \Leftrightarrow T_4 + SiH \qquad 1.15$$

Here T_4 and H_i denotes a four-fold coordinated silicon atom and an interstitial hydrogen atom, respectively. It should be noted that these and the following reactions can proceed in both directions. The other reactions that are possible with the floating bond are:

$$T_4 \Leftrightarrow FB + DB \qquad 1.16$$

and

$$H_i + DB \Leftrightarrow T_4 + SiH \qquad 1.17$$

When a sample is illuminated with light (as in the SWE), the forward direction of reaction 1.16 may be enhanced by a two step process:

$0 \Leftrightarrow e + h$ and

$T_4 + e + h \Leftrightarrow FB + DB$

Creation of defects in the gap upon illumination with light is now self evident. When a sample is illuminated, electron-hole pairs are generated. These thermalize rapidly and are soon trapped in the localized states - holes in the valence band tail states and electrons in the corresponding antibonding states. Physically some electrons and holes will then reside on the same or adjacent weak Si-Si bonds (spatial proximity is necessary for recombination to occur), which can consequently be broken during recombination. Once the bond breaking is accomplished, all the floating bond has to do is to migrate away from the dangling bond by one step in order to stabilize the defect. The energy released from the recombination of the electron-hole pair is used to overcome the reaction barrier of the bond breakup. The creation of these defects does not require any involvement of hydrogen. These excess defects that are generated can now be annealed away by the reactions 1.14, 1.15 and 1.16 driven in the forward direction. The total number of Si-H bonds during this process remains unchanged in agreement with infra-red absorption studies. Thus as hydrogen diffuses, the excess defects are removed, and the system approaches (quasi)equilibrium. An attractive feature of this model is that defect removal does not require a direct encounter between the floating and the dangling bonds. However, for this model to be viable, the high mobility of the floating bonds is a crucial property.

The evolution of hydrogen from a-Si:H is also explained rather satisfactorily by the floating bond model. The breakup of the Si-H bonds is accomplished by driving reaction 1.14 in the forward direction

and reactions 1.15 and 1.16 in the reverse direction. Floating bonds that are created by reaction 1.15 migrate and self destruct via reaction 1.14 releasing more interstitial hydrogen. This would explain the observation that the total number of hydrogen evolved is always greater than the number of defect centers generated.

The floating bond model, though elegant, is not without controversy. Since a fb - fourfold pair becomes a db - fourfold pair when sufficiently stretched, it is difficult to distinguish between the two experimentally. Indeed hyperfine splitting studies have been interpreted both as dangling bond with backbond weakening[44] or a floating bond with significant localization on one of the atoms.[45] However, a recent work by Jackson and his coworkers[46] has put an upper limit on the diffusion of the paramagnetic defects. They have concluded that $D_D < 0.6D_H$ where D_D and D_H is the diffusion constant of the paramagnetic centers and hydrogen respectively. Since the density of hydrogen is $\sim 4 \times 10^{21}$ cm^{-3} whereas the D-center density is $\sim 10^{15} - 10^{17}$ cm^{-3}, the paramagnetic defects cannot mediate the motion of hydrogen. As a result considerable skepticism still remains regarding the validity of the floating bond model.

E. Scope of this Work

In this work we studied long range hydrogen motion in undoped and boron-doped rf sputter deposited hydrogenated amorphous silicon. The samples were prepared at various rf powers and varying hydrogen contents and doping levels. Thus the microstructure of the samples could be

easily controlled and the relation between hydrogen diffusion and the microstructure could be studied. The two major techniques used in this study were infra-red (IR) absorption and secondary ion mass spectrometry (SIMS). The former yielded information on the total hydrogen content and the nature of hydrogen bonding while the latter yielded profiles from which the diffusion of hydrogen could be determined.

a-Si:H/(H,D)/H multilayers of varying thickness were prepared at different rf sputtering powers ranging from 50W to 550W. The hydrogen partial pressure and the sputtering power determined the total content of hydrogen in these films. The total hydrogen content of the samples varied from 2 to 30 at. %. The target to substrate distance during most of this work was kept between 1" and 1.25". However, one sample prepared at a 2" gap was also studied. The boron doping level, as determined by SIMS, was also dependent on both the sputtering power and the partial pressure of diborane in the chamber. Since the hydrogen diffusion in boron-doped samples was found to be faster than intrinsic samples by several orders of magnitude, the range of temperatures and the annealing time in these samples were generally lower than those of the undoped films.

II. SAMPLE PREPARATION

Most of the samples used in this work were prepared by reactive rf sputtering at a frequency of 13.56 MHz. Sputtering is one of the most widely used techniques currently employed for deposition of thin films of a variety of materials. Deposition is attained by bombarding a target with high energy ions of an inert gas (argon in this work) by application of an rf field.

The target used in this work was a 6" diameter 99.99% purity polycrystalline silicon target, mounted on a water cooled stainless steel backplate located at the top of the chamber. Various types of substrates were used in this work. Single crystal silicon wafers were used for IR absorption and SIMS measurements, while Corning 7059 glass slides were used for UV-Vis-NIR absorption and ESR measurements. Films were also deposited on aluminium foils from which powdered samples could be extracted for nuclear magnetic resonance (NMR) experiments. The substrates were placed on a stainless steel plate 1/4" in thickness and 2.75" in diameter. The target to substrate distance could easily be varied and was set between 1" and 2" for most of this work.

Before any film was deposited, the sputtering chamber (Figure 2.1) was pumped to about $2.0 \pm 1.5 \times 10^{-7}$ torr. The gate valve was then opened three turns in order to slow the pumping rate and thereby depositing the film at the desired flow rate. The gases were now introduced one at a time. The order in which the gases were introduced depended on the desired partial pressures. The gas with the least partial pressure was introduced first followed by the one with the next

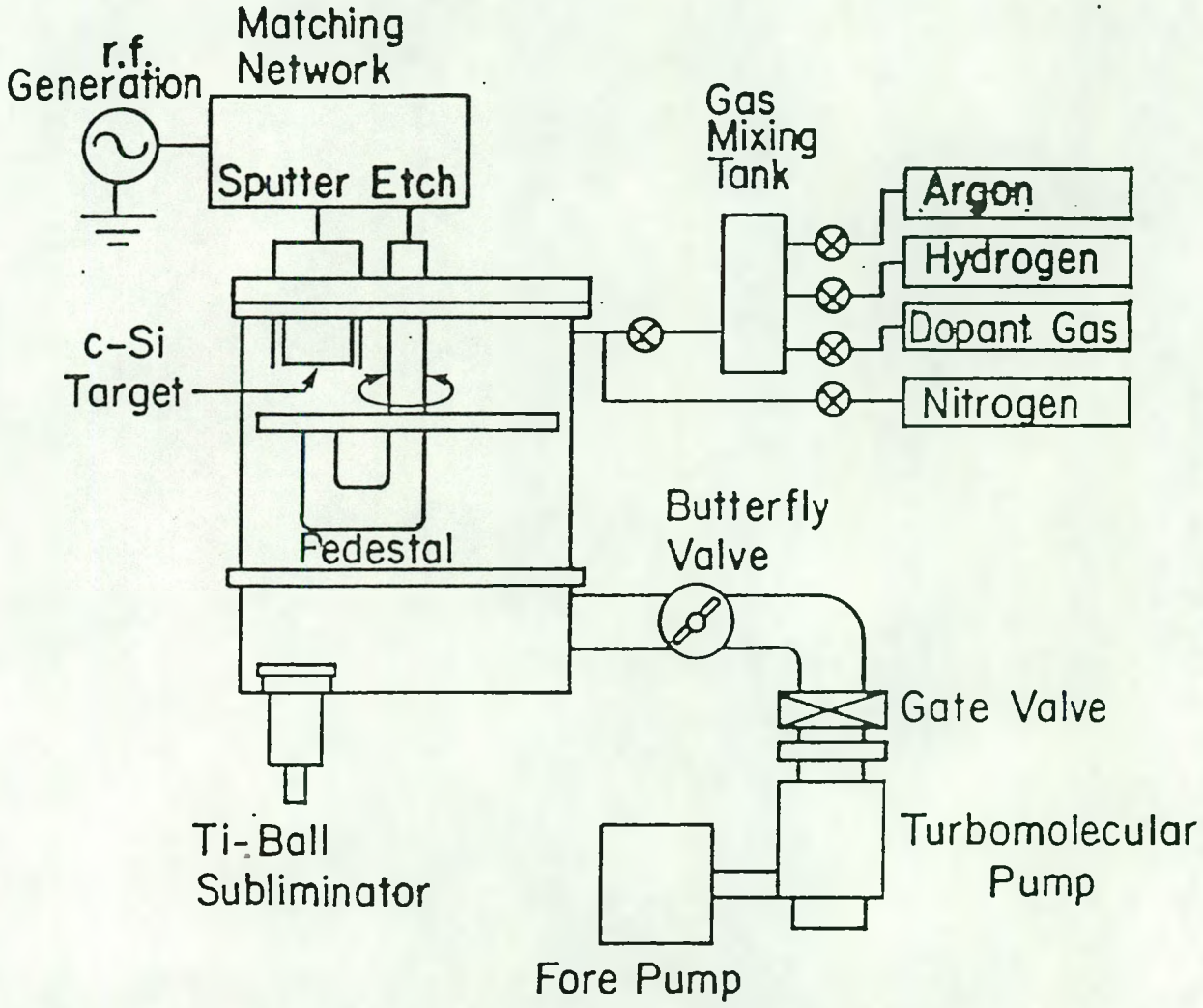

Fig. 2.1 Schematic diagram of the rf sputtering system

highest pressure and so on. The pressure of each gas could be adjusted by turning a needle valve (one for each gas line) which controlled the flow rate.

Once the final, steady state pressures of the different gases were obtained, an rf power was applied across the target and the pedestal (which was grounded). The inert gas atmosphere within the chamber always has some free electrons and ions. These charged particles are accelerated and gain in kinetic energy in the induced rf field. Collisions with other inert gas atoms ionize some of these atoms. This proccess continues until a plasma is generated.

The applied rf field is shown in Figure 2.2. Although the field is actually sinusoidal, it is schematically shown as a square wave in order to simplify the following discussion. In the first half of the cycle, the target is held at a positive potential with respect to ground. Electrons in the plasma are thus attracted towards it. As the electrons impinge on the target, its overall positive bias is reduced. In the second half of the cycle the polarity of the target is reversed and positively charged inert gas ions are now attracted towards it reducing its overall negative bias. The mass of the ions is much heavier than the electrons and hence their response to the changing rf field is much slower. At 13.56 MHz, the potential of the target is reversed before the ions can fully reduce the applied bias. Consequently, over a few cycles the target attains an overall negative bias $-V_{SB}$, with respect to the plasma and the grounded pedestal (and hence the substrates). This naturally occuring self bias is the key to the sputtering process. The positive ions are formed in the "glow region" and are accelerated

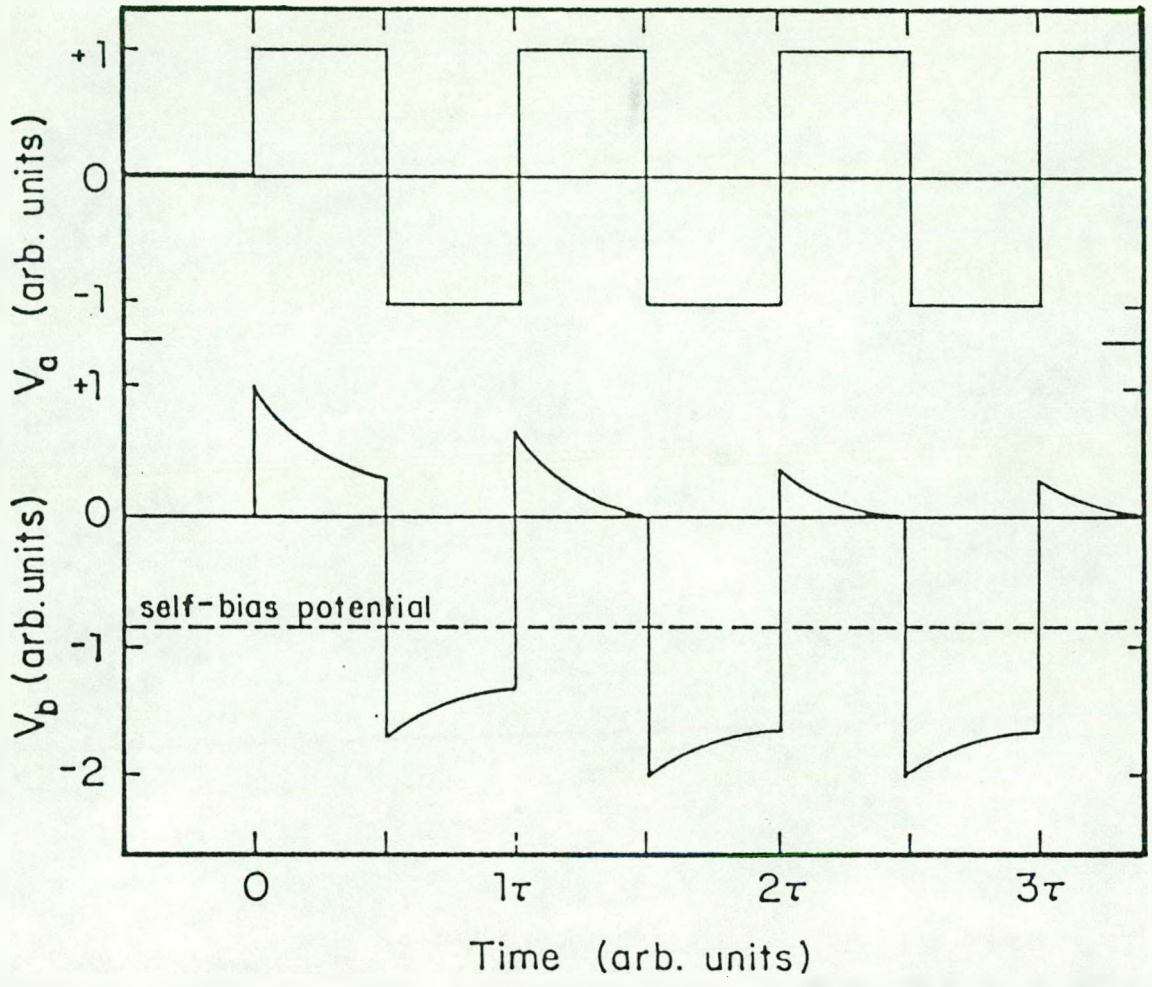

Fig. 2.2 Voltage vs time characteristic for the source, V_a, and the target, V_b, in a rf sputtering system. The period of the voltage source is τ (from ref. 18)

through the "dark space" (Figure 2.3) onto the target. As they bombard the target, atoms on its surface are ejected. Since the sheath voltage V_p is small, the accelerating voltage experienced by the ions is approximately equal to the potential difference between the target and the subtrates. This acceleration potential depends on the rf power but is independent of the pressure of the inert gas used. The sputtered atoms are largely electrically neutral, consequently travel across the chamber along the "line of sight", and are deposited onto the substrates.

To maximize the power transmitted through the target, an rf matching network is used. It consists of two variable capacitors one of which is connected in series and the other in parallel to the capacitor formed by the target and the pedestal. By matching these capacitors, the reflected power from the target can be reduced to less than 2.5 W for the entire range of transmitted power that was used in this work.

Both undoped and boron doped single-layered and multilayered samples were deposited at transmitted powers ranging from 50 W (0.27 W/cm^2) to 550 W (2.97 W/cm^2). The multilayered samples were of two types : a-Si:H/a-Si:D/a-Si:H and a-Si:H/a-Si:(H,D)/a-Si:H. However, in both cases the middle layer contained deuterium and was sandwiched between two hydrogenated layers. When samples of the former type was prepared, the hydrogen flow to the chamber was shut off while the deuterium flow was started during the deposition of the middle layer. After the middle layer was deposited, the hydrogen flow was restored while the deuterium flow was cut off. The partial pressures of both hydrogen and deuterium was comparable. a-Si:H/a-Si:(H,D)/a-Si:H multilayers, on the other

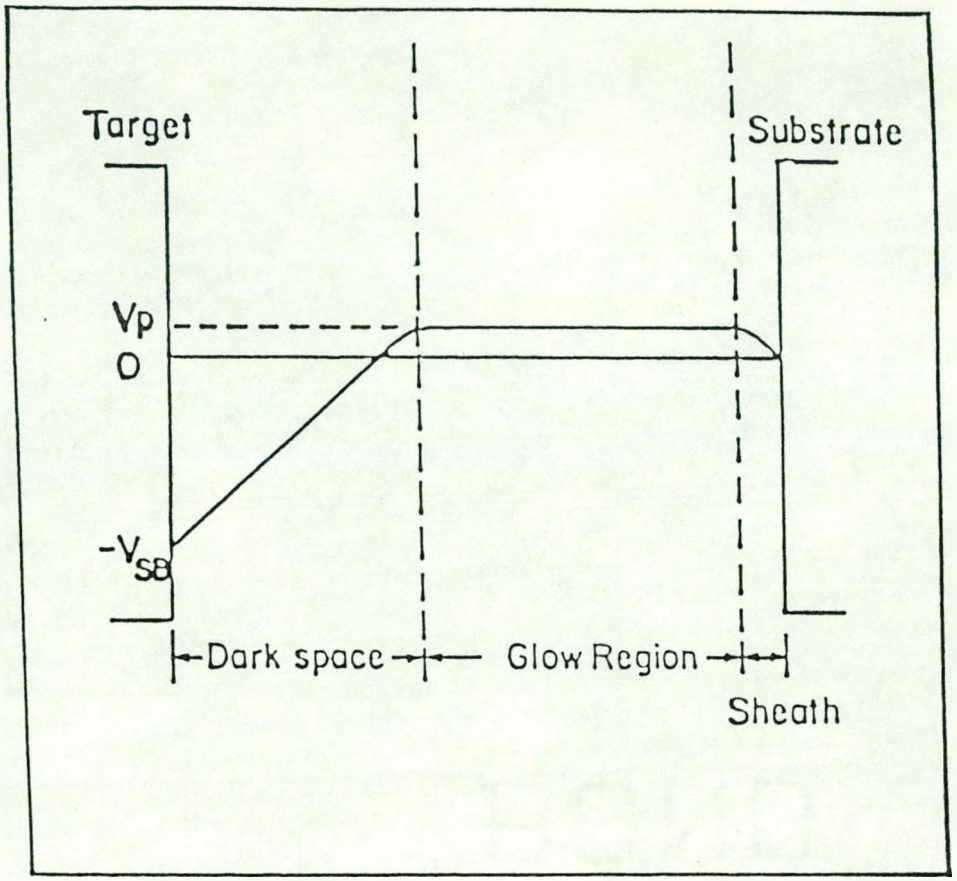

Fig. 2.3 Schematic description of the distribution in an rf sputtering process. V_p is the sheath plasma voltage between the plasma and the substrate, and V_{SB} is the self bias which is responsible for the sputtering of the target (from ref. 18)

hand, were made by introducing deuterium (D) in the middle layer while the flow of hydrogen was allowed to continue uninterrupted. The partial pressure of deuterium was always much lower than that of hydrogen, to minimize its effect on the microstructure or electronic properties of the film. The interfaces on either side of the middle layer remained reasonably sharp in the pristine samples indicating little diffusion during the deposition process.

The quality of the film depended on the deposition conditions. The various parameters that were controlled during the deposition process were the following:

Inert gas partial pressure

The inert gas used throughout this work was argon. The partial pressure of argon was kept constant and was maintained at about 10mT. This value was suggested to be optimal by Moustakas[47] who demonstrated that films grown at higher pressures exhibited columnar morphology and incipient microvoids, thereby reducing the quality of the film. Both the deposition rate and the thermalization distance depends on the argon partial pressure. Generally the deposition rate increases and the thermalization distance decreases with increasing argon pressure (see below).

Hydrogen partial pressure

The hydrogen partial pressure is one of the most important parameters that control the opto-electronic properties of the film. The content of hydrogen in the sample can be changed conveniently by

adjusting the partial pressure of hydrogen. Moustakas, Tiedje and Lanford[48] proposed a kinematic model for the incorporation of hydrogen in rf sputter deposited amorphous silicon films. Under the assumption that (a) there is no significant desorption of bonded hydrogen, (b) there is no gas phase reaction between silicon and hydrogen, and (c) hydrogen incorporation arises from surface reactions only, they showed that the total hydrogen content in the film $[H_T]$ is given by

$$[H_T] = [H_T]_{max} [1 - \exp(-F\Theta\sigma/R_d) \qquad 2.1$$

Here $[H_T]_{max}$ is the maximum possible concentration of hydrogen, F is the flux of hydrogen onto the growing surface, R_d is the deposition rate, Θ is the sticking coefficient, and σ is the capture cross section. Since the partial pressure of hydrogen determines its flux, the total hydrogen content of the film is critically sensitive to this parameter assuming that the other deposition parameters remain unaltered.

Transmitted power

The transmitted power is another important deposition parameter that critically determines the quality of the film. The transmitted power affects the sputtering yield Y, which is defined as the number of target atoms ejected per incident inert gas ion. It increases with increasing transmitted power, i.e., target voltage. This is expected since the momentum transfer between the incident ions and the target causes material of atomic dimensions to be ejected. The deposition rate of the growing film is given by

$$R_d = Y \frac{(\text{Sputtering ion density})}{(\text{density of a-Si:H})} \qquad 2.2$$

Since the density of the hydrogenated amorphous film is roughly constant (~5.12 x 10^{22} cm^{-3}), the deposition rate depends on the sputtering yield Y and the inert gas partial pressure which determines the sputtering ion density. Since the argon partial pressure was maintained at about 10mT, any increase in the deposition rate with increasing rf power reflected an increase of the sputtering yield. This is demonstrated in Figure 2.4 where the sputtering yield of both germanium and silicon is plotted against incident ion energy. It is clearly seen that as the incident ion energy increases with increasing transmitted power, the sputtering yield also increases. This is also reflected in the deposition rate which increases with transmitted power. If the hydrogen partial pressure is now held constant, the total H content of the film can be controlled through Eq. (2.1).

Changing the transmitted power has other effects too. For example, an increase in the rf power increases the plasma-film interaction as the growing film is increasingly bombarded by the ions from the plasma. This enhanced bombardment destroys internal surfaces and incipient porous and/or columnar morphology, lowering both the dangling bond spin density and the number of di- and tri-H silicon bonds associated with these internal surfaces.

Target to substrate distance

The distance between the target and the substrate plays an important role in determining the defect density of the film. Moustakas[47,49] suggested that bombardment of the growing film by the heavy inert gas

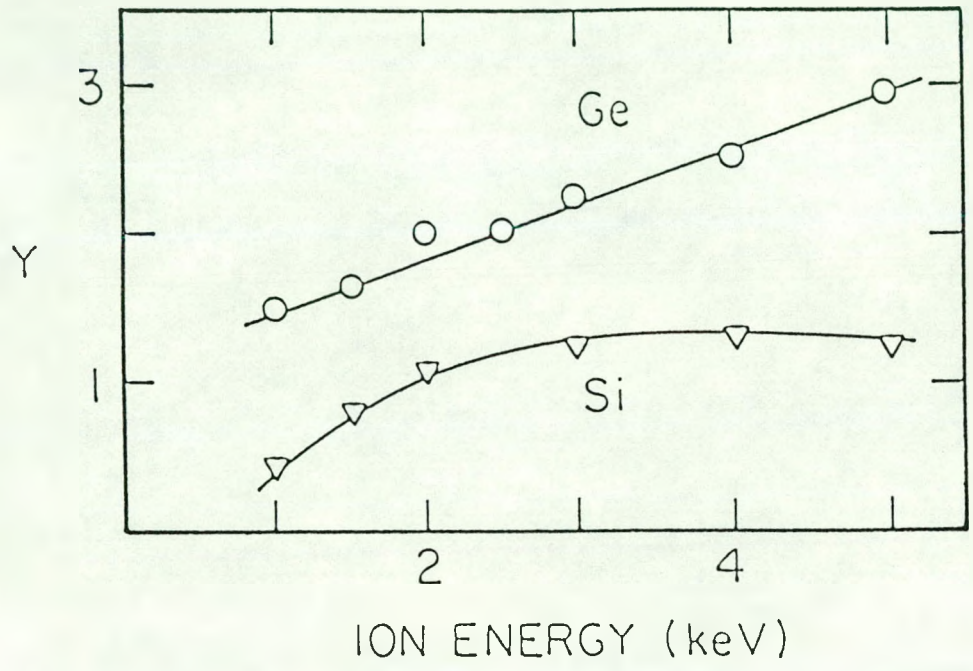

Fig. 2.4 The sputtering yields of Ar^+ ions bombarding Si and Ge target vs ion energy

atoms has a deleterious effect on the quality of the film. An increase in the spacing between the electrodes results in more collisions between the inert gas atoms and thus thermalizes them before they reach the substrate. The thermalization distance, however, also depends on the inert gas partial pressure. As this pressure is increased the thermalization distance decreases.[50]

Wu[51] discussed the dependence of the thermalization distance on inert gas atomic mass, partial pressure and the incident ion energy in detail. For a-Ge deposited at 150 W in 10 mT of argon the thermalization distance was estimated to be 2.2".[52] For a-Si, it has been suggested that under similar conditions, a target-to-substrate distance of 1.2" is sufficient to thermalize silicon atoms below 10 eV while a distance greater than 2.4" is required to thermalize all atoms with energies up to 1 keV.[51]

Substrate temperature and plasma-film interaction

Film growth during the deposition process is not uniform. It begins on numerous nucleation sites or "islands" on the substrate. As these islands grow both vertically and laterally, the film develops both microvoids and columnar morphology that adversely affect its performance.

Heating the substrate generally has a beneficial effect. It enhances the lateral mobility of the surface atoms thereby reducing the columnar morphology and microvoids. Another effect pertains to silicon atoms on the surface of the growing film which are associated with more than one hydrogen atom. Since these di- and tri-H bonds are broken to

form molecular H_2 at ~250°C, heating the substrate reduces the density of these bonds and improves the opto-electronic properties of the film. Care should be taken, however, when heating the substrate. The mono-H bonds break at ~ 500°C and too high a temperature can, and indeed does, have a deleterious effect on the quality of the film.

In rf sputtering, the substrate is also heated due to electronic bombardment. Fast electrons from the target (mostly secondary electrons) can overcome the small sheath voltage (Figure 2.3) and pass almost unattenuated through the plasma (due to their low crossection) and bombard the substrate causing it to heat up. Due to a small bias of ~ 10 - 15 V relative to the plasma, positive ions such as Ar^+ and H^+ are also accelerated towards the substrate and bombard the growing film. The effects of this plasma-film interaction are not well understood. Moustakas[49] suggested that electronic bombardment is beneficial since it delivers heat to the growing film and thus enhances thermal rearrangement of the surface atoms. Ar^+ bombardment, on the other hand, promotes growth of microvoids and columnar morphology, and hence is undesirable. His conclusions, however, are in disagreement with the work of other groups.[19,53-55] Rudder, Cook and Lucovsky,[54,55] for example, have produced high quality a-Ge:H films by magnetron sputtering - a process that is characterized by low electronic bombardment of the substrates.

The mechanism of sputtering is very complicated and many of the processes that are involved are not well understood. Nevertheless, the advantage of rf sputtering, for our purposes, remains in the fact that samples with a wide variety of microstructures and H content could be

prepared by changing the deposition conditions in a systematic manner. The deposition parameters are, however, not independent of each other. A change in one affects one or more other conditions. For example, a change in the anode to cathode distance has an effect on the plasma-film interaction and hence on the effective temperature of the growing film.

Good quality films, as judged from infrared absorption spectra, were produced using the following deposition conditions: partial pressure of argon and hydrogen set at 10 mT and 0.5 mT respectively, transmitted power greater than 500W and target-to-substrate distance between 1" and 1.25". Although the substrates were not heated, their temperature is estimated to be ~ 180^{o}C at 550W. These samples had ~ 10 at. % of hydrogen with little or none in di- or tri-H bonding configurations. On the other hand, samples deposited at 50W with 1.5 mT of hydrogen had over 30 at. % of hydrogen of which a substantial fraction was in di- and tri-H bonding configurations.

The goal of this work was to study the long range hydrogen motion in undoped and boron-doped a-Si:H with changing hydrogen microstructure. In this respect, rf sputtering was one of the most easy and convenient methods of depositing a-Si:H.

III. SAMPLE CHARACTERIZATION

A. Thickness Measurements

During each deposition run a Corning 7059 glass substrate was partially masked such that there was no deposition on one part. The thickness of the film was then measured mechanically using a Sloan Dektak stylus profilometer which had an accuracy of ±1000 Å. Uniformity of deposition was checked occasionally by placing two such masked glass pieces at opposite ends of the stainless steel pedestal and measuring the thickness. The difference was invariably found to be no more than 5%.

B. Optical Measurements

The optical band gap E_g was determined using a Cary Model 14 spectrophotometer. A schematic representation of the Cary is shown in Fig. 3.1. The Cary spectrophotometer is a dual beam instrument which measures the optical density (OD) at different wavelengths. The optical density is defined as

$$OD = \log_{10}(I_o/I) \qquad 3.1$$

where I_o and I are the intensities of the incident and the transmitted light respectively. The transmission T is defined as

$$T = I/I_o \qquad 3.2$$

and hence the relationship between transmission and the optical density immediately follows:

$$T = 10^{-OD} \qquad 3.3$$

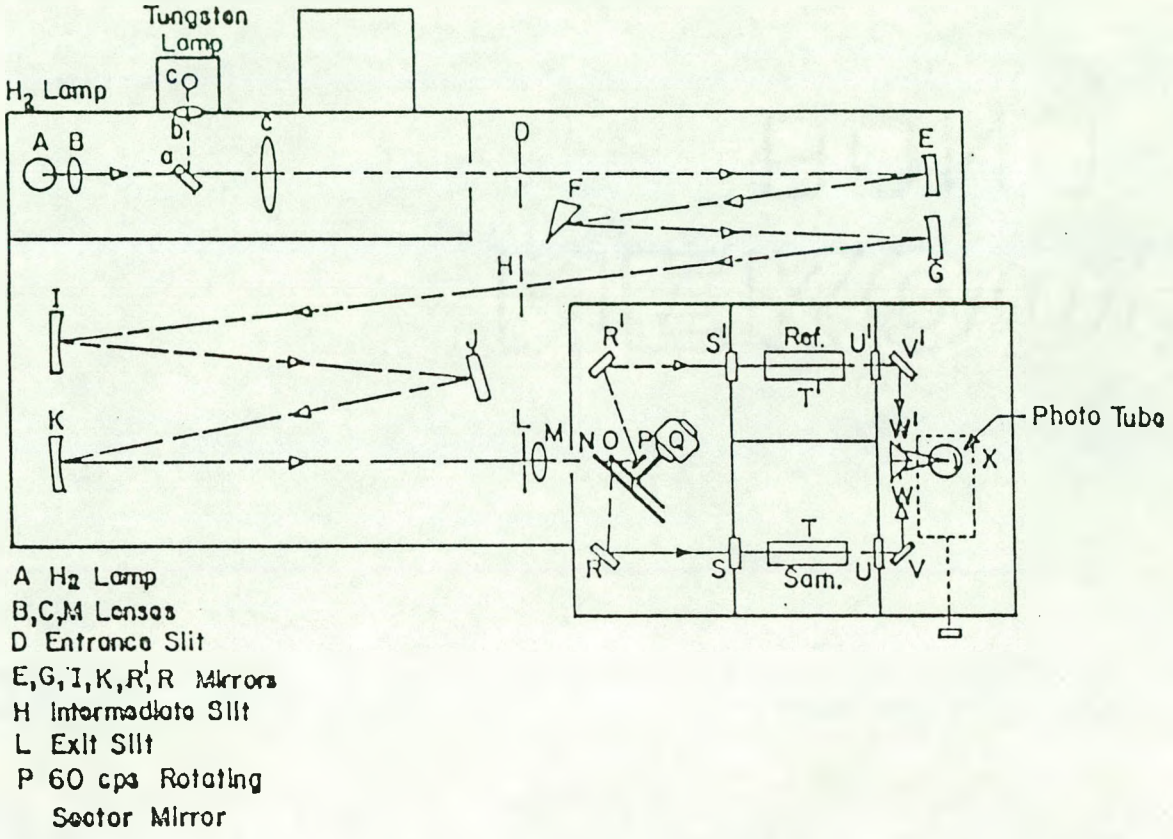

Fig. 3.1 Optical system in the Cary Model 14A spectrophotometer used in this work

The light beam in the Cary was split in two. One beam passed through an empty reference compartment while the other traveled through the sample compartment. To balance the intensities of the two beams, the Cary automatically adjusted the size of the entrance slits; the ratio of the slit sizes gave the ratio of I_o to I. The light source was a General Electric quartzline lamp. Wavelengths from 325 nm to 2100 nm were scanned using the monochromator of the Cary and the corresponding optical densities recorded on a strip chart recorder. A maximum optical density of two could be measured by the Cary. This value corresponds to a transmission of 1% (Eq. 3.3) and an absorption of 10^4 cm^{-1} for a 1 μm thick sample (from Eq. 3.7).

When radiation passes through a film of thickness d, its intensity is attenuated. Knowledge of d immediately yields information on the optical absorption coefficient α through the relation

$$I = I_o \exp(-\alpha d) \qquad 3.4$$

Since samples deposited on Corning 7059 glass were used for optical absorption measurements, the reflection coefficients of the air/film and film/glass interfaces must be taken into account. The reflection coefficient at the a/b interface R_{ab}, can be written as

$$R_{ab} = \frac{(n_a - n_b)^2}{(n_a + n_b)^2} \qquad 3.5$$

where $\mathbf{n_a} = n_a + ik_a$ is the complex index of refraction of medium a, and the index of air, film, and glass is 0, 1, and 2 respectively. After allowing for multiple reflections in the sample, the transmission

coefficient T can be shown to satisfy (see ref 18 for a detailed discussion)

$$T = \frac{T_g(1 - R_{01})(1 - R_{12})\exp(-\alpha d)}{1 + R_{01}R_{12}\exp(-\alpha d) - 2(R_{01}R_{12})^{1/2}\exp(-\alpha d)\cos(4\pi n_1 d/\lambda)} \qquad 3.6$$

where R_{01} and R_{12} are the reflection coefficients from the air/film and film/glass interfaces respectively. Here T_g, the transmission through glass has been included to compensate for absorption in glass. The glass was found to have a transmission of 0.97 in the wavelength region of interest.

The optical density versus wavelength plot of a typical sample is shown in Fig. 3.2. The $\cos(4\pi n_1 d/\lambda)$ term in the denominator gives rise to interference fringes in the wavelength region where α is small. However, as α becomes increasingly larger, both terms in the denominator become small compared to unity and α can then be approximated to

$$\alpha = -\frac{1}{d}\ln\left[\frac{10^{-OD}}{T_g(1 - R_{01})(1 - R_{12})}\right] \qquad 3.7$$

Since the thickness of the sample and the refractive indices of air and Corning 7059 glass is known (1.0 and 1.53 respectively), knowledge of n_1 completely defines α.

Assuming that $k_1^2 << (n_1 - n_0)^2$, $(n_2 - n_1)^2$, the reflection coefficients can now be written as

$$R_{01} = \frac{(n_1 - 1)^2}{(n_1 + 1)^2} \qquad 3.8a$$

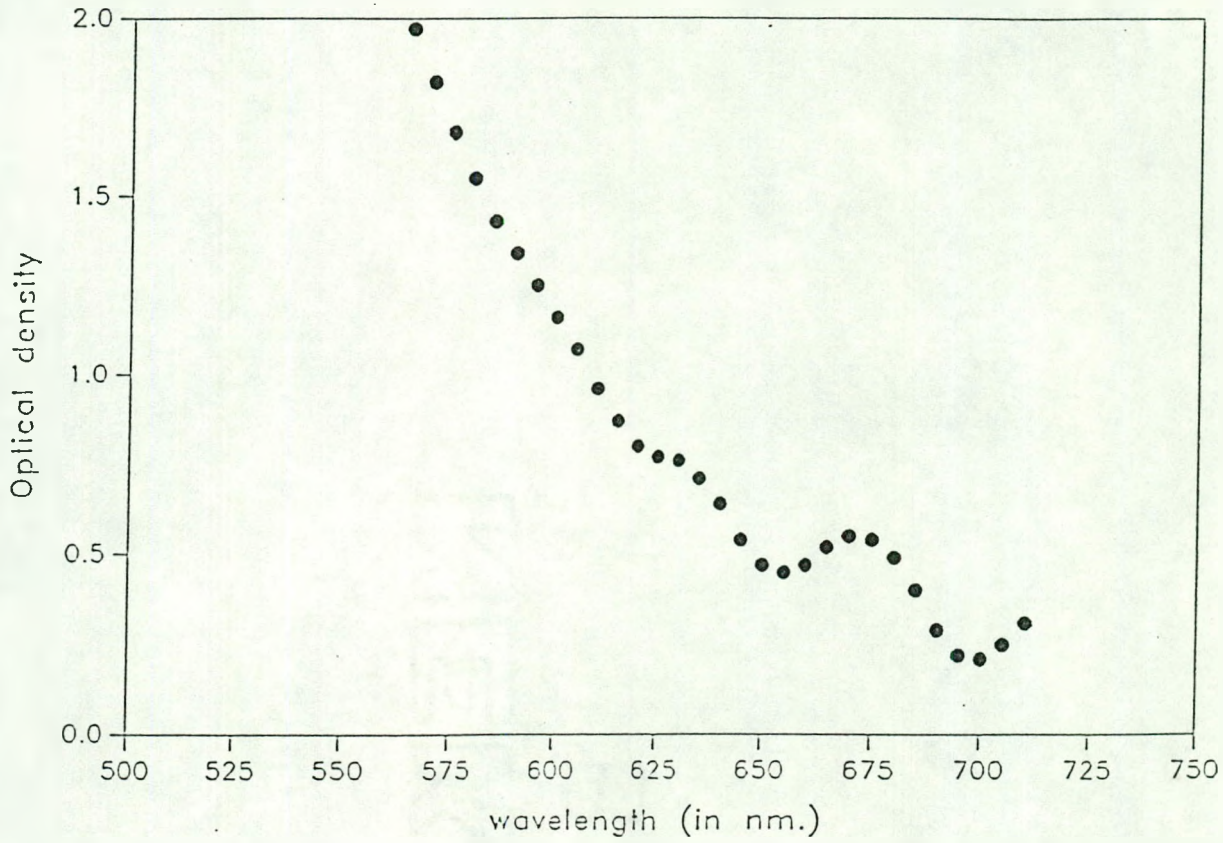

Fig. 3.2 A typical optical density vs. wavelength spectrum

and

$$R_{12} = \frac{(n_1 - 1.53)^2}{(n_1 + 1.53)^2} \qquad 3.8b$$

Using the relation $k_1 = \alpha\lambda/4\pi$ and recognizing that the maximum value of α (for d = 1 μm) that can be measured by the Cary is ~ 10^4 cm^{-1} at λ ~ 500 nm, the maximum possible value of k_1 is ~ 10^{-2}. Since the accepted value n_1 is ≃ 3.5, the above assumption certainly holds. The refractive index can be estimated from the interference fringes in the OD vs. wavelength plot. If λ_1 and λ_2 are the wavelengths where two consecutive minima in the OD (i.e. transmission maxima) occur, then the average refractive index in that wavelength region n, is given by

$$n = \lambda_1\lambda_2/2d(\lambda_2 - \lambda_1) \qquad 3.9$$

An alternate way of estimating n is by solving Maxwell's equations in the film and showing that as conductivity tends to zero, as in insulating materials, n tends to $\sqrt{\varepsilon}$ where ε is the dielectric constant.[56]

The absorption coefficient α can now be calculated using Eq. (3.7). As has been mentioned earlier in Chapter I, unlike its crystalline counterpart, amorphous semiconductors have allowed states in the energy gap. Hence α is always greater than zero even at low energies. The optical gap E_g was determined using the relation suggested by Tauc et al.[57]:

$$(\alpha h\nu)^{1/2} = B(h\nu - E_g) \qquad 3.10$$

where B is a material dependent constant which depends on the density of tail states (and hence on disorder). A Tauc plot is shown in Fig. 3.3.

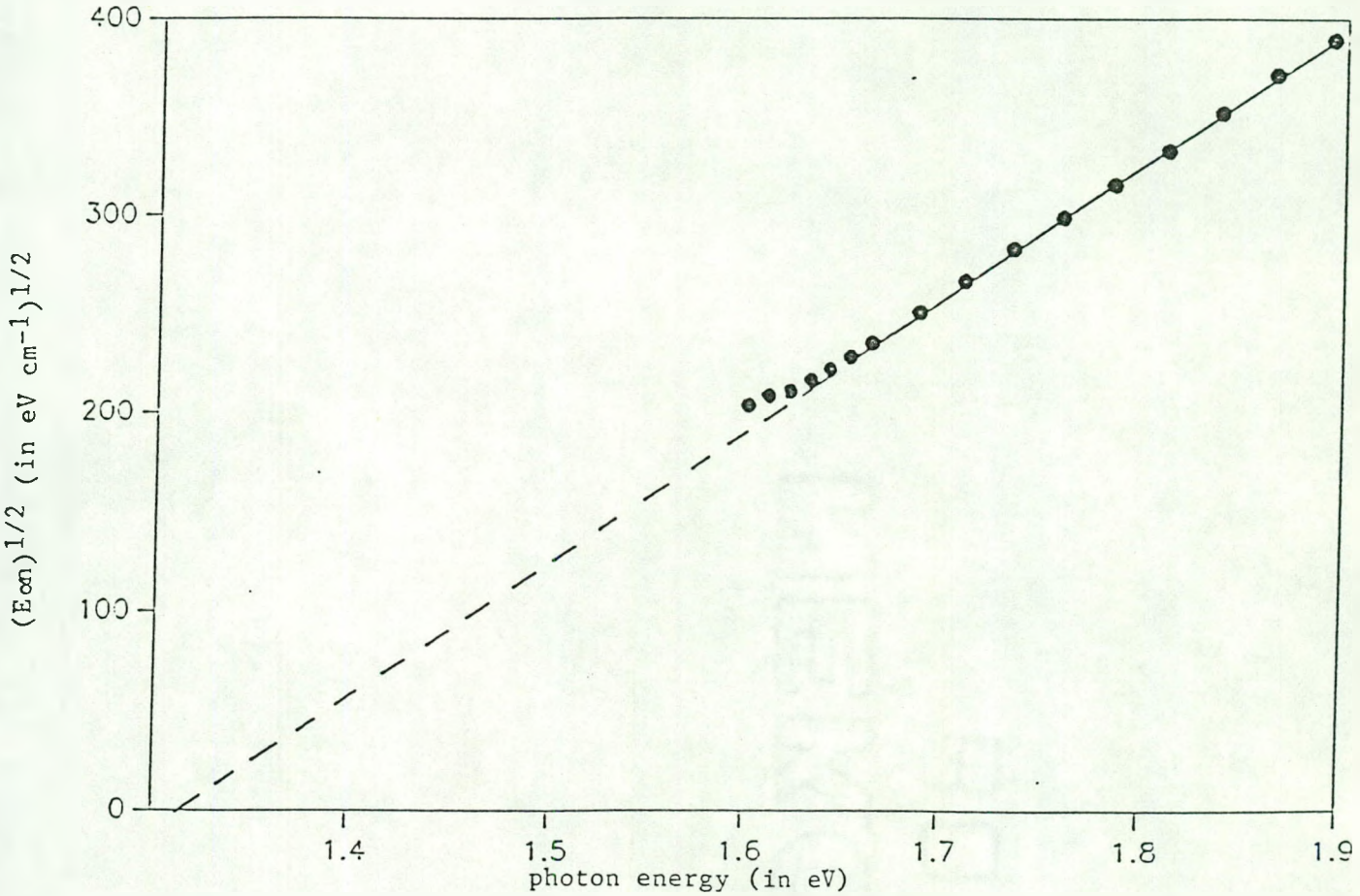

Fig. 3.3 $\sqrt{E\alpha n}$ vs. E for sample 92

The optical gap E_g is found by extrapolating the straight line in the plot of $(\alpha h\nu)^{1/2}$ vs. $h\nu$ to $\alpha = 0$. The intercept of the line with the $h\nu$ axis then yields E_g.

Absorption below and near the Tauc gap is dominated by bandtail to bandtail transitions. The absorption coefficient in this case is given by the Urbach relation (Eq. 1.2). To measure the Urbach coefficient E_o, the absorption must be measured to small values ($100 \leq \alpha \leq 5000$ cm^{-1}). This requires depositing films thicker than 4μm and was not attempted in this work. Albers[18] has found E_o to be ~ 0.08 and ~ 0.09 eV for argon sputtered a-Si:H deposited at 100 and 600 W respectively. However, for device quality material E_o lies typically between 0.04 to 0.05 eV.[58,59] Note that for c-Si, E_o is about 0.01 eV.[58]

C. Infrared Absorption

Samples deposited on single crystal silicon substrates were used for the measurements of infrared (IR) absorption using a single beam Fourier Transform Infrared (FTIR) spectrometer IBM model IR 98. IR absorption is an important technique that is widely used to characterize both a-Si:H and a-Ge:H. It provides information on the total hydrogen content, hydrogen bonding configurations and presence of oxygen (above ~ 0.5 at. %) in the films. Typical IR spectra for two samples are shown in Figs. 3.4 and 3.5. The absorbance of the blank substrates has been subtracted from the absorbance of the film-substrate to give the absorbance of the film alone.

The IR spectra of a-Si:H (a-Ge:H) display three main vibrational modes for hydrogen, was first identified by Brodsky and coworkers.[60]

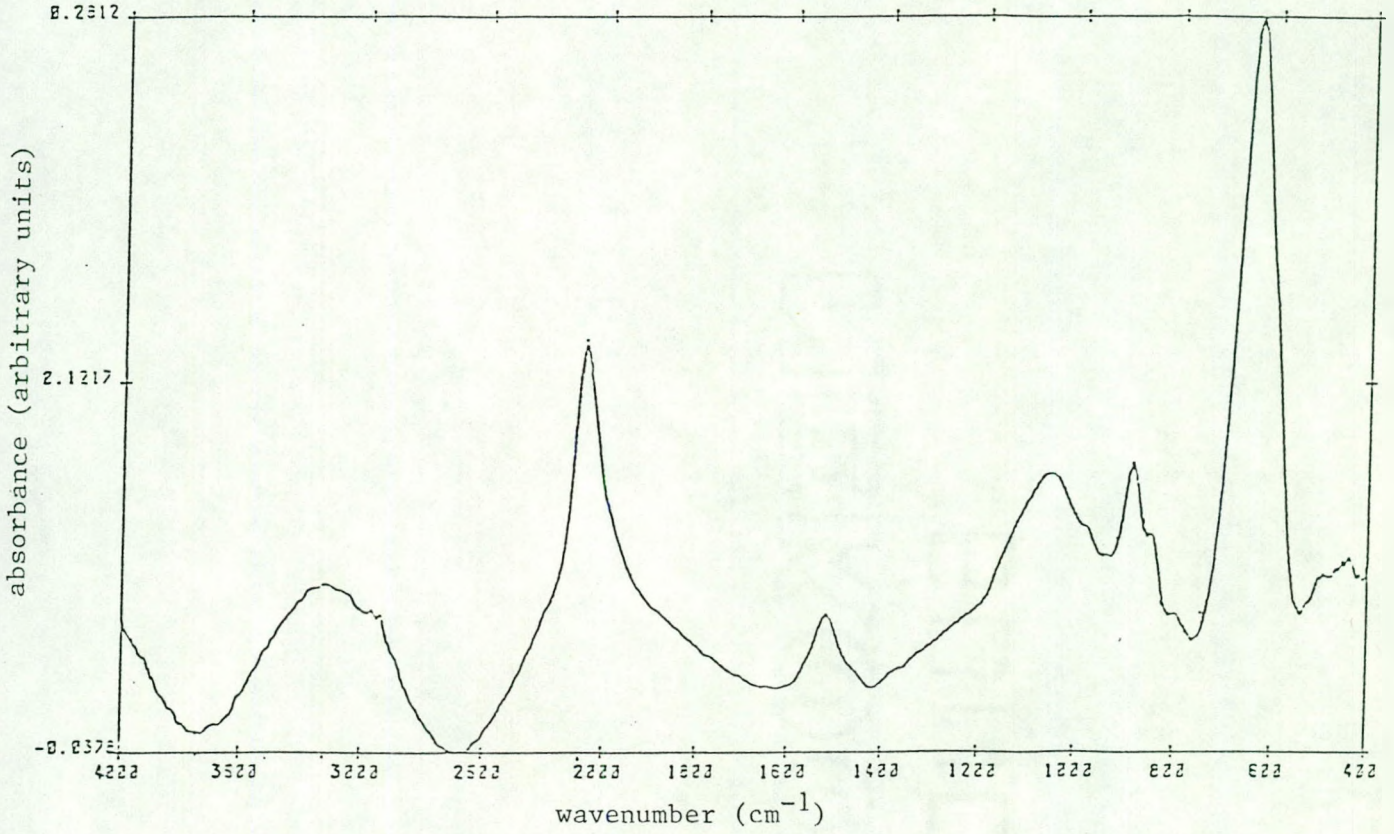

Fig. 3.4 The IR absorption spectrum of sample 11 (as deposited)

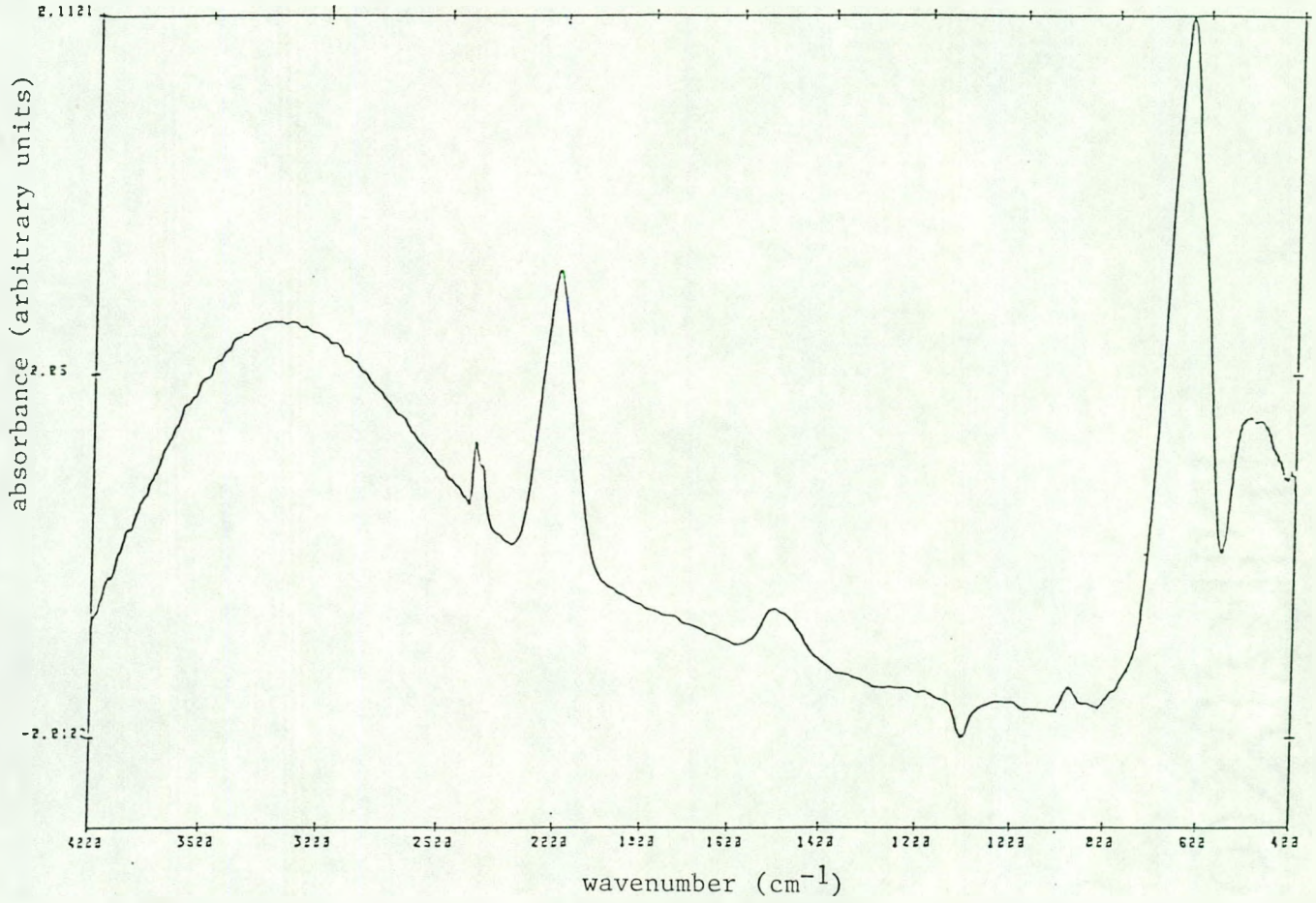

Fig. 3.5 The IR absorption spctrum of sample 13 (as deposited)

These are (a) the Si-H wagging mode at ~ 640 cm^{-1} (580 cm^{-1}), (b) the $Si-H_2$ and $Si-H_3$ scissors or bond bending mode 840 - 890 cm^{-1} (780 cm^{-1}) and (c) the Si-H stretching mode at 2000 - 2100 cm^{-1} (1870 - 1970 cm^{-1}). A schematic of these modes is shown in Fig. 3.6. The density of oscillators N in each vibrational mode is given by

$$N = A^* \int \alpha(\omega)/\omega \, d\omega \qquad 3.11$$

where α is the absorption coefficient, ω the angular frequency, and A^* a proportionality constant depending on the oscillator strength. The values of A^* of the different modes were first determined experimentally by Shanks et al.[61] and are listed in Table III.

The 640 cm^{-1} wagging mode, which shows no discernible structure, is attributed to silicon-bonded hydrogen in any bonding configuration. The prefactor A^* of this mode has been found to be nearly independent of both the deposition conditions and total hydrogen content.[61] The total silicon-bonded hydrogen content $[H_T]$ calculated from this absorption peak is thus considered to be reliable. Eq. (3.11) and the experimental value of A^* then yield the following expression for $[H_T]$:

$$[H_T](\text{at. \%}) = 1.1245 \, A_{640}/d \qquad 3.12$$

where A_{640} is the area (in cm^{-1}) under the 640 cm^{-1} absorption peak and d is the film thickness in microns. The concentration of $Si-H_2$ (di-) and $Si-H_3$ (tri-H) bonds N_d is similarly given by

$$N_d(\text{at. \%}) = 10.44 \, A_{840}/d \qquad 3.13$$

However, the oscillator strength of both the scissors and stretch mode depends the arrangement of Si atoms around the Si-H bond. A^* of these modes thus changes with both preparation conditions and hydrogen content. Consequently, the concentration of silicon atoms bonded to

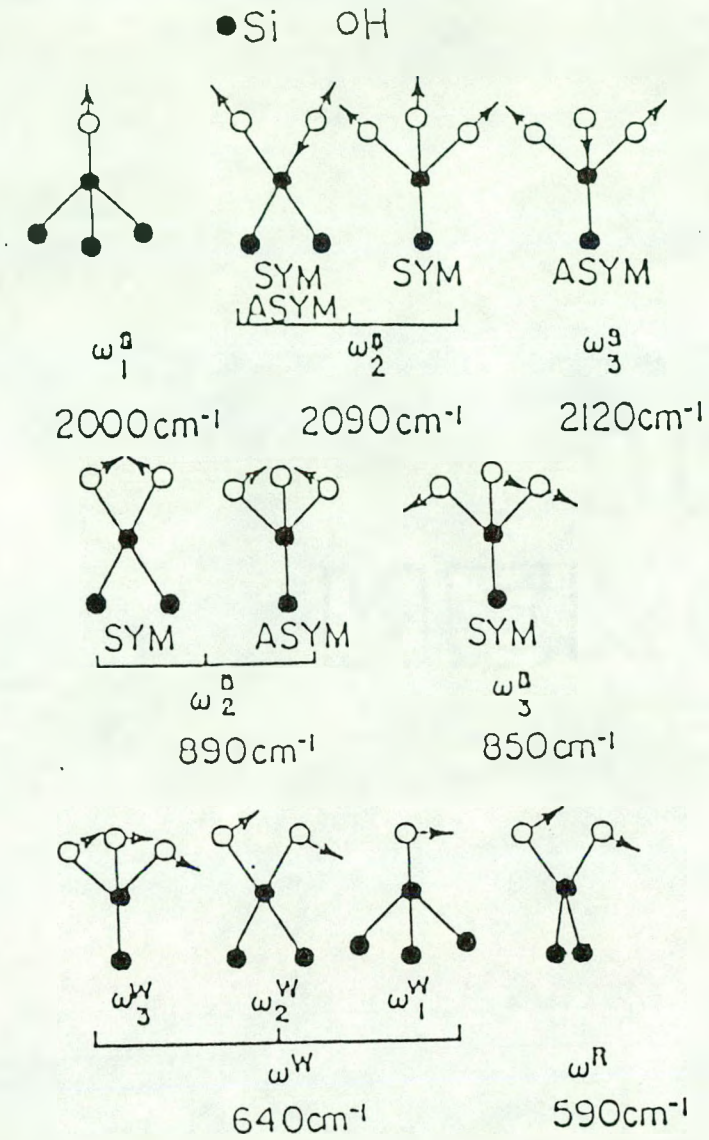

Fig. 3.6 Schematic illustration of the bond-stretching (top row), bond-bending (middle row), and bond wagging and rocking (bottom row) modes of SiH, SiH_2, and SiH_3 groupings in either a-Si:H gaseous silanes. The frequencies shown are for a-Si:H. The solid and open circles represent Si and H atoms respectively. Only bonds relevant to the central Si are shown (from ref. 58)

Table III. The various vibrational modes of hydrogen in a-Si:H, their bonding configurations and the corresponding proportionality constant A^* (from Ref. 18)

Wavenumber	640	840-890	2000	~2100	2100 (cm^{-1})
Mode	Wag	Scissors	Stretch	Stretch	Stretch
Bonding	Si-H $Si-H_2$ $Si-H_3$	$Si-H_2$ $Si-H_2$	Si-H (Isolated) (microvoids)[a]	Si-H (Cluster) (microvoids)[b]	$Si-H_2$ $Si-H_3$
$A^*(cm^{-2})$	$1.6x10^{19}$	$2x10^{20}$	$2.2x10^{19}$	$1.7x10^{20}$	$9.1x10^{19}$

[a]Compressed microvoids
[b]Microvoids with radius $\geq$ 2Å
See text for details.

more than one hydrogen, obtained from the integrated intensity of the 840-890 cm^{-1} band should be viewed with some caution.

The stretch peak at 2000 cm^{-1} is believed to result from isolated mono Si-H bonds in the bulk or in "compressed", "compact" microvoids, probably "pancake" shaped, in which opposite surfaces are less than ~ 3Å apart.[62] The peak at 2100 cm^{-1} has been attributed to silicon associated with di- and tri-H bonds or to mono Si-H bonds at internal surfaces of larger microvoids.[60] However, it is not possible to distinguish between silicon bonded to two or three hydrogen atoms from either the scissor or the stretch peak. It has been pointed out that the stretch frequency of a mono Si-H bond shifts from 2000 to 2100 cm^{-1} as the radius of the void around the hydrogen increases to 2 Å.[63-65] Shanks et al.[63] have also suggested that the 2100 cm^{-1} stretch peak is due, in part, to clusters of silicon atoms each bonded to one hydrogen atom. Multiple quantum NMR measurements by Reimer and coworkers have suggested that in device quality material, these clusters typically contain 4 to 7 hydrogen atoms.[66,67] They have attributed the stretch frequency at ~ 2080 cm^{-1} to these clusters. As the quality of the material deteriorates, both the size and the number of these hydrogen clusters increase.[67] Thus the interpretation of the stretch peak is not straightforward and hence is considered to be unreliable, in this work, in determining unambiguosly the hydrogen bonding configuration.

Presence of oxygen at levels above ~ 0.5 at. % in the samples can also be detected from the absorption spectra. Additional absorption peaks at 900 cm^{-1} and 1100 cm^{-1} are seen in oxygen contaminated samples. The 900 cm^{-1} peak is attributed to bulk Si-O bonds[68] while that at 1100

cm^{-1} is assigned to oxygen bonded at internal surfaces.[18] The latter peak is seen only in samples exhibiting columnar morphology and grows with time upon exposure to air.

D. Electron Spin Resonance Measurements

Samples deposited on Corning 7059 glass substrates were used for the electron spin resonance (ESR) measurements. ESR was one of the first techniques applied to amorphous semiconductors since it provides information on the density of the paramagnetic defect centers.[21,69] The measurements were performed on a Bruker ER220 DSR X-band ESR spectrometer. To estimate the spin density, the ESR signal from the sample was compared to that of a Picein 80 standard having a known quantity of spins.

Magnetic resonance is observed in systems which possess a magnetic dipole moment $\boldsymbol{\mu}$. The magnetic moment $\boldsymbol{\mu}$ is related to the spin $\mathbf{S}$ by

$$\boldsymbol{\mu} = \gamma_g \hbar \mathbf{S} \qquad 3.14$$

where the gyromagnetic ratio γ_g is given by

$$\gamma_g = g(e/2m_e) \equiv g\beta \qquad 3.15$$

Here g is the so-called g-factor and m_e is the electron mass. $\beta = e\hbar/2m_e$ is called the Bohr magneton.

When a strong magnetic field $\mathbf{H}$ is applied to the system, the Zeeman interaction between the field and the magnetic moment

$$E = -\boldsymbol{\mu}.\mathbf{H} = -g(e\hbar/2m_o)mH, \qquad 3.16$$

where $-S \leq m \leq +S$ is an integer, splits the energy levels of the spin into 2S + 1 values. Transitions between the 2S + 1 Zeeman levels can

now be induced by applying an oscillating electromagnetic field at right angles to the magnetic field. The condition for resonance, then, is

$$\omega_0 = \gamma_g H = g\beta H \qquad 3.17$$

where ω_0 is the angular frequency of the electromagnetic field. When H $\simeq$ 0.33 T (as in this work), and g = 2.0023 (g-factor for free electrons), resonance occurs at 9.3 GHz (X-band). For NMR, the principle remains the same and resonance occurs in the radio frequency range since the nuclear masses are much larger than m_e.

The g-factor of the native paramagnetic defect in a-Si:H was found to be 2.0055. This value is independent of preparation conditions and is hence considered to be intrinsic to the material.[70] Comparison of ESR signal from a-Si with those of the dangling bonds present at the surfaces of Si/SiO_2 interfaces[71] and radiation damaged c-Si[72,73] has led to the suggestion that this resonance in a-Si:H is due to dangling bonds.

The ESR measurements were performed by inserting the sample in a microwave cavity placed in a strong magnetic field. The microwave frequency was set 9.3 GHz and the magnetic field was swept from 3330 G to 3350 G. A small modulation field of 4 Gauss was applied at a frequency of 100 KHz and a phase sensitive lockin technique was used to detect the signal. A spectrum proportional to the first derivative of the absorption was obtained and is shown in Fig. 3.7. The total number of spins in the sample N^S was calculated from[74]

$$N^S = N^r \frac{(\Delta H^S_{pp})^2}{(\Delta H^r_{pp})^2} \frac{(Y^S)}{(Y^r)} \frac{(H^r_{mod})}{(H^S_{mod})} \frac{(P^r_w)^{1/2}}{(P^S_w)^{1/2}} \frac{(\Lambda^S)}{(\Lambda^r)} \frac{(G^r)}{(G^S)} \frac{(N^r_p)}{(N^r_p)} \qquad 3.18$$

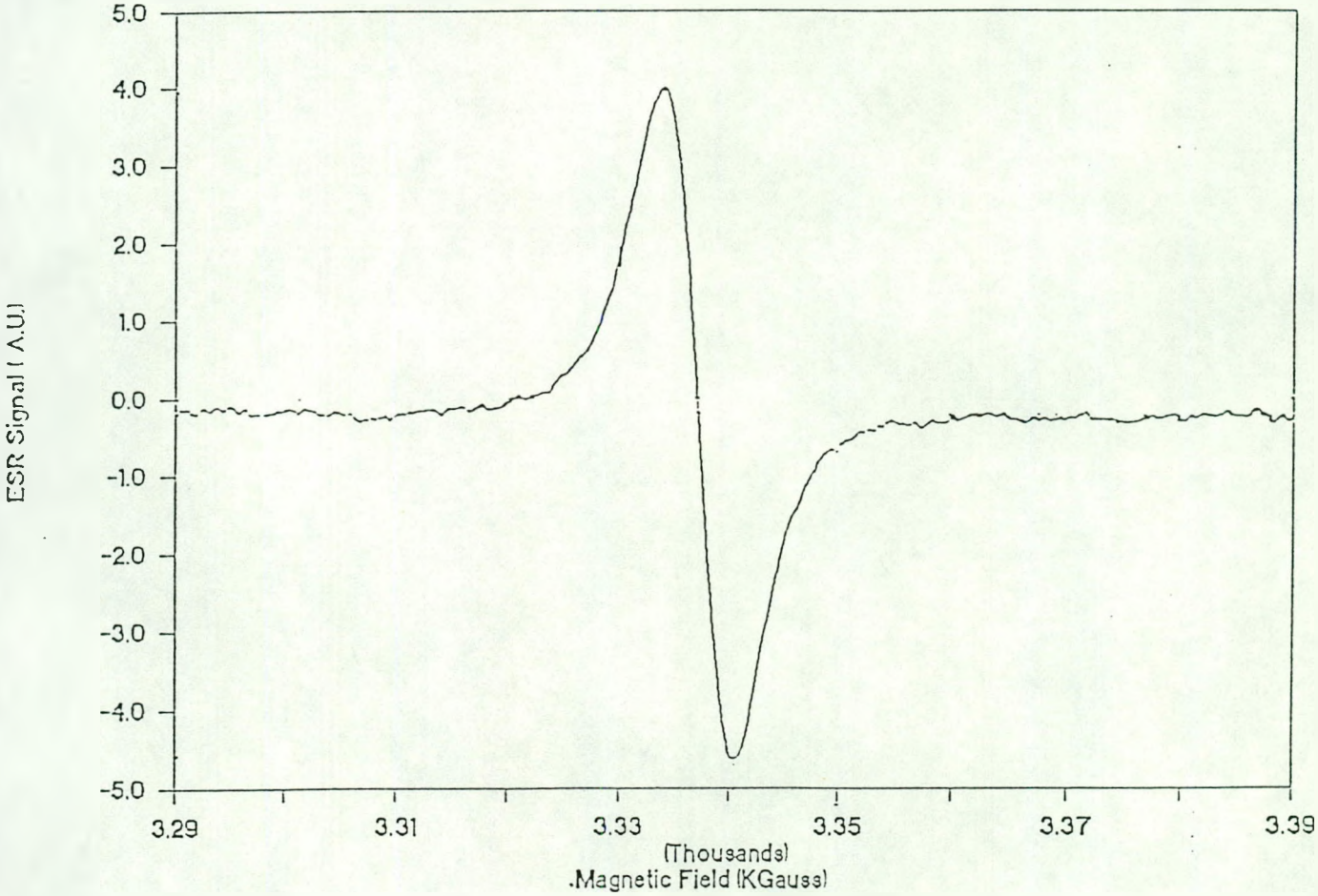

Fig. 3.7 The ESR signal of sample 108 (as deposited)

where the superscripts r and s denote the reference sample and a-Si:H sample, respectively. Here ΔH_{pp} is the derivative peak-to-peak width of the resonance, Y is the amplitude, H_{mod} is the magnitude of the modulation field, P_w is the power, Λ is the line shape factor, G is the lockin gain and N_p is the number of scans. Λ is 1.18 for a standard Gaussian and 3.63 for Lorentzian lines. Generally, the lineshapes were mixed and hence an interpolated value was used. For Picein 80 and a-Si:H, Λ was found to be 3.28 and ~ 1.6 respectively. The center of the resonance occurs at the value of the magnetic field where the derivative spectrum passes through the base line.

E. Secondary Ion Mass Spectrometry

Secondary Ion Mass Spectrometry (SIMS) is an analytical technique which is often used to characterize the surface or depth-profile the near-surface region of a solid.[1] It generally involves the use of a primary ion beam with energies between 0.5 - 20 keV to sputter off particles of atomic dimensions from the sample surface. The secondary ions thus produced are then detected using a mass spectrometer. The details of the experiment are discussed below. It should be noted that the process is partially destructive since a part of the sample is etched as it is depth-profiled.

Samples deposited on single crystal silicon substrates were used for the SIMS measurements. The instrument was a Perkin Elmer SIMS model PHI 6300. A schematic of the basic SIMS configuration is shown in Fig. 3.8.

---

[1]The SIMS measurements were performed by Dr. R. Shinar at the Microelectronics Research Center, Ames, IA 50011.

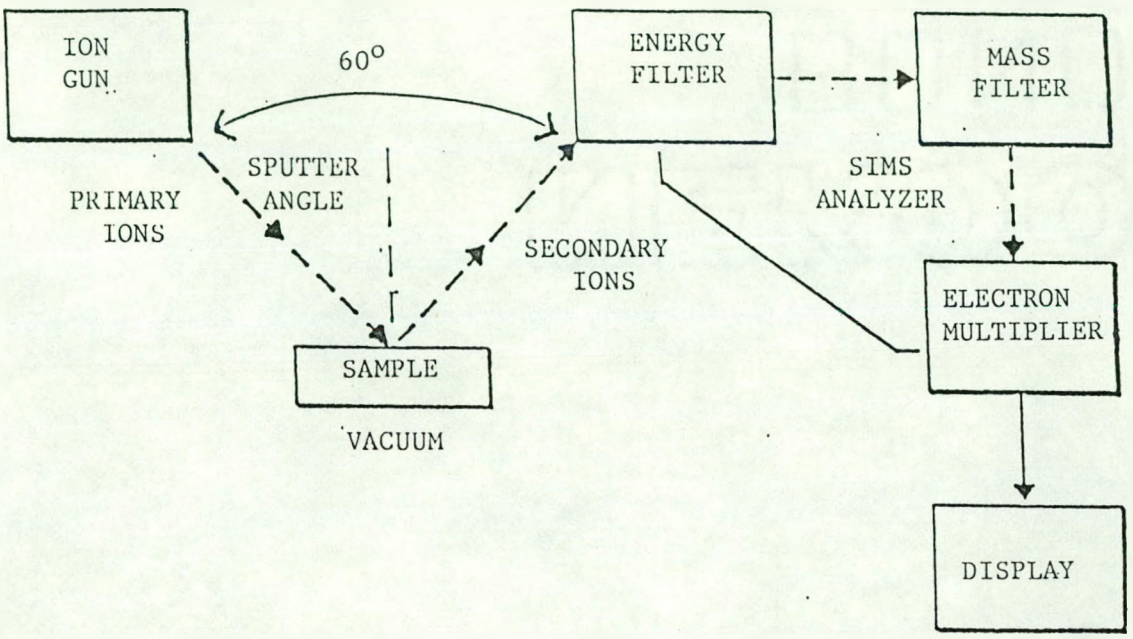

Fig. 3.8 A schematic of the basic SIMS configuration

A primary beam of positive cesium ions (Cs^+) ~ 50 - 60 μm in diameter having energies between 4 - 6 keV was incident on the sample surface at an angle of 30^o. This beam was used to raster a 500μm x 500μm area on the sample surface. The secondary ions from the sample surface were analyzed by the SIMS analyzer which consisted of an energy filter, a quadrupole mass filter and an electron multiplier for signal amplification. The instrument was operated under ultra-high vacuum (UHV) conditions. The depth profile of a a-Si:H/a-Si:(H,D)/a-Si:H multilayer is shown in Fig. 3.9. The sputtering time is plotted along the abscissa and the corresponding counts per second of either the deuterium or hydrogen along the ordinate. The film-substrate interface is determined from the sharp drop in the hydrogen concentration as seen in Fig. 3.9a. Knowledge of the sample thickness (from Dektak measurements) immediately yields both sputtering rate and the depth vs counts plot. The film-substrate interface also helped in determining the depth resolution of the profile. The depth resolution deteriorates as the etching process continues. The resolution was typically between 1% to 3% at the film-substrate interface for a ~ 1.5 μm thick sample.

To obtain depth profiles of more than one atomic species, concentration of the different masses are monitored sequentially. As the etching continues, the detected signal of the different species originates from increasingly greater depths from the sample surface. For accurate depth profiles, two key conditions must be met. First, the analysis area must be bombarded uniformly. This criteria is met by ensuring that both the primary beam current and the ion impact energy is kept constant throughout the analysis. The beam current, which was

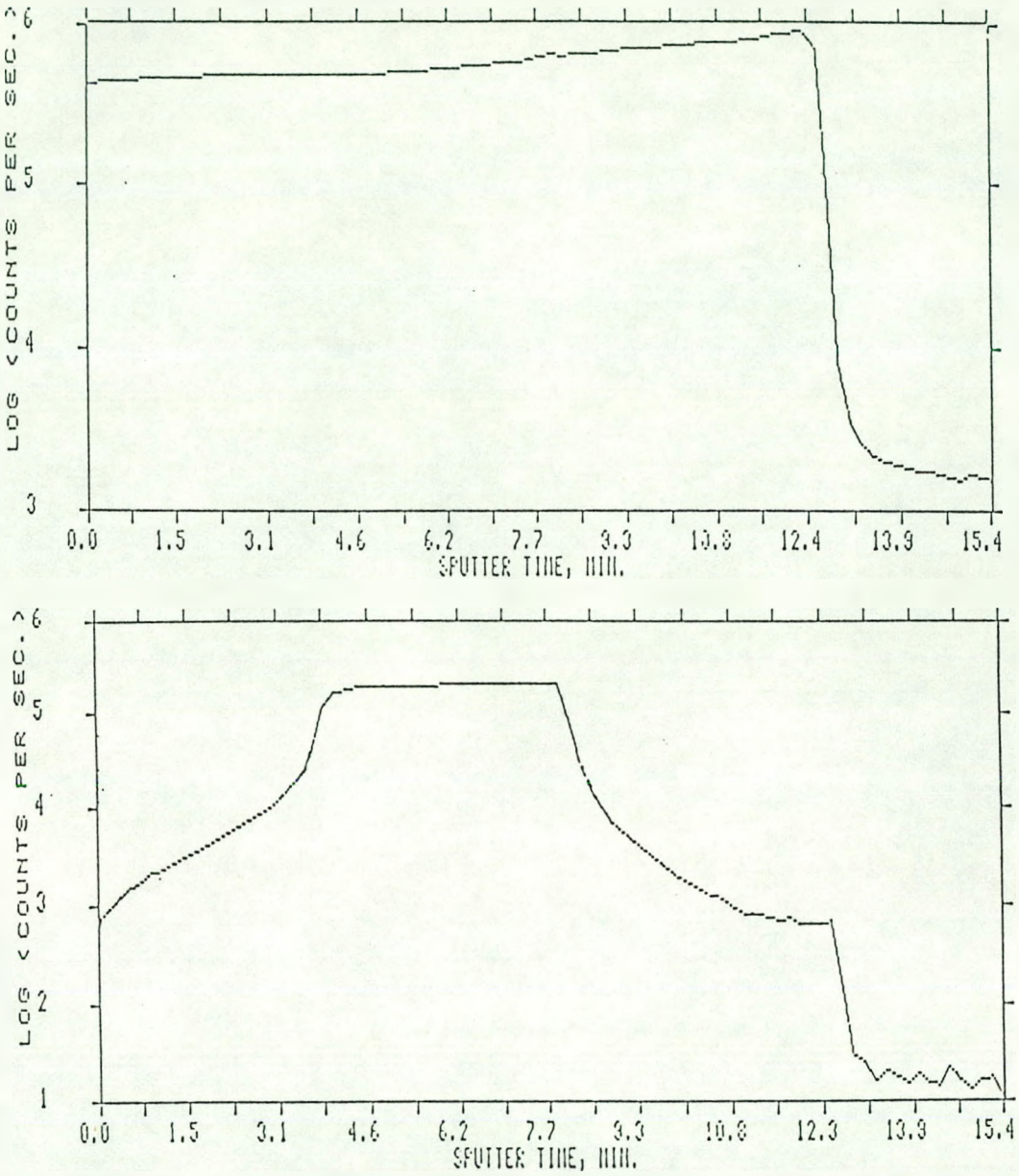

Fig. 3.9 The depth profile in sample 29 annealed at 300°C for 6 hrs as measured by the SIMS of (a) hydrogen, and (b) deuterium

maintained between 500 nA to 700 nA, determined the number of ions incident on the sample surface per second. Since the substrates were not biased for these measurements, the impact energy was equal to the primary beam energy. Secondly, the contribution of ions from the crater walls must be minimized. To achieve this objective electronic gating was employed so that the measured signal originated from typically a 125μm x 125μm area located at the center of the crater. A profile of a typical crater is shown in Fig. 3.10. The raster width is the distance between the 50% points. The beam diameter is estimated from the sloping sidewalls of the crater as measured by the profilometer between the 16% and 84% points and is found to be ~ 55 μm. The beam size increases with the primary beam current and this is demonstrated in Fig. 3.11 for a Cs^+ source in a Perkin Elmer PHI 6300 instrument.[75] The flat crater floor suggests that sputtering was uniform.

The true shape of the depth profile can often be distorted. It depends critically on the physics of sputtering and the shape of the sputtered crater. When energetic ions from the primary beam are incident on the sample surface, "mixing" of atoms take place. Three different types of mixing processes have been identified[76]: recoil mixing, cascade mixing, and radiation-enhanced diffusion (RED). Recoil mixing, an anisotropic effect, occurs when surface sample atoms are driven into the sample due to direct collisions with the primary ions. Cascade mixing is an isotropic effect and is due to the motion and collision of the sample atoms with each other. In this process the subsurface atoms are moved to the surface and viceversa. RED is thermally activated diffusion enhanced by higher than equilibrium

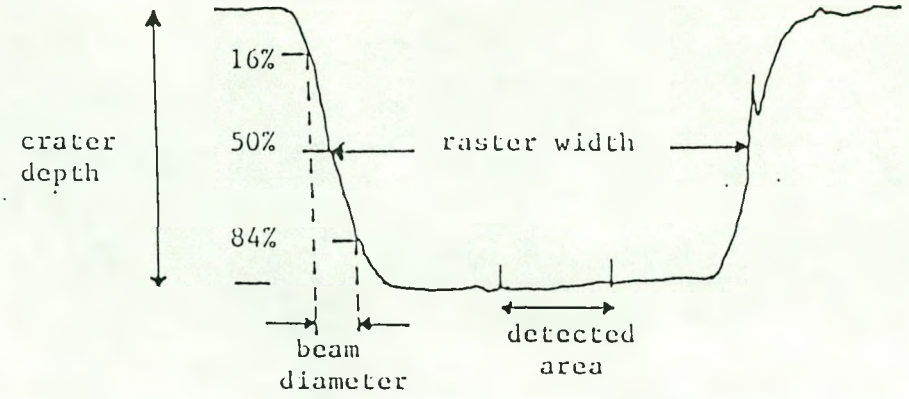

Fig. 3.10 The profile of a crater etched away by the SIMS in sample 94. Note the sloping crater walls and the flat crater floor

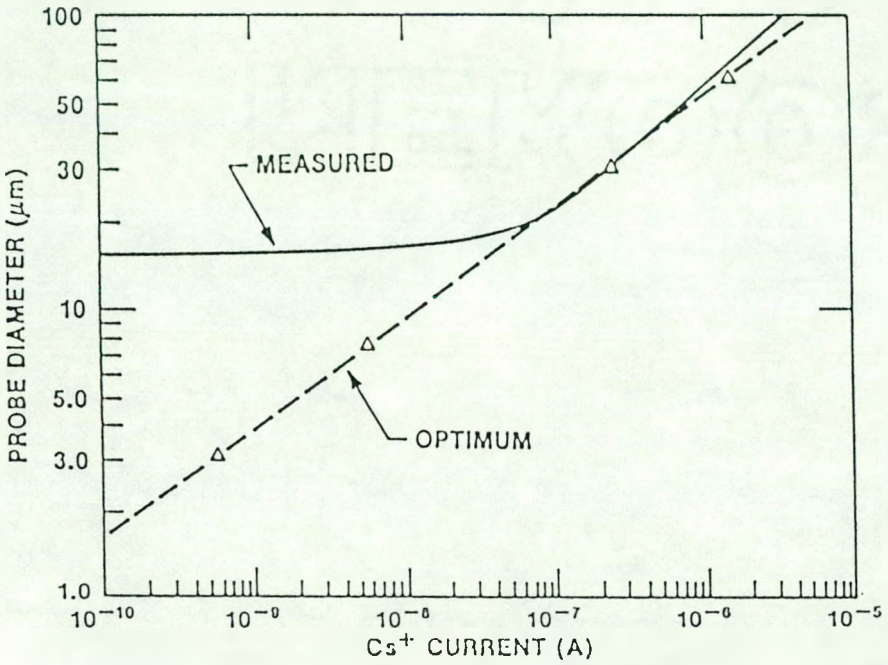

Fig. 3.11 Probe diameter relatioship to Cs^+ ion current for Perkin Elmer PHI 6300 Cs source (from ref. 73)

density of defects. The distance over which the ion mixing effects take place is called the penetration depth. For Cs^+, the penetration depth R is given by[77]

$$R(\text{in Å}) = 18.38\ E^{0.68}\ \text{Cos}\Theta \qquad 3.19$$

where E is the impact energy of the primary beam ions (in keV) and Θ is the angle of incidence. For unbiased samples with E between 4 - 6 keV and $\Theta = 30^o$, as in our work, R lies between 40 - 54 Å. The penetration depth (and hence the ion mixing effects) can be decreased either by decreasing the ion beam current density (primary beam current divided by the raster area) and the primary beam energy or by increasing the angle of incidence. This leads to a slower sputter-etching rate and an improvement in the depth resolution since the depth between data points is reduced. A lower sputter-etching rate also lowers the counting rate and hence avoids saturation problems for the high content isotopes. However, the penalty paid is in the sensitivity which decreases with decreasing sputter-etching rate. Thus in choosing the various parameters a balance must be reached among the depth resolution, detection limit, and the time available for the experiment.

It should be noted that in this work, a primary beam of Cs^+ was used since only negatively charged secondary ions were detected. The SIMS analyzer can distinguish between the various species only by their m/e ratio. Hence, deuterium was detected by its negative ion D^- (m/e = -2) which has a greater dynamic range than the D^+ ion since interference from the H_2^+ ion is eliminated. Note that for both D^+ and H_2^+ ions m/e = +2.

SIMS was also used to determine the boron content in the boron-doped films. This was done by comparing the boron count of the samples with that of an ion implanted standard. The standard used in this work was a crystalline silicon wafer in which boron was implantated at 40 keV at a flux of ~ 10^{14} cm^{-2}. The depth profile of boron in the standard is shown in Fig. 3.12. The peak concentration corresponds to ~ 1.27 x 10^{19} cm^{-3}. A duoplasmatron employing O_2^+ ions was used for the B-level determination.

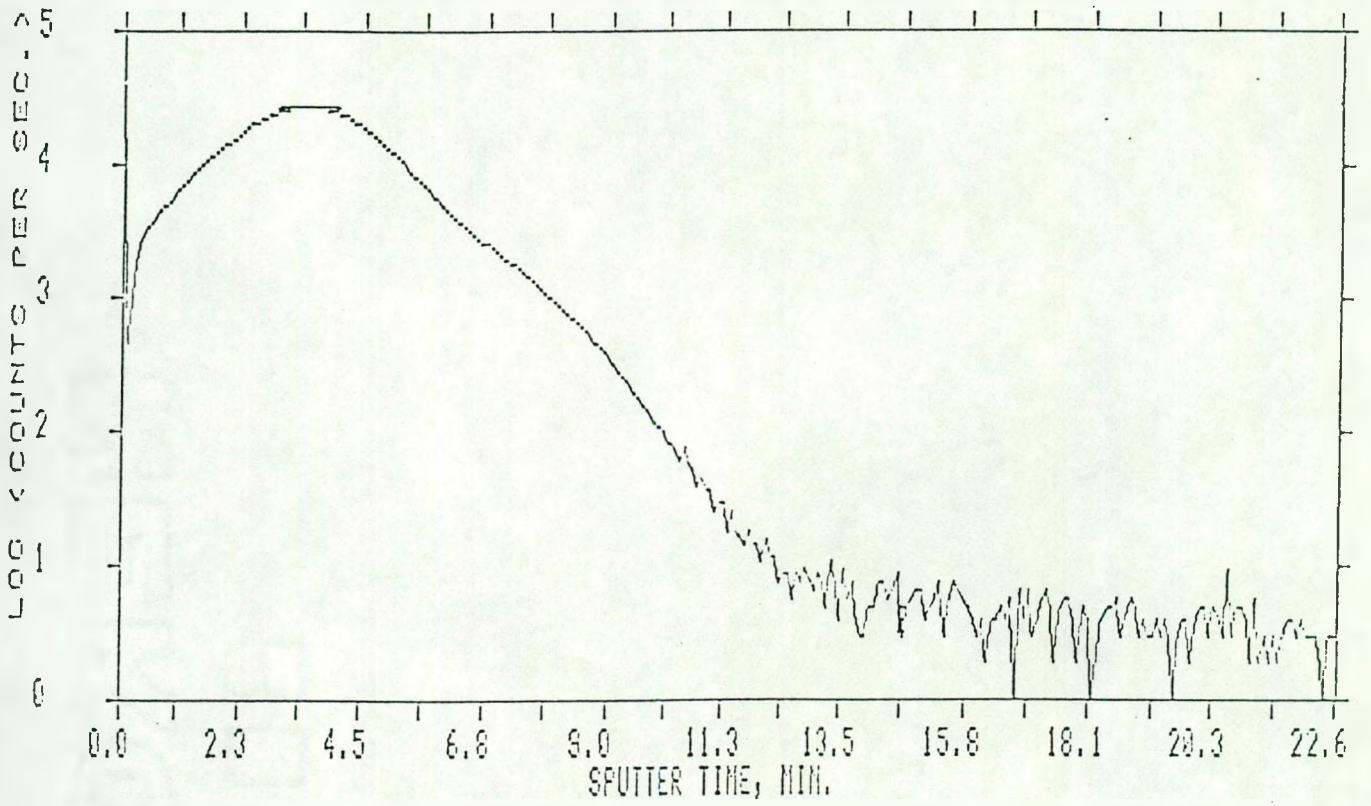

Fig. 3.12 Depth profile of boron in an ion implanted c-Si standard. The peak corresponds to 1.27×10^{19} atom cm^{-3}

IV. RESULTS AND DISCUSSION

A. General Comments

Undoped and boron-doped rf multilayered samples for hydrogen diffusion studies were prepared by rf sputter deposition.[1] The hydrogen content [H_T] and the boron content of the films was varied systematically by changing either the sputtering power or the partial pressure of the desired gas, or both.

As mentioned in Chapter II, diffusion was studied on two types of multilayered samples. Following Carlson and Magee (CM),[78] the initial samples were a-Si:H/a-Si:D/a-Si:H multilayers. During the preparation of the middle layer, the hydrogen flow was cut off while the deuterium was turned on. The partial pressure of deuterium was at least equal to that of hydrogen. The samples were then annealed at different temperatures for various anneal times in sealed, evacuated pyrex tubes to avoid oxidation.

Initial results indicated that hydrogen diffusion depended critically on the films' microstructure and hence on [H_T]. Consequently, all samples that were subsequently deposited were a-Si:H/a-Si:(H,D)/a-Si:H multilayers. During the preparation of these samples, the hydrogen was allowed to flow uninterrupted while deuterium was added in the middle layer. However, its partial pressure was much lower than that of hydrogen and hence its addition would have little

---

[1] A glow discharge sample (#33) with [H_T] ~ 9% was also studied. This sample was prepared by R. F. Girvan at the Microelectronics Research Center, Ames, IA 50011.

effect on the hydrogen microstructure. Using this method of deposition, the microstructure of hydrogen in the samples could be varied systematically. These samples were also annealed in sealed, evacuated pyrex tubes.

In either type of multilayers, the deuterium profiles of the as deposited samples looks identical. Ideally, the concentration of deuterium in both the top (left) and bottom (right) layer is zero while that in the middle layer is constant. Upon annealing, however, the interfaces become increasingly smeared. The equation describing the smeared profile was obtained from the solution of the diffusion equation[79]

$$\frac{\partial c(x,t)}{\partial t} = D \frac{\partial^2 c(x,t)}{\partial x^2} \qquad 4.1$$

subject to the appropriate boundary conditions. In the above equation, D is the diffusion constant and c(x,t) is the concentration of deuterium at a distance x from the interface (x = 0) at time t.

The boundary conditions of a semi-infinite solid were applied at the two interfaces. For example, the boundary conditions at the bottom interface are:

$$c(x,0) = 0; \quad x > 0$$
$$= c_o; \quad x < 0 \qquad 4.2a$$

and

$$c(x,t) \rightarrow 0 \text{ as } x \rightarrow \infty \text{ for all } t. \qquad 4.2b$$

The boundary conditions at the top interface are similar except that x is now replaced by -x. The solution to Eq. (4.1) is then described by a complementary error function[79]

$$c(x,t) = c_o/2 \ \mathrm{erfc}[x/2(Dt)^{1/2}] \qquad 4.3$$

where c_o is the concentration of deuterium at $x = -\infty$ (the maximal deuterium concentration) and t is the time of anneal. Up to this point in the analysis, it has been assumed that the diffusion constant D is independent of time and position. However, if D does depend on time, as is the case of hydrogen diffusion in a-Si:H, then the above equation is modified to

$$c(x,t) = c_o/2 \ \mathrm{erfc}[x/2(\theta(t))^{1/2}] \qquad 4.4$$

where

$$\theta(t) = \int_0^t D(\tau)\, d\tau \qquad 4.5$$

Note that $\theta^{1/2}$ has dimensions of length and is an estimate of the distance through which deuterium diffuses in the sample. The above equation, when combined with Eq. (1.3), yields an explicit time dependence for θ:

$$\theta(t) = \theta_o \ t^{1-\alpha} \qquad 4.6$$

where θ_o is a constant.

The diffusion profiles were fitted to Eq. (4.4) and the various values of θ were extracted from samples that were annealed at the same temperature but for different times. α could then be determined from the slope of $\log\theta(t)$ versus $\log(t)$ (Eq. 4.6). Note that $\alpha = 1$ would

Page(s) Missing

from

Original Document

B. Undoped a-Si:H

Undoped samples were prepared under varying deposition conditions. Throughout this work the partial pressure of the sputtering gas (argon) was maintained at 10.5 ± 1.0 mT. The other parameters like hydrogen partial pressure, rf power, and the target to substrate distance were varied systematically to change the total hydrogen content [H_T] and the hydrogen microstructure.

1. Sample characterization

The deposition parameters of the undoped samples are summarized in Tables IV and V. Samples deposited with a target to substrate separation (d) of 1" are listed in Table IV. The only exception was sample 27 which was prepared at d = 2". Samples deposited at a slightly greater separation of 1.25" are listed in Table V. All samples, except # 106, were deposited on unheated substrates. Heating was accomplished by placing a copper plate on a piece of machined ceramic block. The substrates were placed on the copper plate and the ceramic block was heated with a tungsten filament. The temperature was then measured with a chromel-alumel thermocouple immediately after the rf power was turned off at end of the deposition run. Hence the temperature of the substrates during the depositon is an estimate only.

The dependence of the deposition rate R on transmitted rf power for samples deposited at 1 and 1.25" is plotted in Figs. 4.1 and 4.2 respectively. Fig. 4.1 also shows the dependence of [H_T] on rf power. For this plot only the total hydrogen content of samples 108-112 were used. These samples were bilayers with deuterium deposited in the top

Table IV. Deposition parameters, total Si-bonded H and di-H content of as-deposited films ($[H_T]_o$ and N_{do} respectively, spin density N_s and optical gap (E_g) of undoped samples deposited at ~ 10 mT of argon with a target to substrate separation of 1"

Sample #	rf Power (W)	Partial Pres. H_2 (in mT)	Partial Pres. D_2 (in mT)	Thickness (μ)	Dep. rate (Å/s)	$[H_T]_o$ (at. %)	N_{do} (at. %)	N_s (cm^{-3})	E_g (eV)
11[a]	50	1.5	3.0	1.8	0.89	22	11		
13[a]	500	1.5	2.5	1.1	4.70	14	3.5	5.0×10^{17}	
21[b]	200	0.80	0.20	0.96	1.97	19	9	2.3×10^{17}	1.8
22[b]	550	0.80	0.22	0.80	5.56	13	2.5	9.8×10^{16}	1.75
23[b]	50	0.78	0.22	0.52	0.64	33	11		
27[b,c]	550	0.50	0.20	1.15	4.5	17	4		
29[b]	550	0.52	0.20	0.7	3.9	19	5		
108[d]	200	0.52	0.042	1.1	1.67	16		3.3×10^{18}	1.63
109[d]	600	0.54	0.045	1.0	4.17	9			1.46
110[d]	500	0.56	0.042	0.88	3.18	7.9		2.2×10^{18}	
111[d]	300	0.54	0.046	1.1	2.40	14			1.58
112[d]	400	0.57	0.044	1.25	3.70	8.5			

[a]H/D/H multilayers.

[b]H/(H,D)/H multilayers.

[c]Target to substrate distance 2".

[d](H,D)/H multilayers.

Table V. Deposition parameters, total Si-bonded H and di-H content of as-deposited films ($[H_T]_o$ and N_{do} respectively, spin density (N_s) and optical gap (E_g) of undoped samples deposited at ~10mT of argon with a target to substrate separation of 1.25"

Sample #	rf Power (W)	Partial Pres. (in mT) H_2	Partial Pres. (in mT) D_2	Thickness (μ)	Dep. rate (Å/s)	$[H_T]_o$ (at. %)	N_{do} (at. %)	N_s (cm^{-3})	E_g (eV)
81[a]	550	0.15	0.04	1.5	3.79	2	-	1.9×10^{18}	
84[a]	550	0.35	0.05	2.4	4.40	4.5	-	7.2×10^{15}	
89[b]	550	0.18	-	0.84	4.7	3.6	-	3.8×10^{18}	1.31
90[b]	550	0.29	-	0.64	3.9	6.5	-		1.35
91[b]	550	0.40	-	0.73	4.5	5.9	-		1.41
92[b]	550	0.20	-	0.50	3.3	5.7	-		1.32
93[b]	550	0.29	-	0.53	3.5	4.8	-		1.37
95[c]	550	0.11	0.025	8.8	3.9	1.0	-		
96[c]	450	0.15	0.035	8.0	3.3	2.1	-		
97[c]	350	0.20	0.048	12.5	3.2	3	-		
99[c]	200	0.41	0.09	6.7	1.62	10.7	0.5		
100[c]	100	0.50	0.12	6.0	1.04	16.5	2.2		
102[c]	300	0.31	0.071	7.5	2.55	6.1	-		
104[c]	50	0.65	0.17	3.4	0.79	23	8.1		
106[b,d]	400	0.34	-	0.7	2.6	22	1.7	4.8×10^{17}	

[a]H/(H,D)/H multilayers.

[b]Hydrogenated single layer.

[c](H,D)/H multilayers.

[d]Substrate temperature ~206°C.

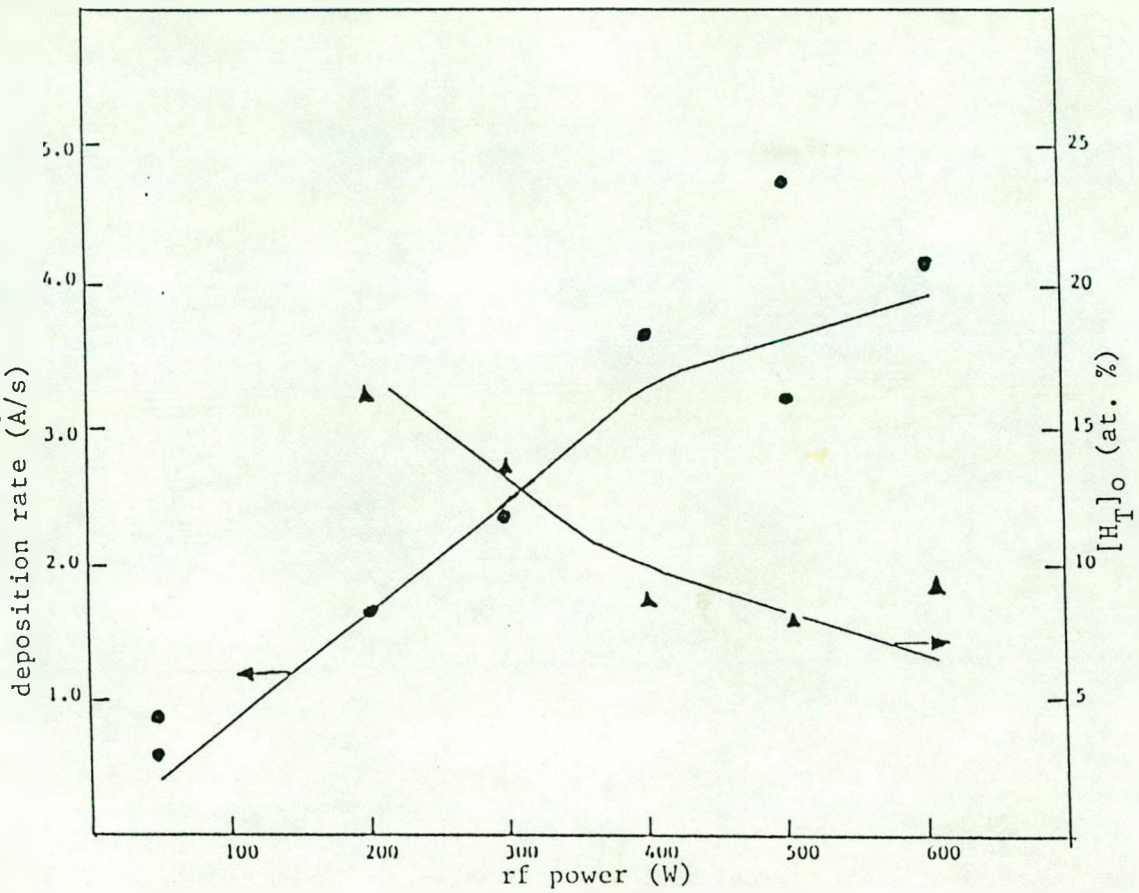

Fig. 4.1 Deposition rate and the total hydrogen content $[H_T]_o$ at different rf powers for films deposited at d = 1".

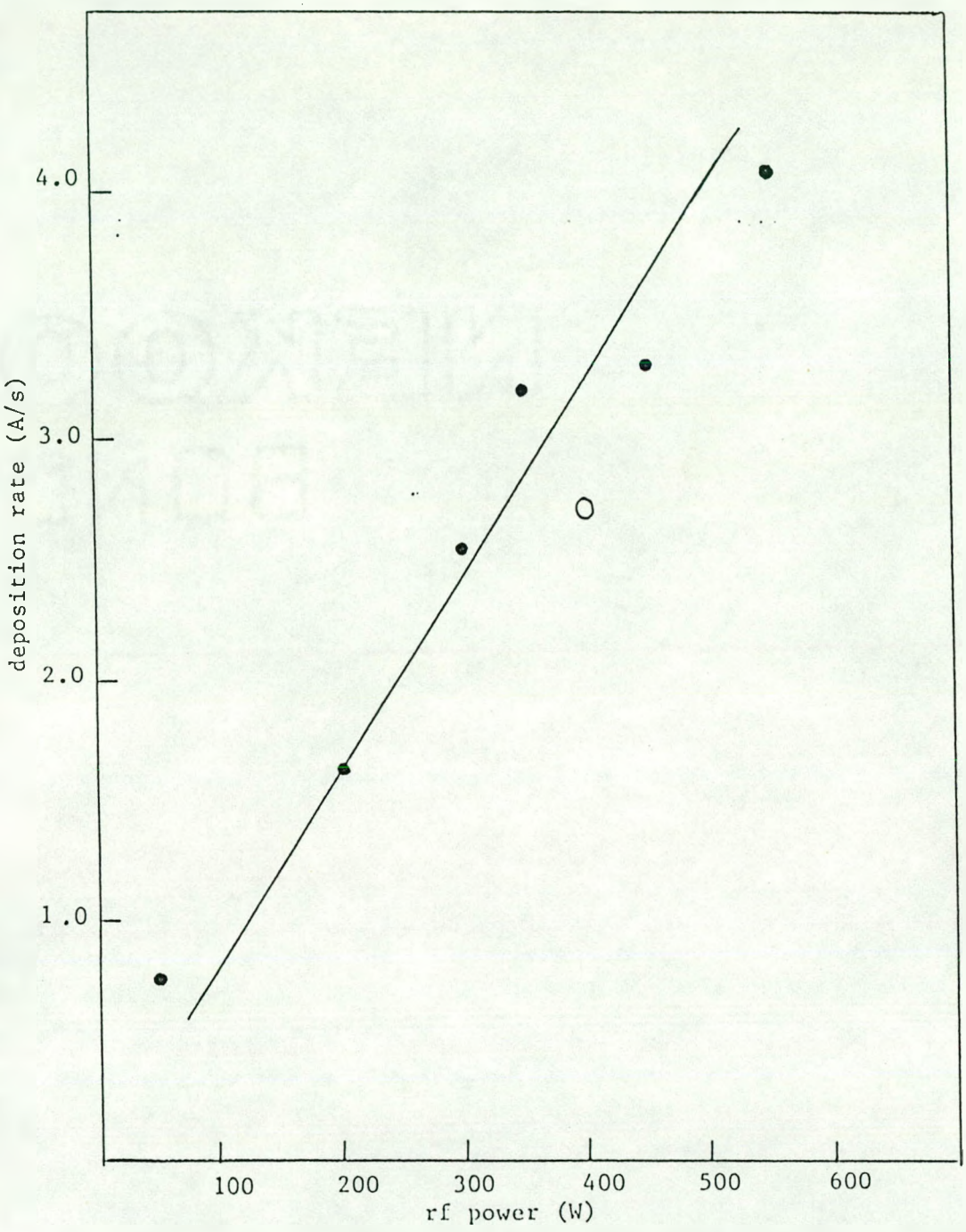

Fig. 4.2 Deposition rate at different rf powers for films deposited at d = 1.25".

layer. The partial pressure of hydrogen was maintained at a constant value of 0.54 ± 0.03 mT while the rf power was varied. As expected, R generally increases with increasing power. However, at d = 1", it tends to flatten out beyond 450 W. This result is in qualitative agreement with Fig. 2.4 which shows a similar dependence of the sputtering yield with increasing incident ion density. In Fig. 4.2, R continues to increase linearly throughout the entire range. It is interesting to note that the scatter in the data increases at high rf powers. This is perhaps due to an increase in the plasma-film interaction at higher powers. For d = 1", resputtering processes are stronger and this is exhibited in the nonlinear behavior of R at 450 W and beyond. This nonlinearity is also reflected in the dependence of $[H_T]$ with rf power (Fig. 4.1).

The optical gap E_g of the samples depends essentially on the total hydrogen content. This is demonstrated in Fig. 4.3 which is a plot of E_g versus $[H_T]$. It shows that E_g generally increases with increasing hydrogen content. Note that samples deposited at various transmitted powers and target-to-substrate separation have been included in this figure.

Unlike E_g, the density of the paramagnetic centers do not show a clear correlation with $[H_T]$. Figs. 3.7 and 4.4 show the typical ESR signal for two as deposited samples with spin densities of 3.3×10^{18} and 4.8×10^{17} cm^{-3} respectively. Upon annealing the samples for 40 minutes at 300° C and 290° C respectively, the ESR signal was drastically reduced by an estimated one to two orders of magnitude (Figs. 4.5 and 4.6). The ESR data presented in this work is

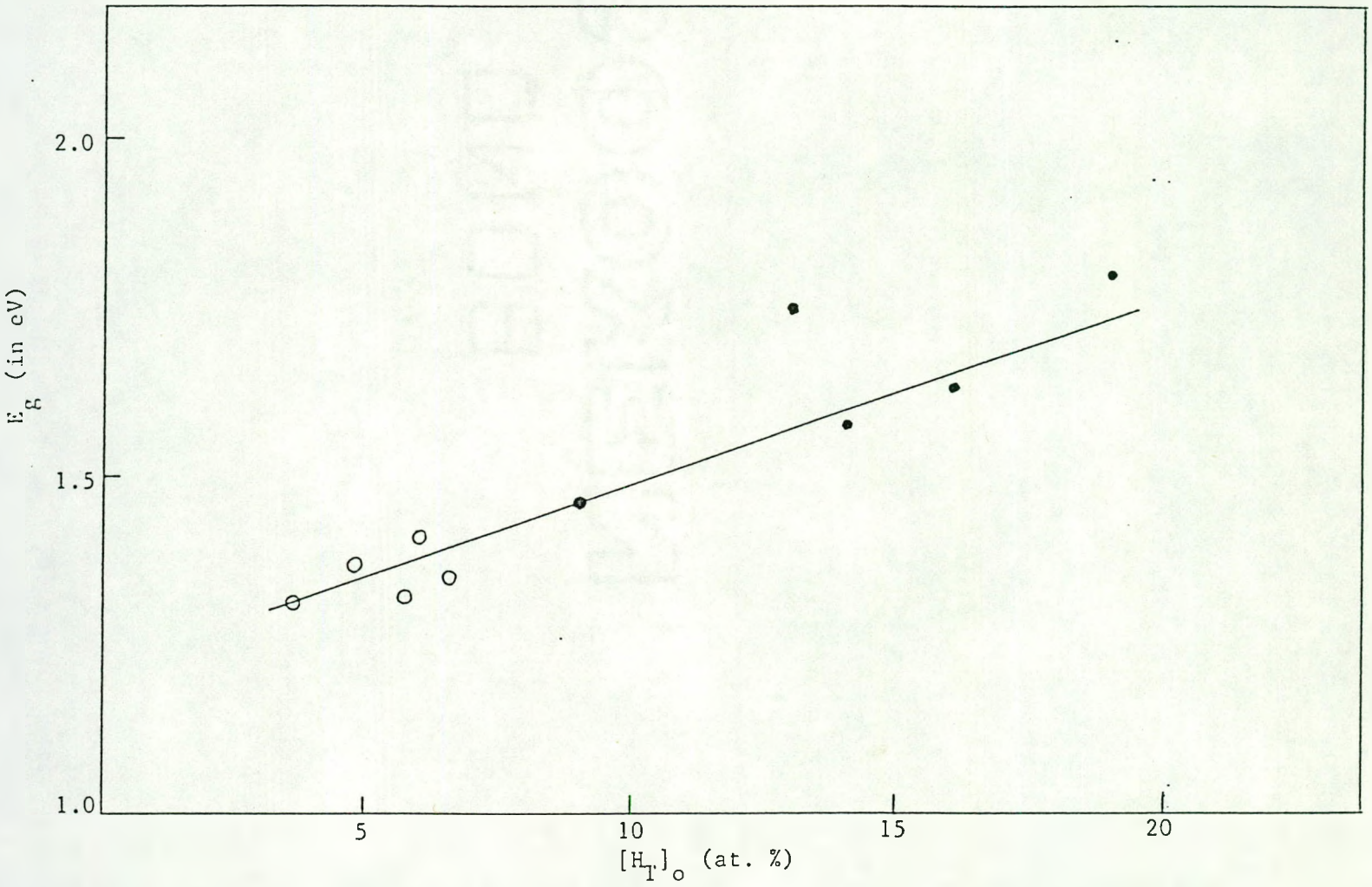

Fig. 4.3 Optical gap versus hydrogen content. (Solid and open circles represent samples deposited at 1.0" and 1.25" respectively).

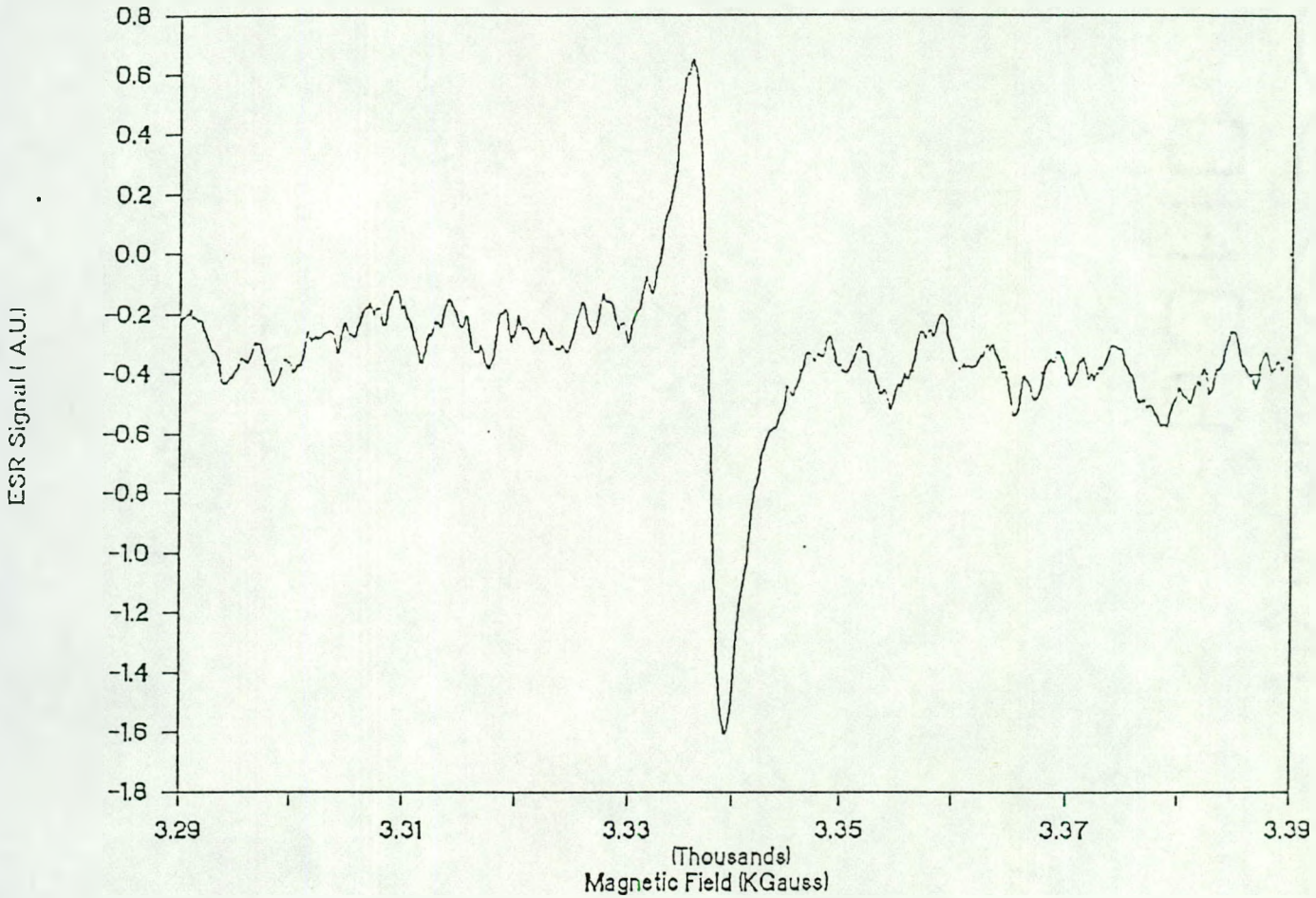

Fig. 4.4 ESR signal of sample 106 (as deposited).

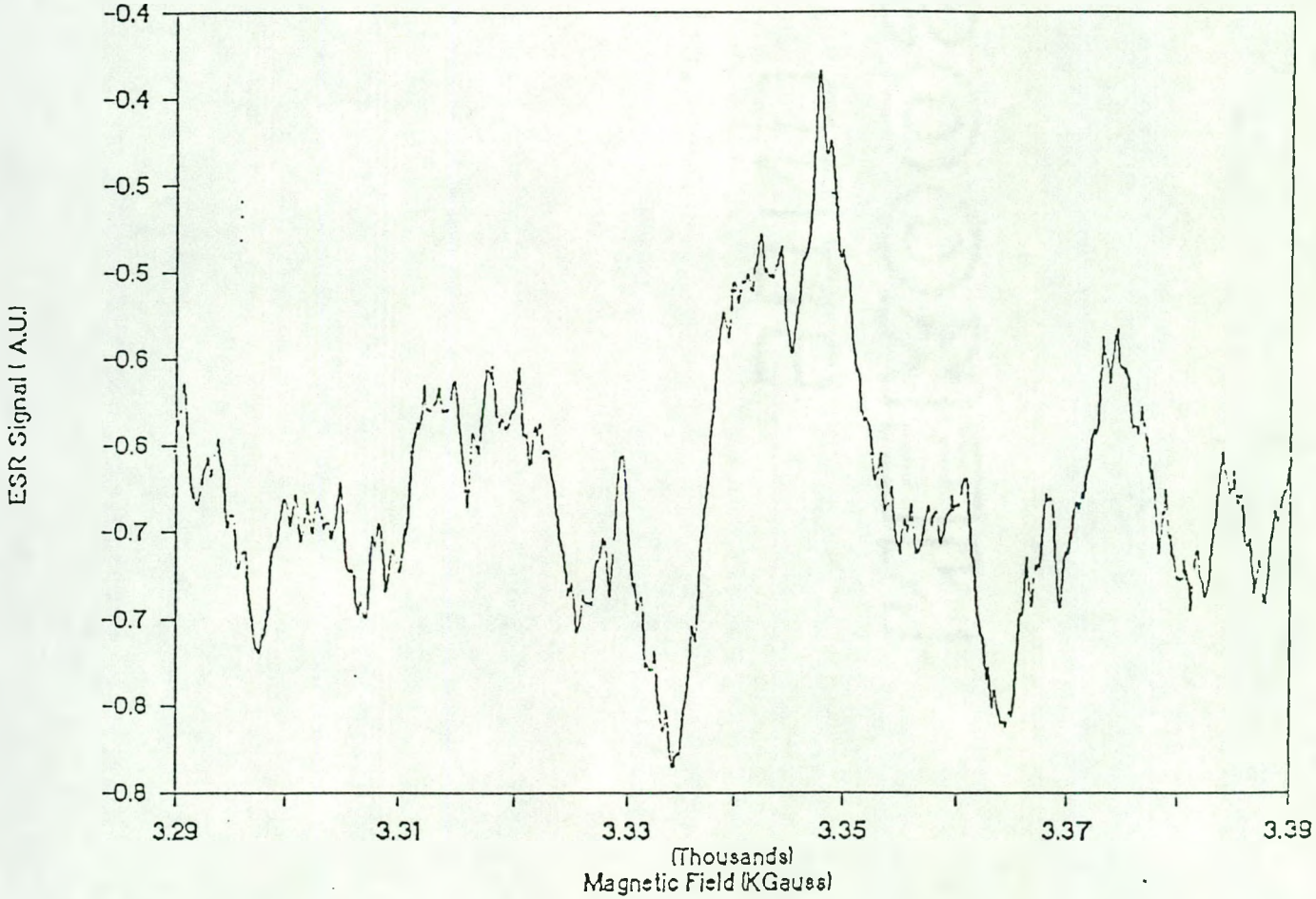

Fig. 4.5 ESR of sample 108 after annealing at 300°C for 40 mins. Since the signal to noise ratio is ~ 1, the calculated spin density is an upper limit of the actual value

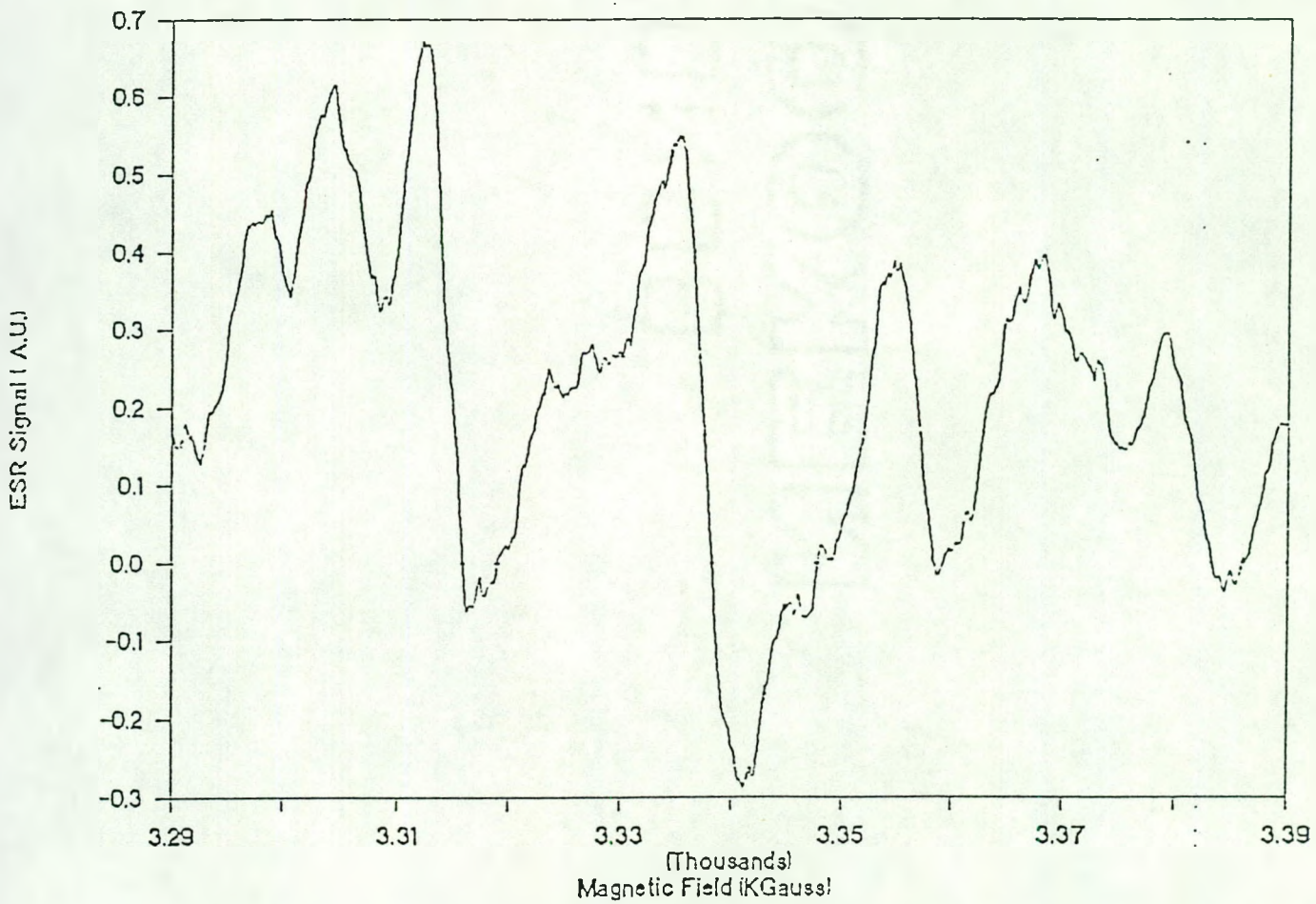

Fig. 4.6 ESR of sample 108 after annealing at 290°C for 40 mins. Since the signal to noise ratio is ~ 1, the calculated spin density is an upper limit of the actual value

complementary to that of Albers.[18] For argon sputtered samples, he showed that the spin density decreased sharply when the rf power increased from 50 W to 300 W. Beyond 300 W, the spin density increased gradually. Since all the samples that were studied by Albers were deposited at a constant target to substrate separation and hydrogen partial pressure, this minima in the spin density was also reflected in the plot of the spin density versus $[H_T]$. In this work many of the parameters mentioned above were varied simultaneously (including the substrate temperature in the case of sample 106). The microstructure of the samples is now a complex function of all the deposition parameters and hence it is hardly surprising that no correlation is seen between the spin density and $[H_T]$.

2. Hydrogen diffusion results

Multilayered samples were deposited on both glass and c-Si (polished on both sides) substrates. While the samples on glass substrates were used for thickness, optical gap and spin density measurements, samples deposited on c-Si were used exclusively for IR and SIMS experiments. Silicon wafers were cut to small pieces roughly 1/4 x 1/4 cm^2. A typical deposition run had 15 - 20 small wafers of c-Si and a few pieces of Corning 7059 glass. One or two such wafers were set aside to be used as references for the IR measurements.

To check the uniformity of deposition and hydrogen microstructure, the IR of two or more randomly selected as-deposited samples was always measured. The results have consistently showed that both $[H_T]_o$ and N_{do} exhibited no variation from sample to sample (within experimental

uncertainty) of the same deposition process. The depth profiles of H, D, O and Si were also measured by SIMS. The flatness of these depth profiles confirmed that the partial pressures of H and D remained aproximately constant during the run. Oxygen contamination and the sharpness of the interfaces were also checked. Hydrogen diffusion experiments were done only on samples with sharp interfaces and little ($\leq$ 0.2 at. %) oxygen contamination.

The samples were annealed and after each annealing step the IR spectra and the diffusion profiles were monitored. However, for samples 11, 13 and 22 the IR was not checked after annealing. Since the experiments on these samples were done at the very beginning, the importance of hydrogen microstructure on hydrogen diffusion was not realized. The total hydrogen content $[H_T]_a$, the content of silicon bonded to di- and tri-H N_{da} and changes in the shape of the stretch peak were closely monitored after each annealing step.

The deuterium depth profile of a typical sample annealed at 300° C for a two different anneal times (one short and one long) are shown in Figs. 4.7 and 4.8 respectively. The fits to the complementary error function (Eq. 4.4), for all samples, were generally good and usually excellent. The diffusion results for the undoped samples have been summarized in Table VI. The presentation and discussion of these results have been broadly divided into two subsections: samples with $[H_T]_o$ > 10% and those with $[H_T]_o$ < 10%. Since the total hydrogen content in device quality material is ~ 10%, samples of the former type are defined as (rather arbitrarily) as "hydrogen rich" and the latter as "hydrogen poor".

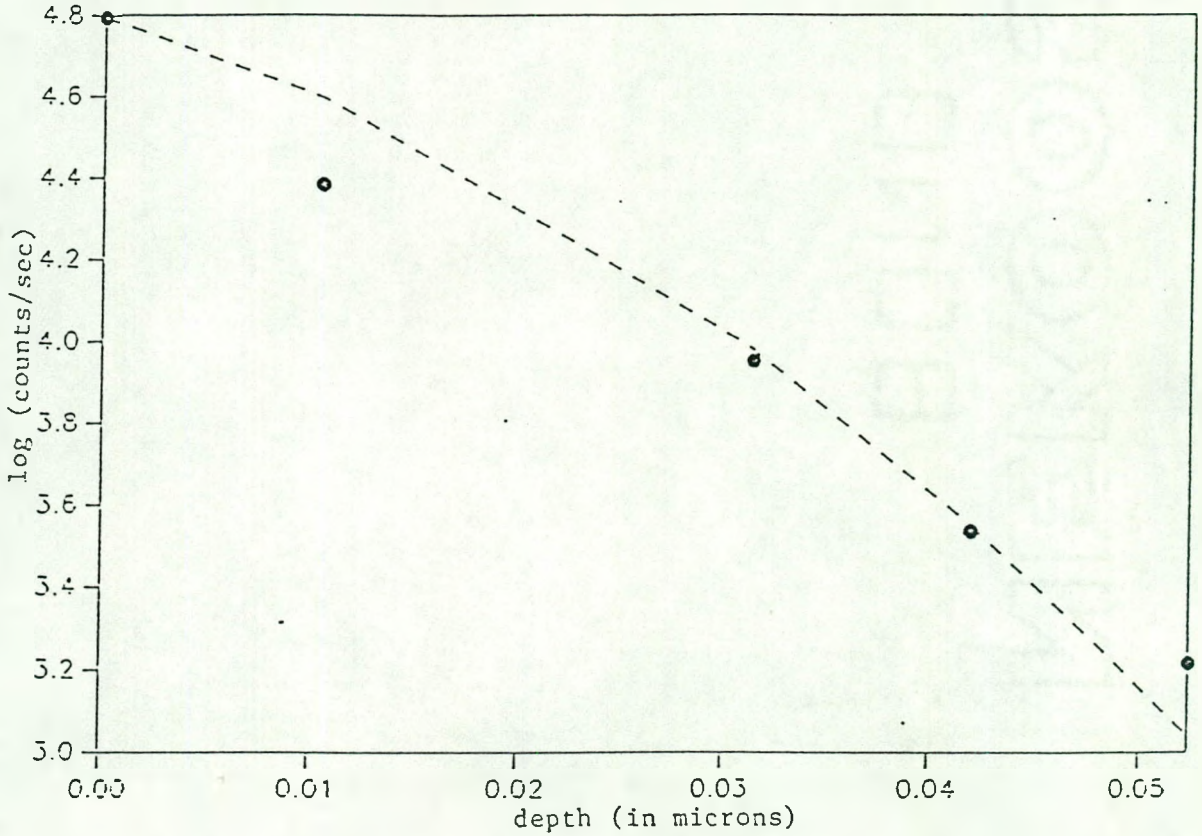

Fig. 4.7 The depth profile of deuterium (solid circles) and its fit (dashed curve) for sample 84 after annealing for 24:20 hrs at 300°C. Note $\Theta = 2.4 \times 10^{-12}$ cm^2.

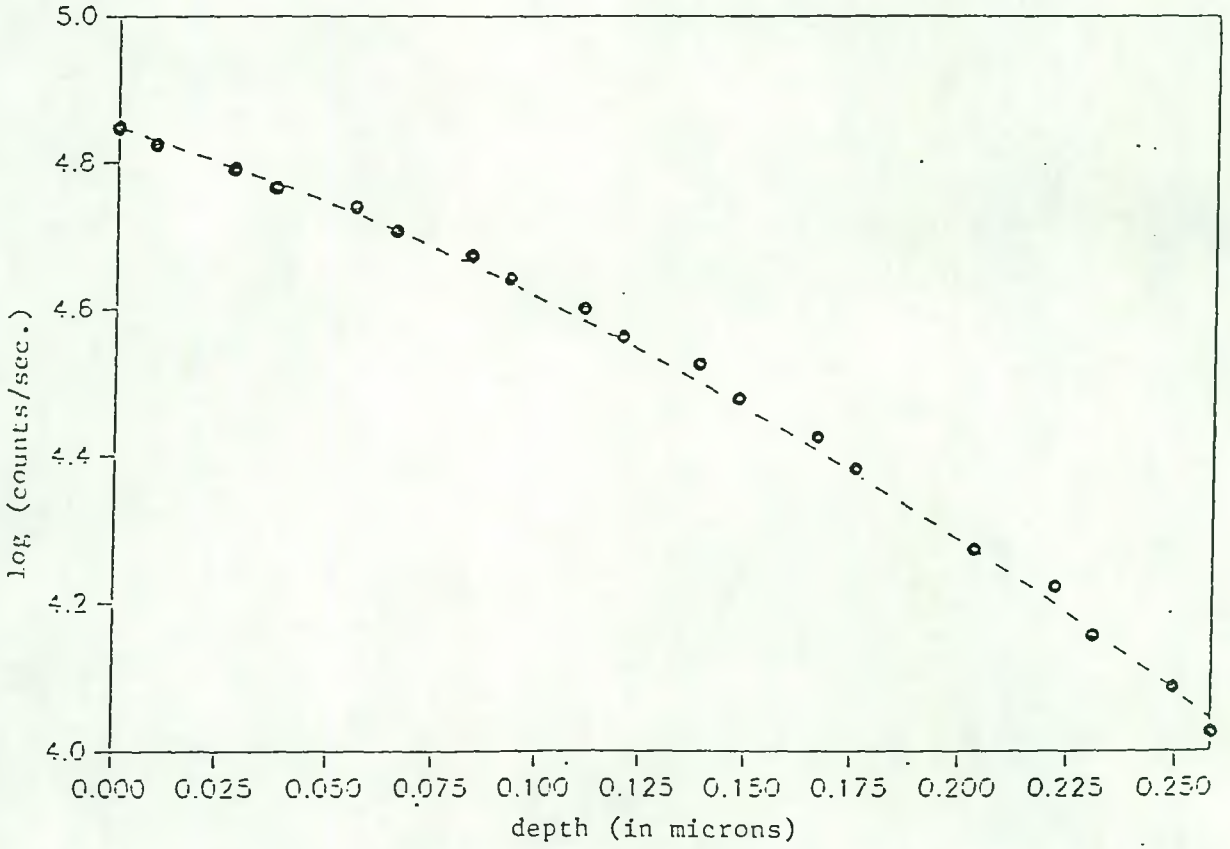

Fig. 4.8 The depth profile of deuterium (solid circles) and its fit (dashed curve) for sample 84 after annealing for 723:43 hrs at 300°C. Note $\theta = 1.7 \times 10^{-10}$ cm^2.

Table VI. Total Si-bonded H and di-H of annealed films ($[H_T]_a$ and N_{da} respectively), primary (ν_1) and secondary (ν_2) stretch peaks, and presence (+) or absence (-) of long-range H motion

Sample #	$[H_T]_a$ (at. %)	N_{da} (at. %)	$[H_T]_a/[H_T]_o$ (%)	N_{da}/N_{do} (%)	ν_1 (cm^{-1})	ν_2 (cm^{-1})	Diffusion (+/-)
11[a]					2093		-
13[a]					2000		+
21[a]	13	3	68.4	33.3	2045	2100	-
22[a]					2000		+
23[a]	20	5.5	60.6	50.0	2080		-
27[a]	11.5	3.5	67.6	87.5	2080	2000	+
29[a]	13.2	5	69.5	58.0	2022	2000	+
33[b,c]	9		NC[d]		2000		+
81[b]	2.5		NC		2000		+
84[b]	4.5		NC		2000		+

[a]Hydrogen rich samples
[b]Hydrogen poor samples (see text for details)
[c]Glow discharge deposited sample
[d]No change

Hydrogen rich samples It is clear from the above table that not all samples exhibit diffusion. Figs. 4.9 - 4.11 show the depth profiles of three as deposited samples (11, 13, and 21). Note that both interfaces in these samples remained sharp indicating no diffusion during deposition. The samples were then annealed and the depth profiles were checked again (Figs. 4.12 - 4.14). Comparing the figures, it is evident that no long-range hydrogen motion exists in samples 11 and 21 while there is considerable smearing of the interfaces in samples 13.

The IR spectra of the annealed samples also exhibit some interesting features. For samples 27 and 29, both $[H_T]_a$ and N_{da} are reduced upon annealing. However, this change occurs essentially during the initial annealing period and this is demonstrated in Tables VII and VIII. This decrease in the hydrogen content is expected. Hydrogen from the di- and tri-H bonding configurations dissociate upon annealing, forming molecular hydrogen which then either effuses out of the film or remains trapped in isolated microvoids. However, it should be noted that during the initial annealing period both the hydrogen content and the spin density decreases.

Evolution of the stretch frequencies upon annealing is more complex. The stretch peak of sample 21, upon an initial anneal at 310°C for 25 hrs, split into two components at ~ 2073 cm^{-1} and ~ 2000 cm^{-1} (Fig. 4.15). A similar behavior is observed in sample 29 in which the stretch peak split into two parts centered at ~2020 cm^{-1} and ~2075 cm^{-1} (Fig. 4.16). Note that sample 21, unlike sample 29, does not exhibit long-range hydrogen diffusion.

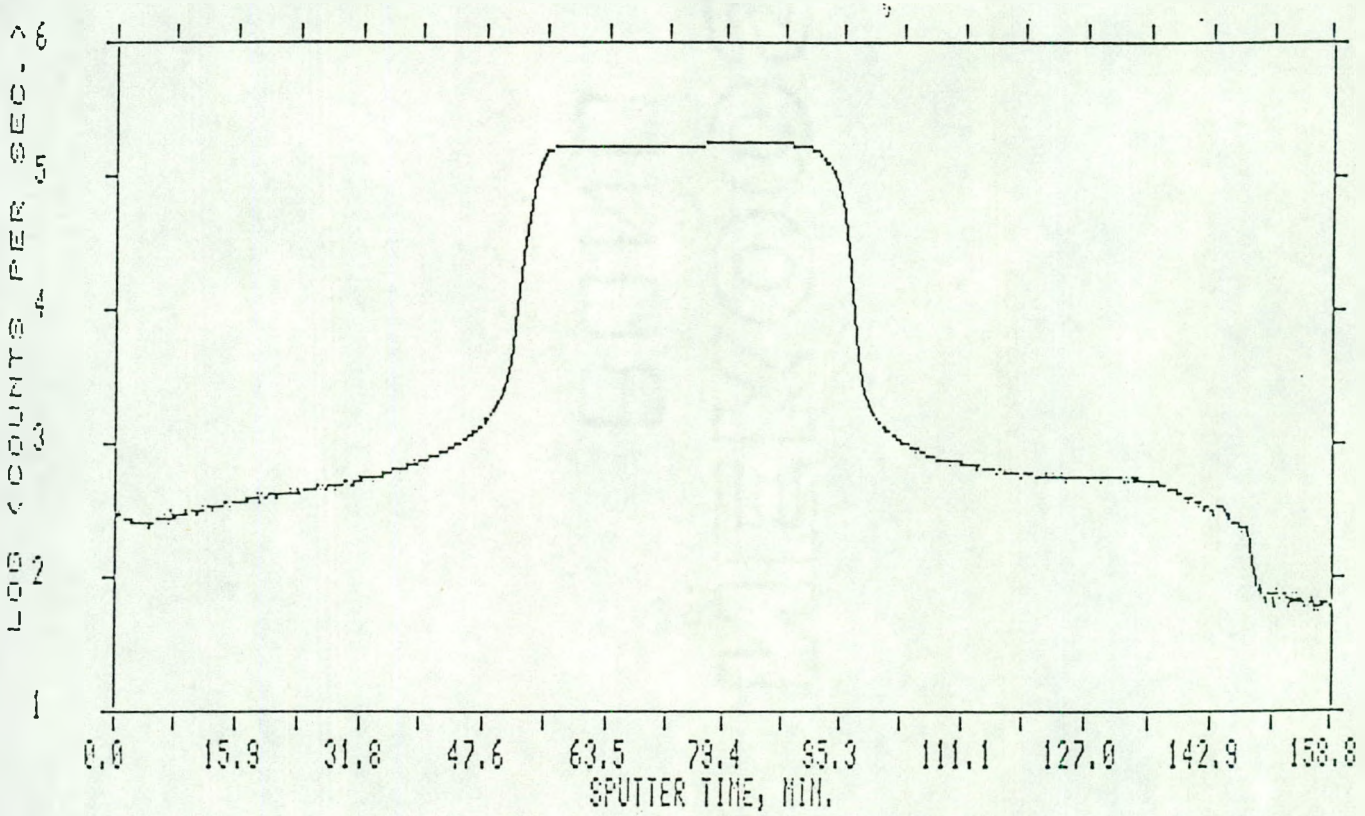

Fig. 4.9. SIMS profile of deuterium in sample 11 (as deposited).

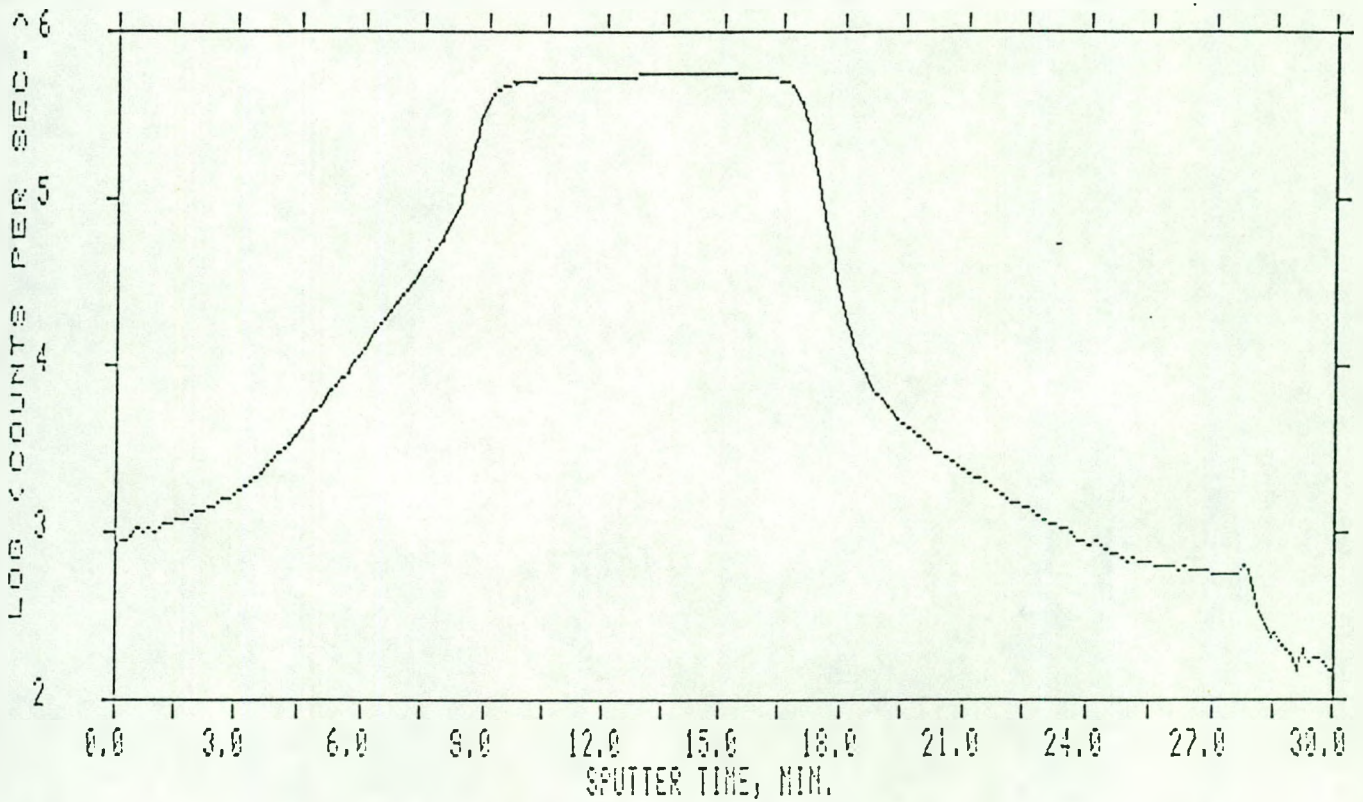

Fig. 4.10 SIMS profile of deuterium in sample 13 (as deposited).

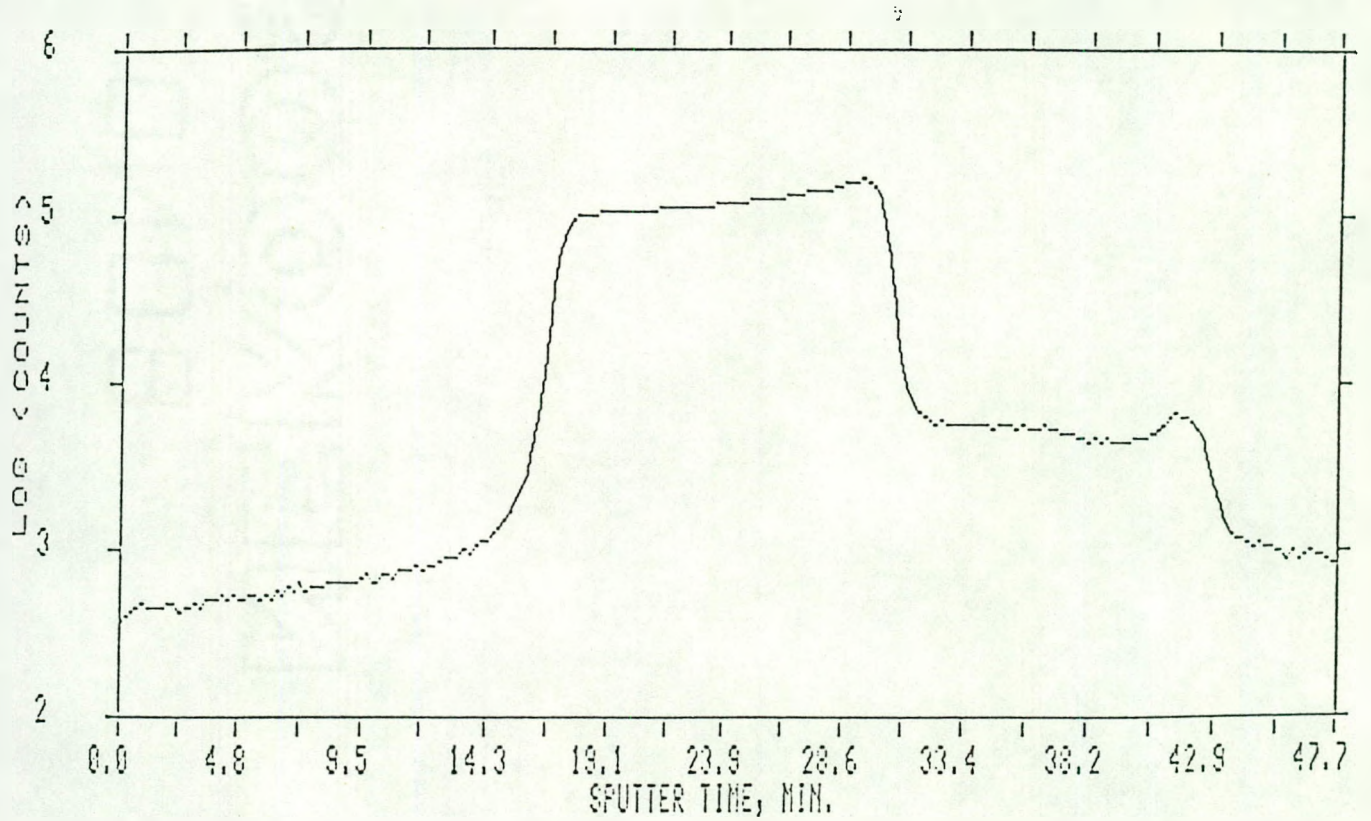

Fig. 4.11 SIMS profile of deuterium in sample 21 (as deposited).

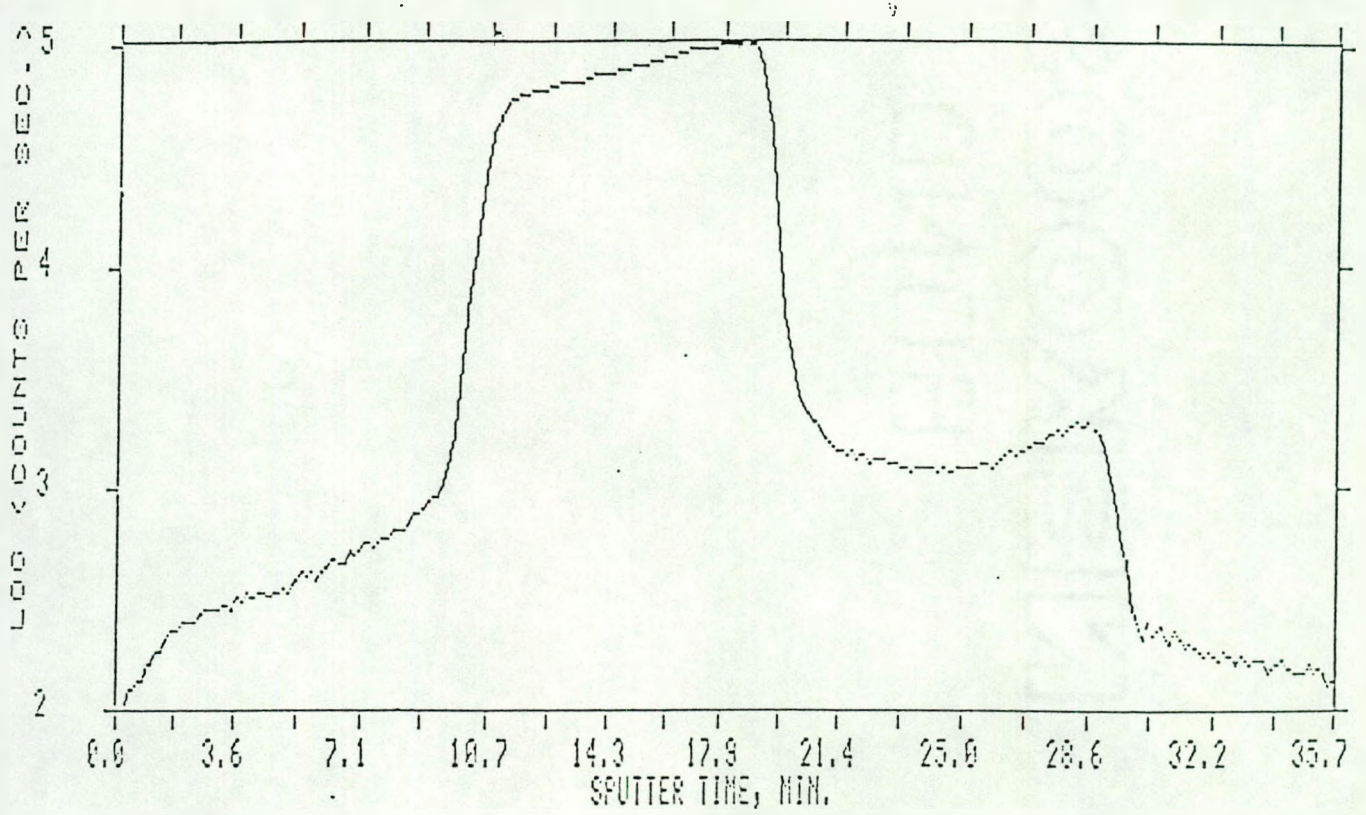

Fig. 4.12 SIMS profile of deuterium in sample 11 annealed at 351°C for 2 days. Note the sharp interfaces.

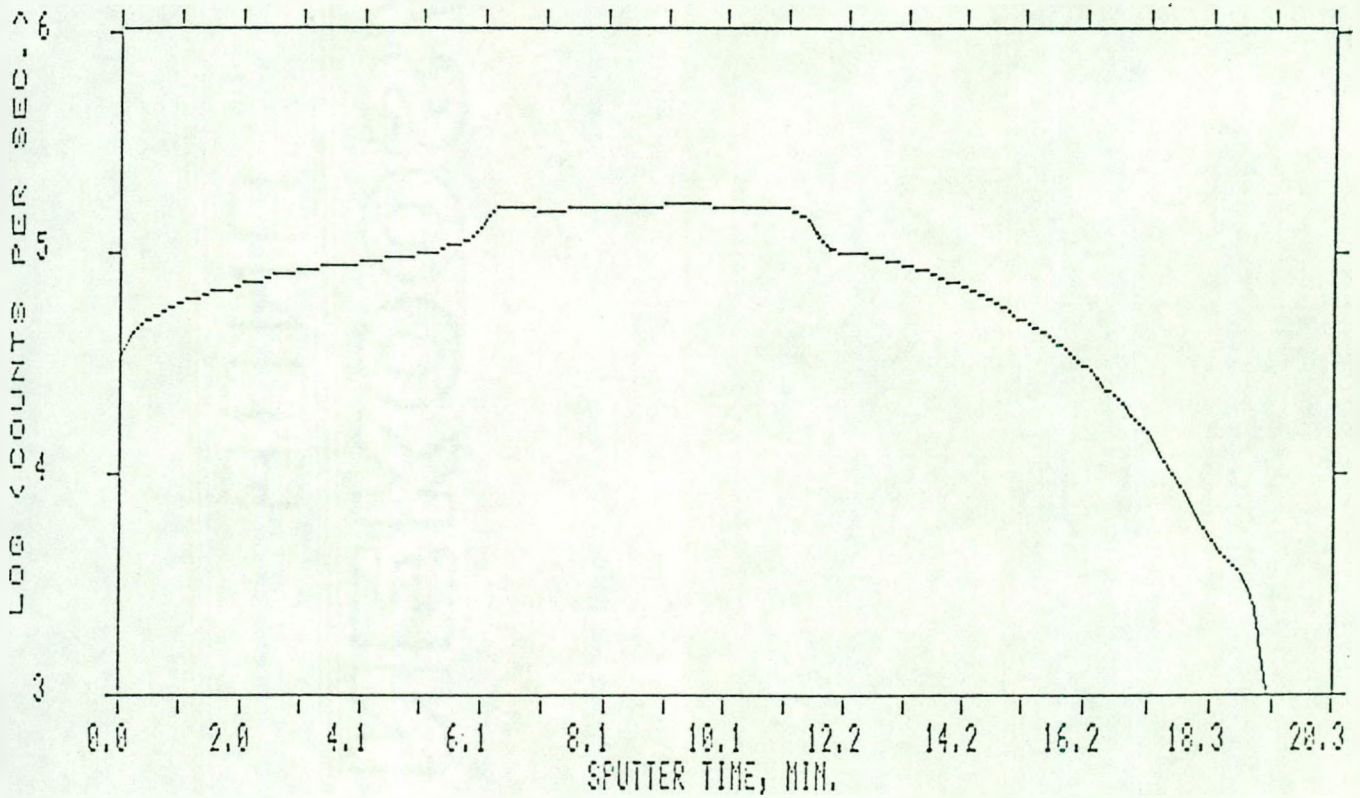

Fig. 4.13 SIMS profile of deuterium in sample 13 annealed at 342°C for 3 days. Note that the interfaces are extensively smeared.

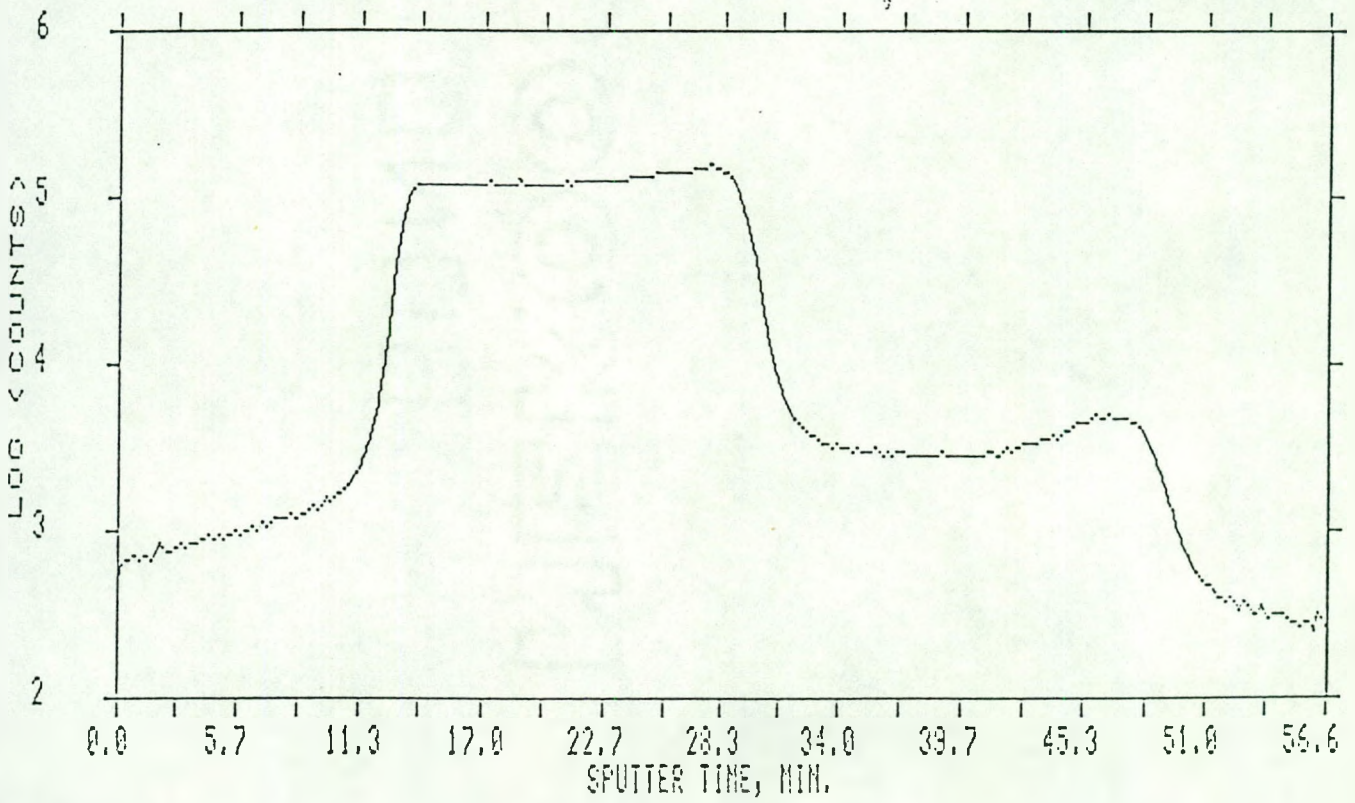

Fig. 4.14 SIMS profile of deuterium in sample 21 annealed at 258°C for 4 days. Note the sharp interfaces.

Table VII. Total hydrogen content $[H_T]_a$, content of di- and tri-H bonded silicon N_{da}, the average value of Θ and the exponent α of sample 27 after annealing

Sample #	Temp. of anneal (^oC)	Time of anneal (hrs)	$[H_T]_a$ (at. %)	N_{da} (at. %)	Θ_{avg} ($\times 10^{11}$) (cm^2)	α
27	as	deposited	17	4	-	-
B	355	1.00	12.0	4.2	4.3	0.90
A		2.00	11.5	3.7	5.1	
D		4.00	11.6	2.8	4.6	
C		8.08	11.6	3.4	4.4	
E		21.35	10.5	3.1	6.7	
G	310	6.00	11.5	4.0	2.4	0.65
F		11.00	11.7	3.8	3.7	
I		42.00	11.7	3.3	4.8	
J		90.00	11.3	3.1	6.8	
M	275	71.11	12.2	3.4	4.6	0.89
K		109.23	11.0	3.7	4.3	
N		191.95	11.1	3.4	5.6	
P		221.73	11.3	3.6	5.3	
L		501.32	10.7	3.4	6.7	

Table VIII. Total hydrogen content $[H_T]_a$, content of di- and tri-H bonded silicon N_{da}, the average value of Θ and the exponent α of sample 29 after annealing

Sample #	Temp. of anneal (^oC)	Time of anneal (hrs)	$[H_T]_a$ (at. %)	N_{da} (at. %)	Θ_{avg} ($x10^{11}$) (cm^2)	α
29	as	deposited	19	5	-	-
A	350	2.00	13.4	2.8	3.0	0.78
C		4.00	13.2	3.1	4.6	
B		8.00	13.8	2.8	5.2	
D		24.00	11.7	2.3	5.4	
I	305	6.1	11.5	3.6	2.1	0.89
J		14.9	11.7	3.2	1.5	
H		48.0	12.0	2.5	1.9	
F		72.0	13.8	2.7	2.3	
G		96.0	13.0	2.4	2.8	
N	275	70.12	15.4	3.2	1.8	0.91
R		118.45	11.0	2.7	2.7	
M		186.73	13.0	2.3	1.6	
K		261.47	13.2	3.7	2.0	
O		500.45	12.3	2.7	2.5	

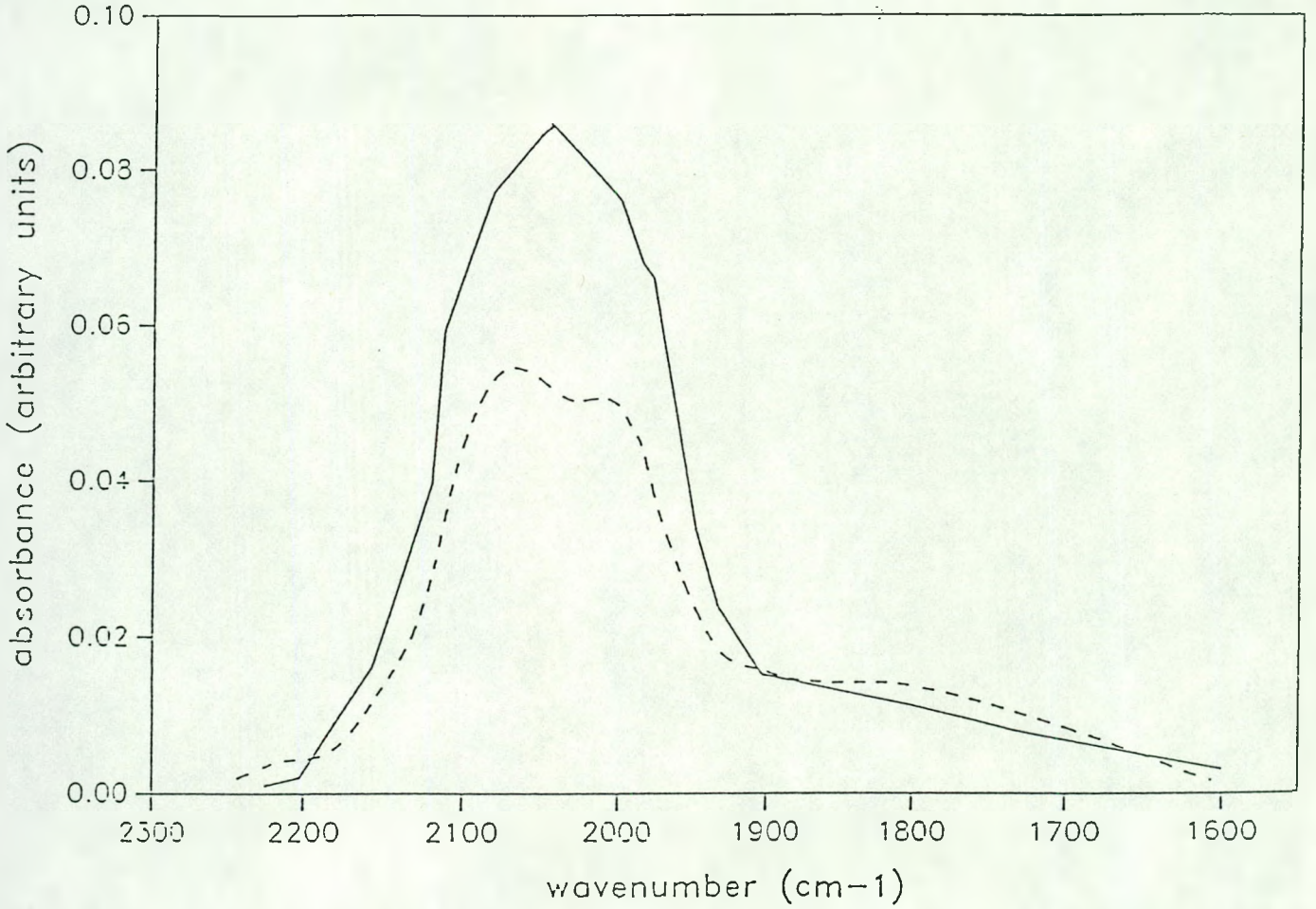

Fig. 4.15 The IR stretch peak of sample 21; as deposited (solid curve) and after an anneal at 310°C for 25 hrs (dashed curve).

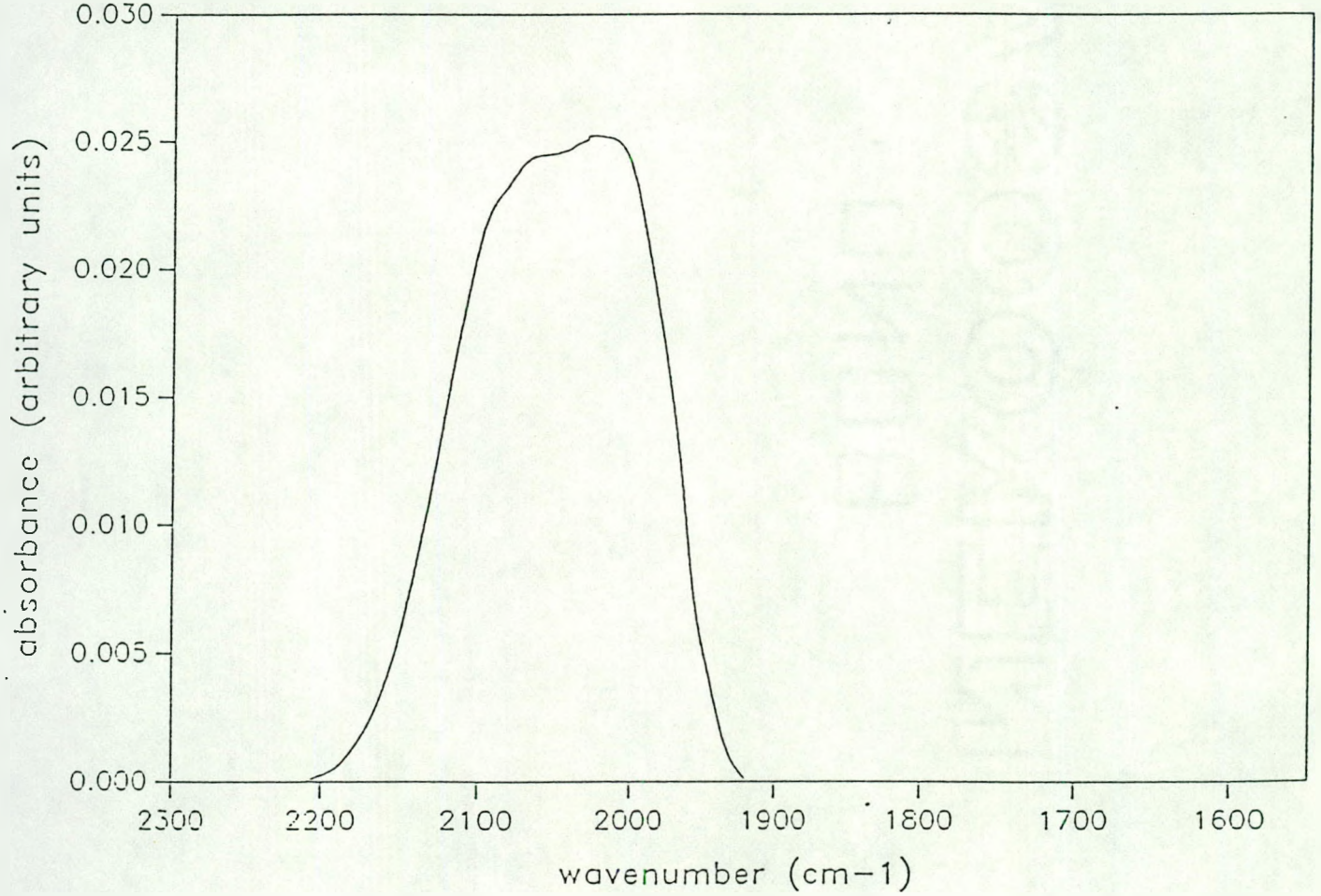

Fig. 4.16 The IR stretch peak of sample 29; as deposited (solid curve) and after an anneal at 350°C for 1 hr (dashed curve).

It is generally believed that N_{do} is directly related to the microvoid content of the film.[42] From Table VI, it is apparent that a clear correlation exists between N_{do} and H diffusion. When the content of microvoids exceeds a critical value, corresponding to an initial value of di- and tri-H configuration of 7 ± 1%, the long-range motion of atomic hydrogen is critically suppressed. This phenomenon is seen although a significant fraction of hydrogen in the film remains in a bulk mono-H configuration, i.e, not on an internal surface. This clearly is the case for sample 21 which, after annealing, shows a stretch peak component at ~ 2000 cm^{-1} (Fig. 4.15). A striking observation is that either there was significant smearing of the interfaces or none at all.

Tables VII and VIII also list the average value of Θ, Θ_{avg} at three temperatures for various anneal times and the corresponding value of the exponent α. (Note that Θ_{avg} is the average value of Θ for the top and bottom interfaces). The $\log(\Theta_{avg})$ vs. $\log(t)$ plots of samples 27 and 29 are shown in Figs. 4.17 and 4.18 respectively. It is clear from these figures that $\Theta \propto t^{1-\alpha}$ and hence $D \propto t^{-\alpha}$, where $\alpha = 0.75 \pm 0.1$. The results show that diffusion decreases strongly with time and is weakly temperature dependent at constant annealing times. The high value of α for these high H content, microvoid-rich samples suggests that within the multiple trapping model (Eq. 1.4), the characteristic energy T_o of the exponentially distributed trapping sites is anomalously high (~2300K). From Eq. (1.7) the activation energy E_{diff} for $L \simeq 700Å$ is estimated to be ~1.3 eV. This is in good agreement with the accepted value of ~1.4 - 1.5 eV. However, D_o then is ~2 x 10^{-5} cm^2s^{-1}, three

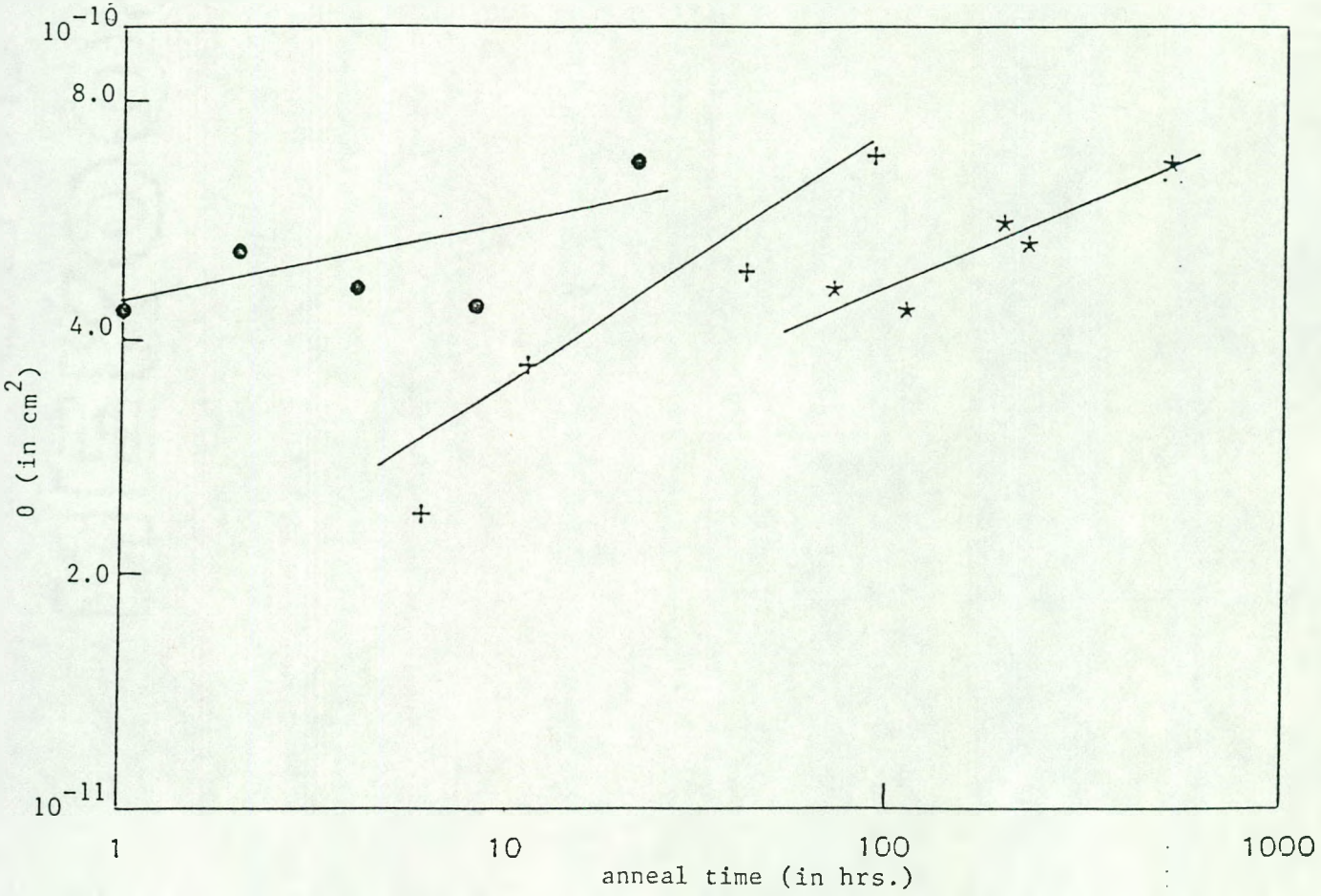

Fig. 4.17 θ(t) versus t for sample 27 at 355°C (•), 310°C (+) and 275°C (*). The values of α are 0.9, 0.65, and 0.79 respectively

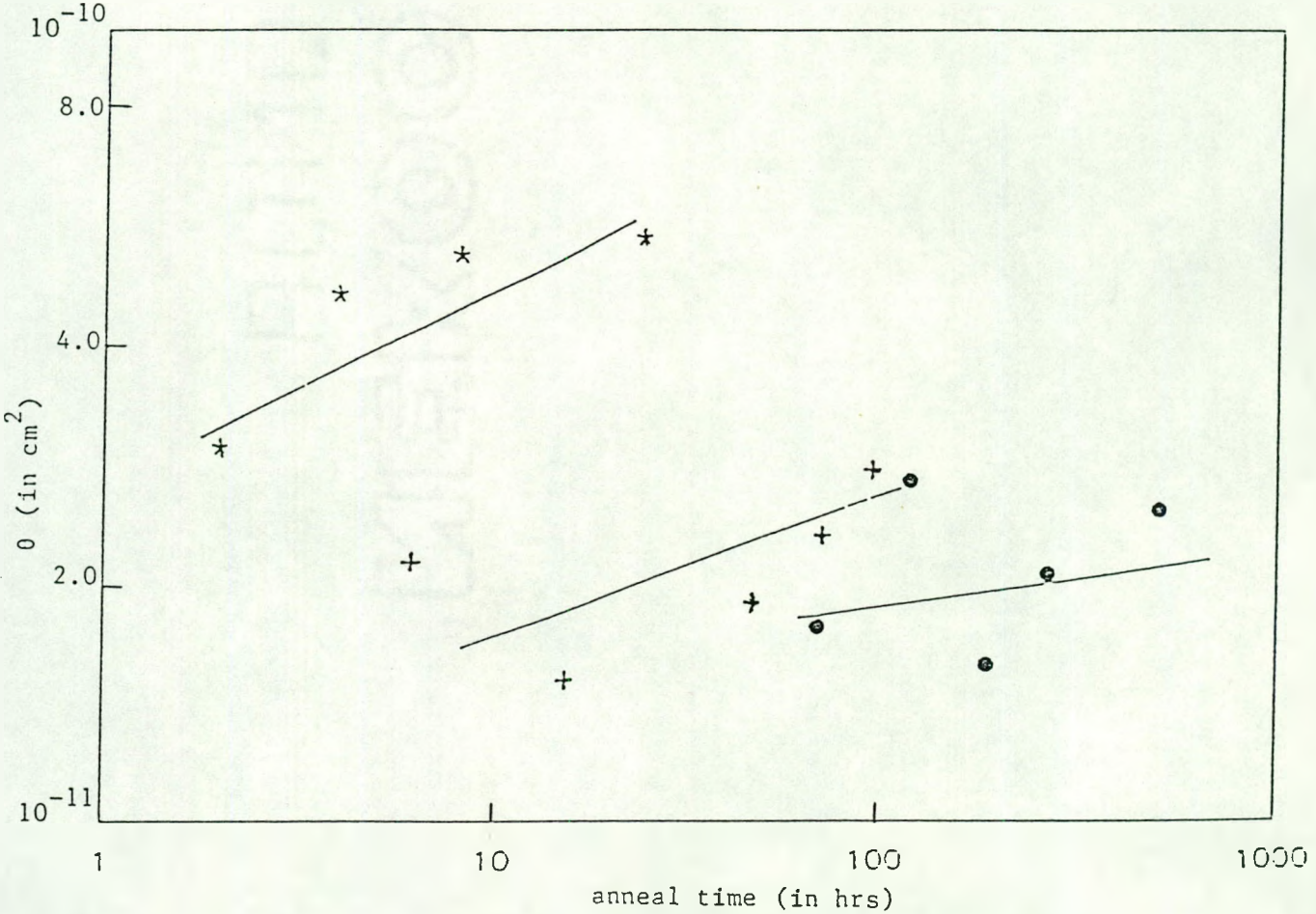

Fig. 4.18 θ(t) versus t for sample 29 at 355°C (*), 310° (+) and 275°C. The values of α are 0.78, 0.89, and 0.91 respectively

orders of magnitude lower than boron-doped glow discharge samples.[38,39] This difference may be due to microstructural differences between glow discharge and rf sputter deposited films. The multiple trapping model can account for the suppresion of the diffusion in microvoid rich films if the width of the exponentially distributed trapping sites is even wider and renders $\alpha \simeq 1$ in these cases.

If it is assumed that in Eq (1.3) D_{oo} is thermally activated, and ignoring any temperature dependence of α, the apparent activation energy is estimated to be $\sim 0.55 \pm 0.2$ eV. Although this value is considerably smaller than the accepted values, it is in close (perhaps fortuitous) agreement with the floating- (dangling-) bond formation energies of 0.3 (0.6)eV.[11]

The results described above can also be explained within the framework of the floating bond model proposed by Pantelides.[10,12] In this picture, the diffusion is mediated by the migration of defects in the bulk (Eqs. 1.14 - 1.17). As the samples are annealed the density of both floating and dangling bonds decreases. Also, as the network relaxes to its quasiequilibrium state, the defects occupy deeper sites in the broad distribution of their formation (equivalent to their migration activation) energy. Consequently, both the generation rate and the mobility decreases.[42] This, then, could account for the power law time dependence of the diffusion constant.

Our results indicate that long-range hydrogen motion is quenched in samples with high microvoid density (corresponding to $N_{do} > \sim 7\%$). This observation is in qualitative agreement with recent calculations of Biswas and coworkers[81]. They have shown that microvoids in a-Si quench

the floating bonds and trap the dangling ones at their surfaces. Thus the density of microvoids, through its effect on annihilation of defects and/or structural relaxations, affect the value of α. This, then, also explains the low value of α ($\sim$ 0.25) for device quality material.[38,39] If microvoids are dominant in determining the value of α, and its density is essentially independent of temperature,[38,82] the weak temperature dependence of α can now be understood.

Hydrogen poor samples The IR spectra of these annealed samples show important differences when compared with that of their hydrogen rich counterparts. This set of samples show no changes in its IR spectra upon annealing.[2] The values of $\Theta(t)$ for samples 81, 84, and 33 are plotted in Figs. 4.19 - 4.21, respectively. The value of Θ in undoped gd deposited a-Si:H, as measured by CM,[78] are also shown for comparison.

It is clear from Fig 4.21 that diffusion in sample 33 is somewhat slower than that measured by CM. For sample 81, however, diffusion at 350°C is $\sim$ 20 times slower than samples 27 and 29. At 300°C, no diffusion was observable and hence the measurements on this sample was restricted to a narrow temperature range of 330 - 400°C. Fig. 4.20 explicitly shows the values of Θ for the top (Θ_L) and the bottom (Θ_R) layers in sample 84. Θ_L is generally greater than Θ_R by almost the same factor. This behavior is seen in most samples (undoped and boron-doped) and its origin is not clearly understood.

---

[2]Only sample 33 lost some hydrogen when annealed at 360°C for 8 hrs.

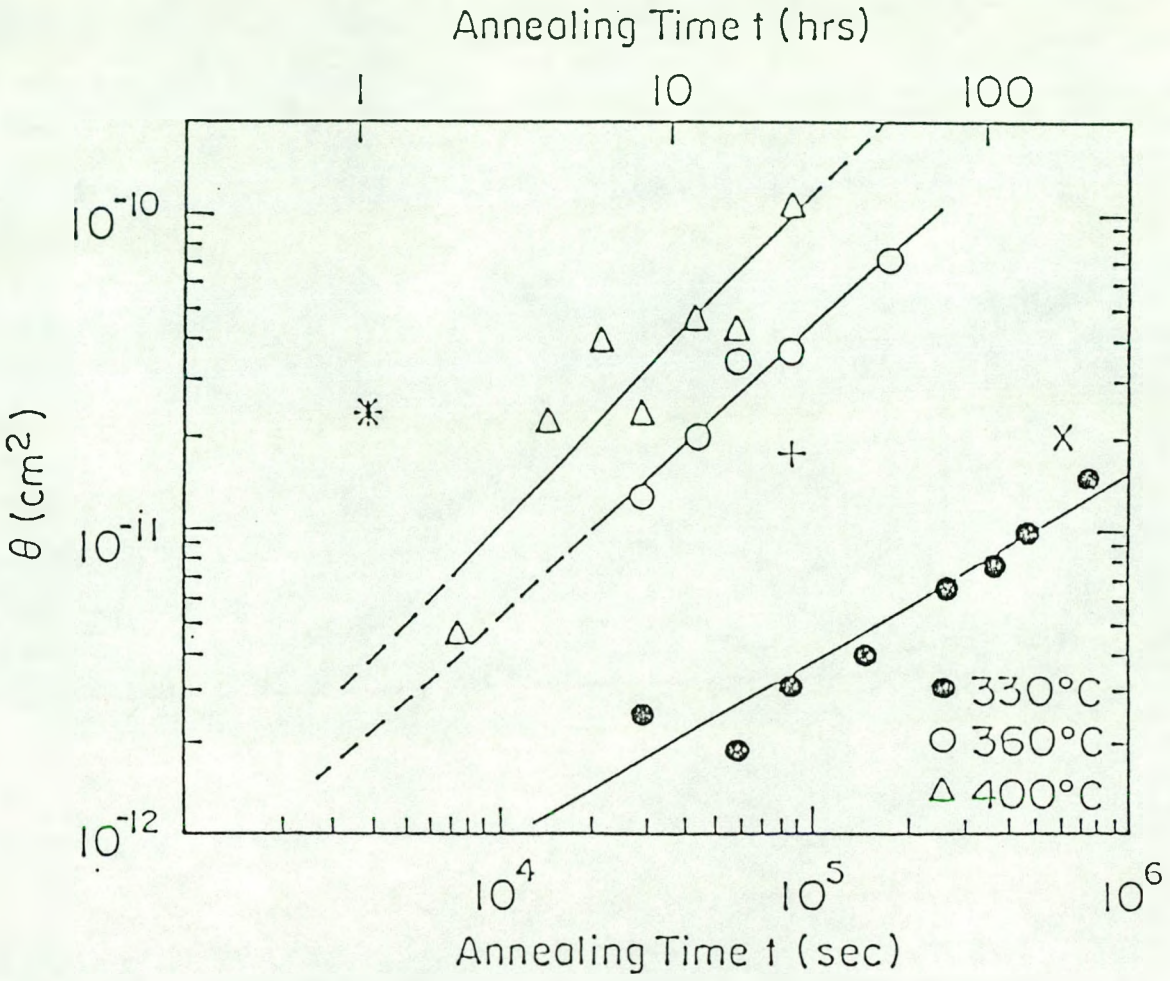

Fig. 4.19 θ(t) versus t for sample 81. The values at 346°C have omitted to avoid clutter. The values of θ(t) as measured by Carlson and Magee (ref. 76) at 250°C (x), 300°C (+), and 350°C, are shown for comparison.

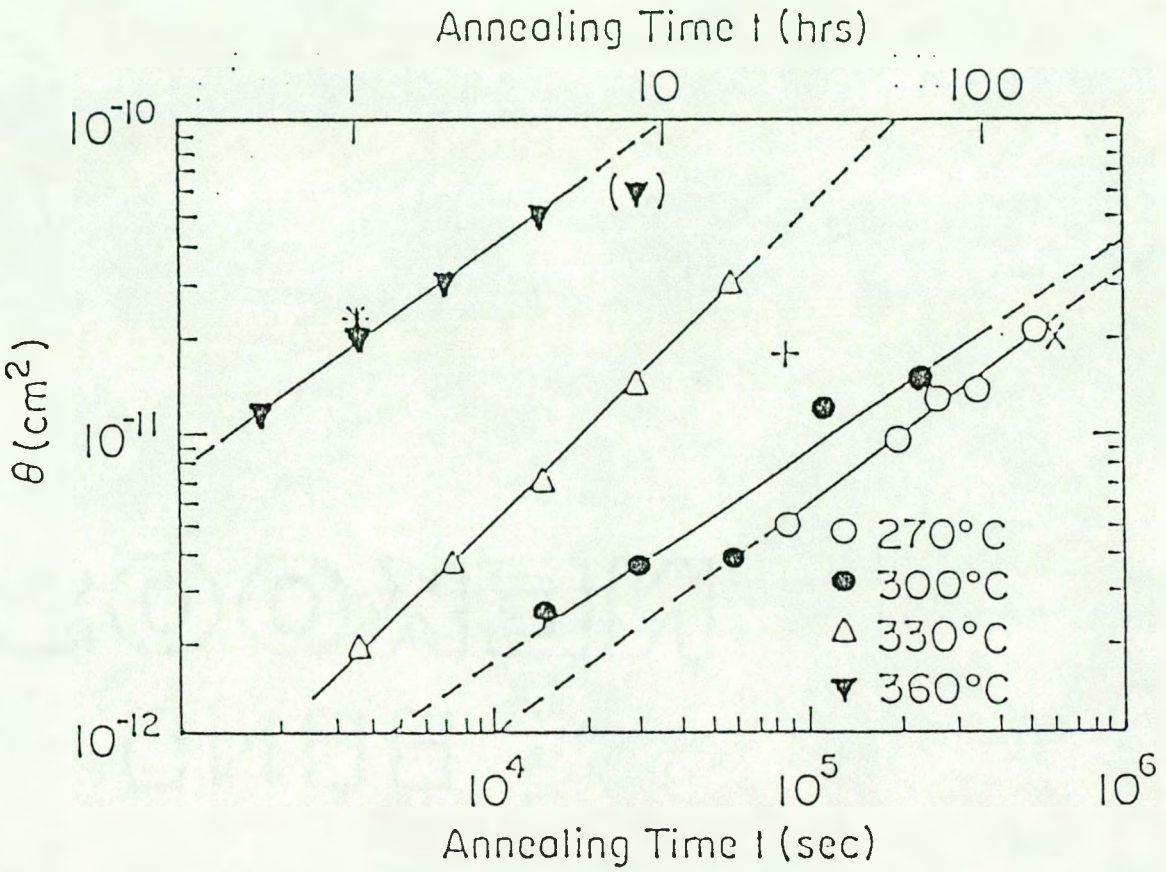

Fig. 4.20 θ(t) versus t for sample 33. The value of θ(t) following annealing for 8 hrs at 360°C is given in parenthesis, some hydrogen evovlved out of the film during that annealing.

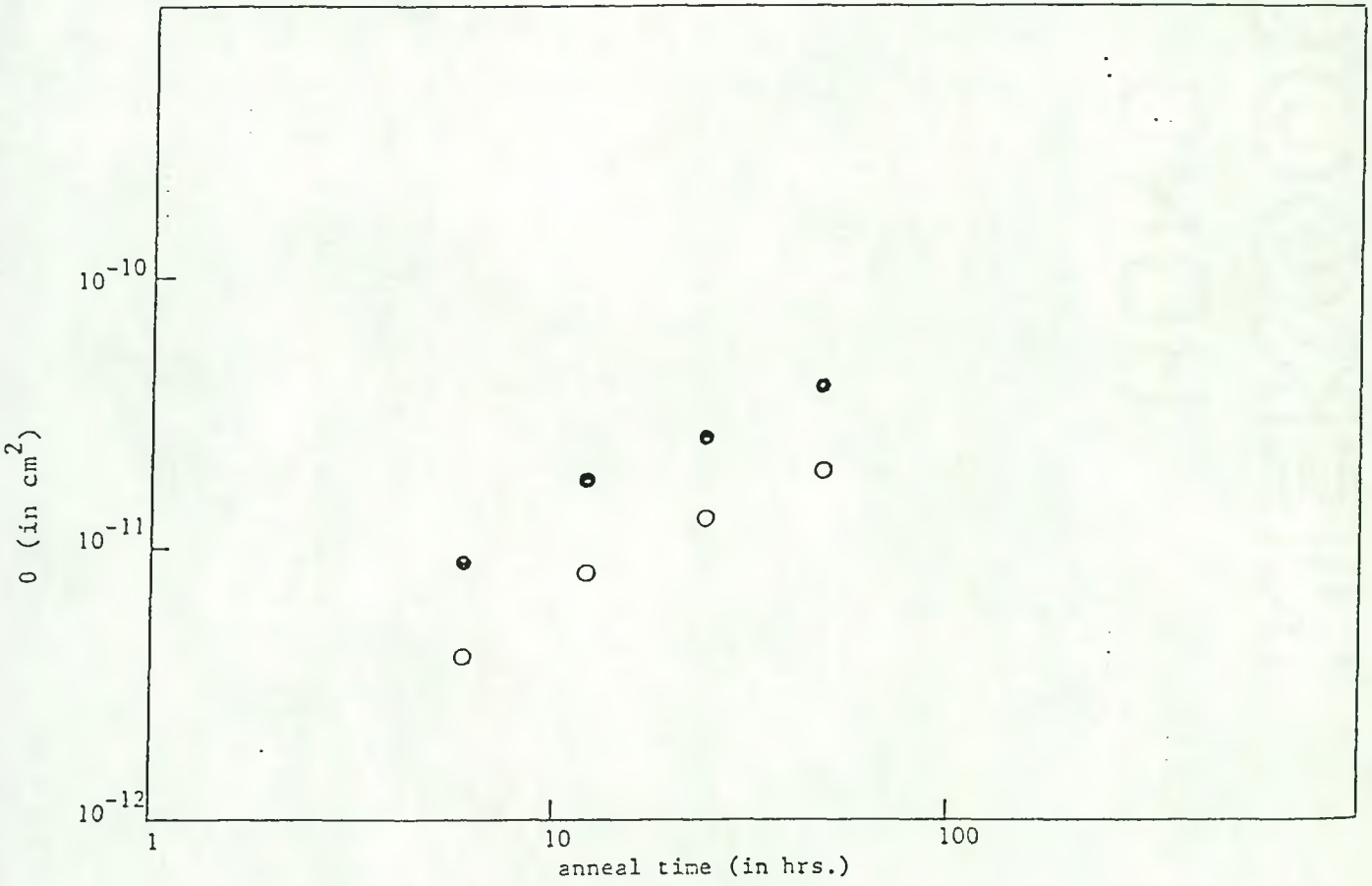

Fig. 4.21 $\theta(t)$ versus t for sample 84 annealed at 363°C. Note that θ in the left layer is always greater than that of the right layer. The average value of the exponent $\alpha \sim 0.28$

The values of α, T_o and Θ_o at various temperatures is shown in Table IX. It is clear that α generally decreases with increasing temperature, except for sample 33 at 360°C. This departure is beyond experimental error and is real. An important difference in the value of α in these samples is its relatively small value. Compare, for example, the values of α measured at ~ 355°C for samples 81, 84, and 33 with that of samples 27 and 29. Since Albers[18] has demonstrated that $N_{do} \propto ([H_T]_o)^{1/2}$, we have plotted α vs $[H_T]_o^{1/2}$. Fig. 4.22 shows that an increase in the microvoid density in the samples leads to an increase in the quenching of the long range H motion. Extending the line to $\alpha = 1$ (when diffusion is totally qunched) gives the critical value of N_{do}. This value is found to be ~ 5.5 ± 1.0 at. %.

The anomalous behavior of α in sample 33 is, however, not surprising. Recently, X. M. Tang et al.[84] have shown than in undoped gd depsited a-Si:H, α increases with increasing T above 350°C, and strongly so between 380° and 470°C. This behavior is suspected to be due to thermal generation of defects and/or structural relaxation. The departure of α from $1 - T/T_o$ (Eq. 1.4) is thus thought to arise from the above processes. However, it should be noted that even in the abscence of the above processes, deviations from Eq. (1.4) are expected to occur if the distribution of the trapping sites is nonexponential.[85]

The diffusion parameters for constant diffusion length (L) were also evaluated from the logΘ vs. logt plots. Since it is difficult to predict the behavior of Θ beyond the measured experimental points, only those values of L that did not require extrapolation of data points were

Table IX. The values of α, resulting T_o, at different annealing temperatures T, the activation energy E_{diff} calculated for various diffusion lengths L

Sample	T(^{o}C)	$\alpha(\pm 0.1)$	T_o(K)	L(Å)	E_{diff}(eV)
81	330	0.39	990	350	1.94
	346	0.34	940	500	2.18
	360	0.07	680	700	2.44
	400	~0.0	670		
33	270	0.22	700	630	1.65
	300	0.32	840	1400	1.67
	330	~0.0	600		
	360	0.3	900		
84	360	0.28	880	-	-

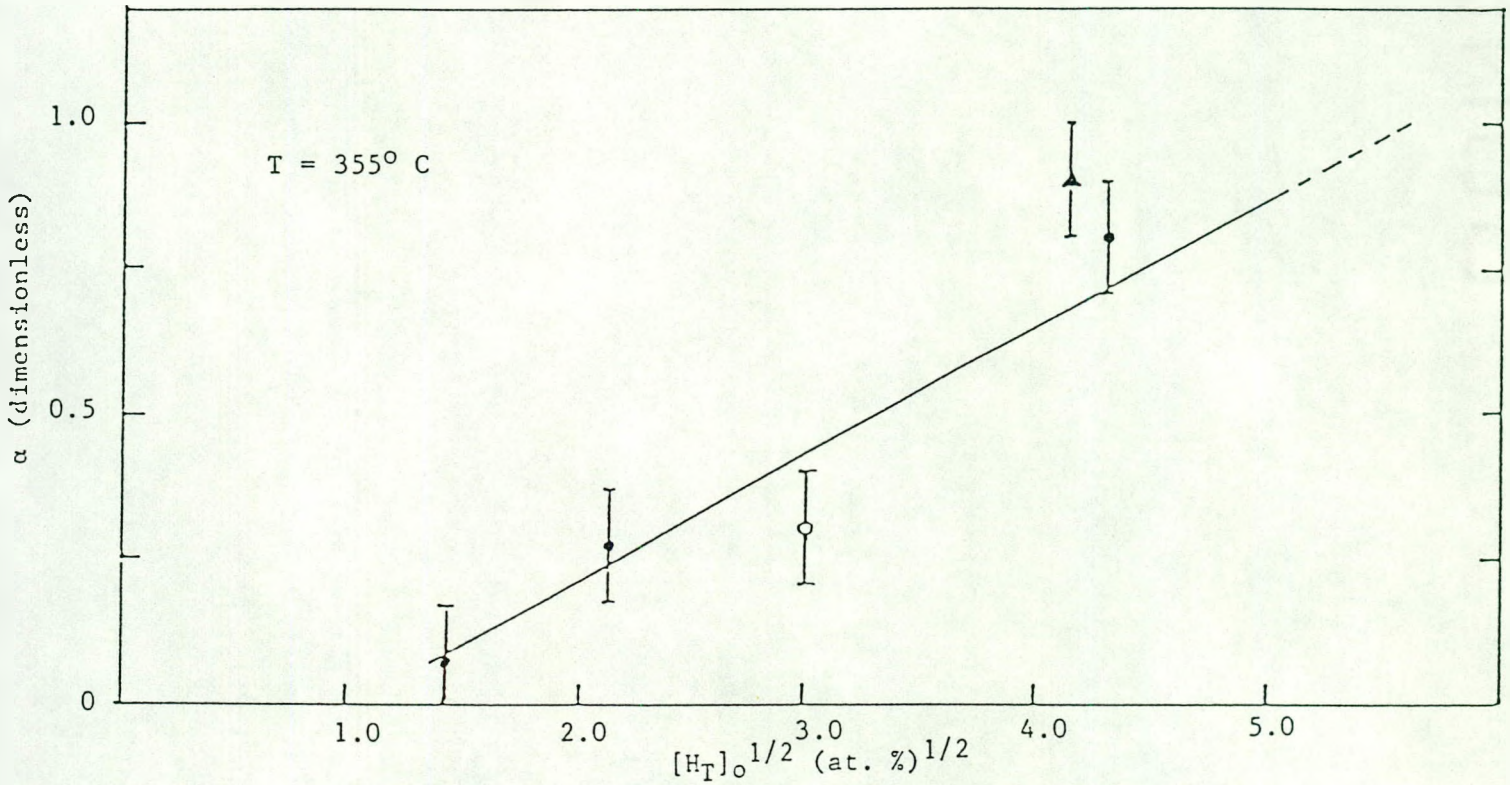

Fig. 4.22 α versus $[H_T]_o^{1/2}$ for samples annealed at ~ 355°C. Solid circles and triangle represent rf sputtered samples deposited at target to substrate separation of 1" and 2", respectively. Open circle represents the glow discharge deposited sample

used. The corresponding values of the activation energy E_{diff} were calculated from

$$E_{diff} = \frac{kT}{(1 - \alpha)} \ln[\frac{L^2(1 - \alpha)}{4D_{oo}}] \qquad 4.8$$

The values of E_{diff} and D_o corresponding to various diffusion lengths in samples 81 and 33 are shown in Table IX. (The activation energy of the hydrogen rich samples were also calculated and was found to be ~ 1.3 eV for L ≃ 700Å). As expected, E_{diff} increases with increasing L indicating that the hydrogen samples deeper and deeper sites as it diffuses. However, at constant L, the activation energy decreases as the total hydrogen content of the samples increases. This is demonstrated for L ≃ 700Å in Fig. 4.23a. This would imply that the diffusion length (and hence Θ) increases with increasing $[H_T]_o$ when both the temperature and time of anneal is kept constant. This dependence of Θ on the total hydrogen content is shown in Fig. 4.23b. The tendency of Θ to flatten out at high $[H_T]_o$ at ~ 330°C is possibly due to the evolution of hydrogen from the films at this temperature. Note this behavior is not observed at ~ 300°C. This is consistent with the well known fact that in undoped a-Si:H, $Si-H_2$ and $Si-H_3$ bonding configurations dissociate below 300°C.

The slow diffusion in low $[H_T]_o$ films is probably not due to hydrogen bonded to internal microvoid surfaces. The IR spectra in all these samples indicate that all of the hydrogen remain in bulk-like mono Si-H configurations (stretch peak at 2000 cm^{-1}) both before and after

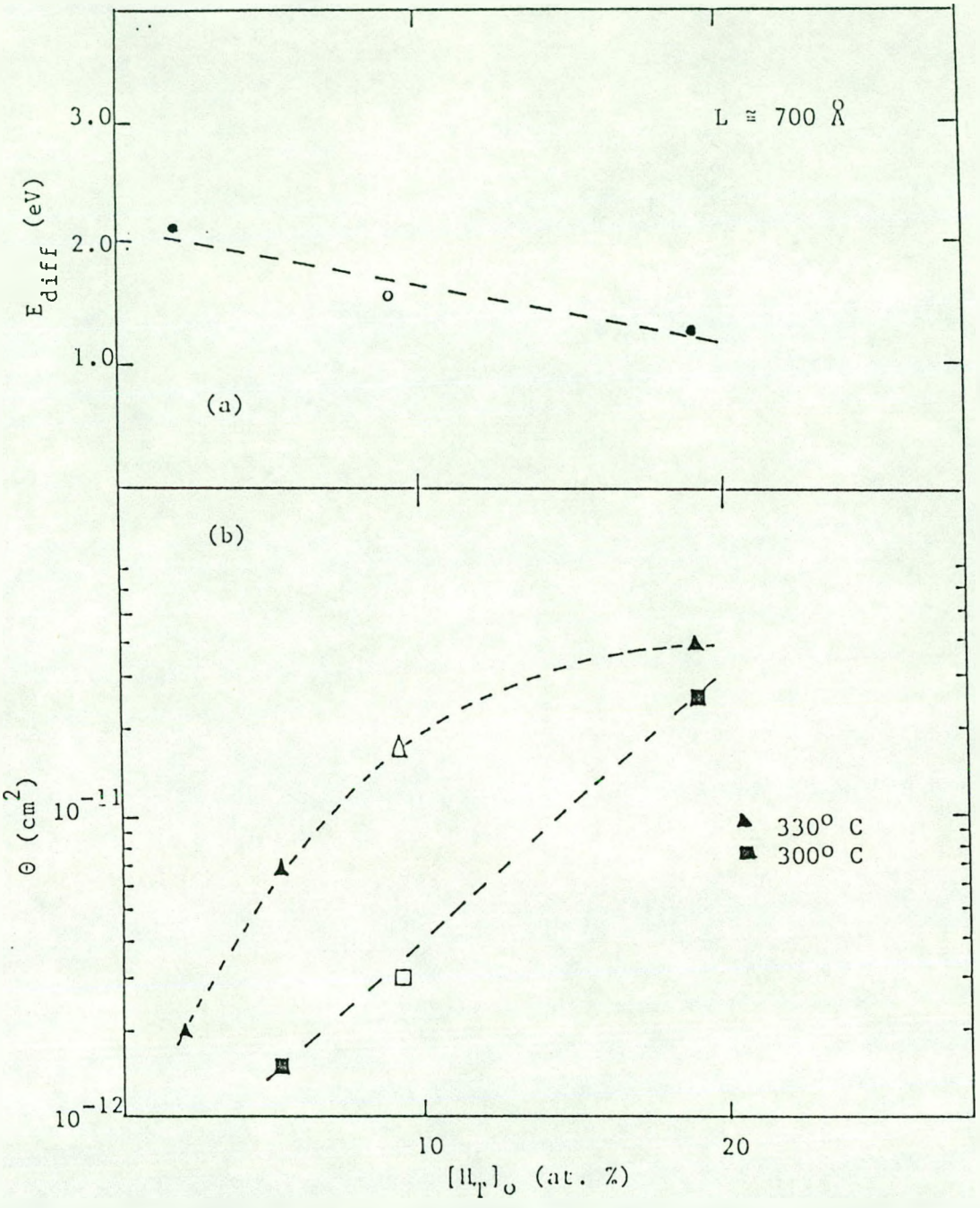

Fig. 4.23 Effect of hydrogen microstructure on the diffusion parameters. The dependence of (a) activation energy and (b) Θ(t) at a constant anneal time of 10 hrs on the total hydrogen content. The solid and open symbols represent rf and glow discharge deposited samples respectively

the anneal. The slowing of diffusion with decreasing $[H_T]_o$, a significantly higher E_{diff}, and its L dependence suggest that as $[H_T]_o$ decreases, the hydrogen in the film occupy the relatively few deeper sites. These sites are thought to be occupied preferentially during deposition, probably through equilibration processes that take place during deposition. In hydrogen rich samples, diffusion is then dominated by hydrogen occupying relatively shallower trapping sites and hence is faster. However, some or most of this hydrogen eventually becomes trapped in microvoids or microvoid-induced trapping sites and is rendered relatively immobile. Thus the value of α also increases with increasing $[H_T]_o$ until it reaches unity when long range hydrogen motion is totally quenched.

The nature of the microvoid related traps is not completely understood. It is evident from this work that as the microvoid density increases, the long range hydrogen motion is increasingly suppressed, and when the microvoid content exceeds a critical value of $\sim 6.5 \pm 1.0\%$, the diffusion is totally quenched. This occurs even though a large fraction of the hydrogen remains bonded in a mono Si-H configuration as evidenced from the prominent shoulder of the stretch peak at ~2000 cm^{-1}. Recently, small angle x-ray scattering and IR studies on device quality a-Si:H by Mahan et al.[62] suggested that many of the microvoids are small, anisotropic (e.g, disk-like) and largely unhydrogenated multivacancies containing no more than 4 - 9 hydrogen atoms. Since these multivacancies are highly compressed with opposite surfaces ~ 3Å apart, the dielectric screening experienced in these microvoids is similar to that in the bulk. Consequently, the stretch peak of hydrogen

bonded in these sites will vibrate at ~ 2000 cm^{-1}, similar to isolated mono Si-H embedded in the bulk.

Although IR cannot distinguish between the mono Si-H bond embedded in the bulk and clustered hydrogen in the multivacancies, proton NMR measurements on these samples can. Clustered hydrogen in these microvoids contributes to the broad proton NMR component while the isolated bulk Si-H contributes to the narrow line. Preliminary NMR measurements were made by Zheng and coworkers[86] on rf sputter deposited samples. Three of the four samples (samples 31, 32 and 36) that were studied were deposited at high rf power (550 W) and under conditions in which hydrogen diffusion was observed while sample 33 was deposited under conditions in which hydrogen motion is suppressed. The IR on these samples confirmed that in samples 31, 32 and 36 most of the hydrogen is bonded in the mono Si-H configurations while sample 33 exhibited a significant fraction of di- and tri-H bonding configurations. As expected, the lineshapes of the as-deposited samples were a mixture of both the narrow and the broad components. However, after annealing at 294^{o}C for 24 hrs, the linewidth of the broad component increased while that of the narrow component sharply decreased as shown in Fig. 4.24. These changes are summarized in Table X.[3] It is evident from these results that the content of clustered hydrogen increases upon annealing and further strengthens the hypothesis that the

---

[3]The NMR measurements on these samples were made by Dr. P. C. Taylor and coworkers at the Dept. of Physics, Univ. of Utah, Salt Lake City, UT 84112.

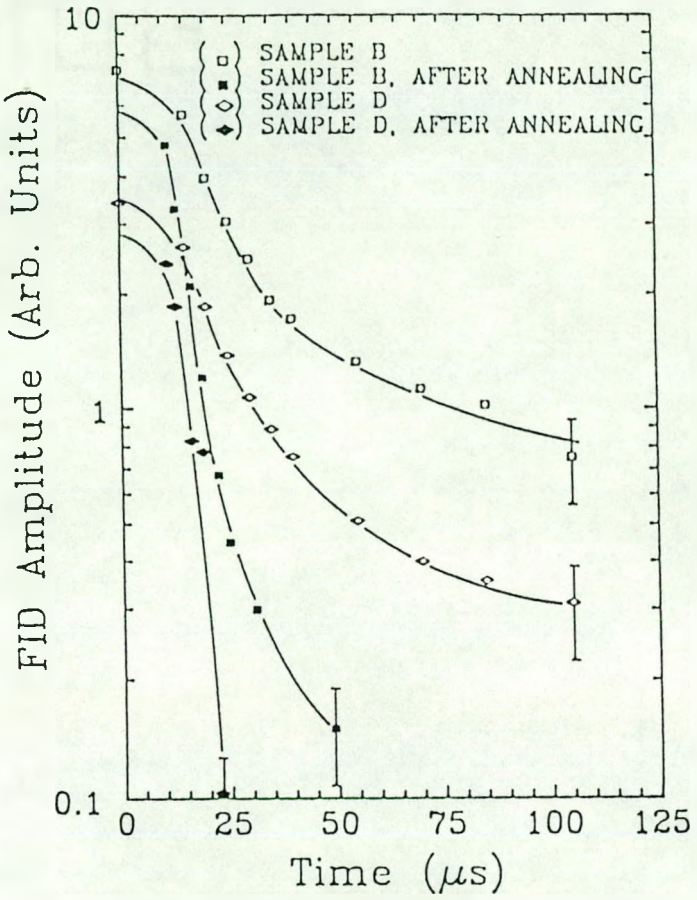

Fig. 4.24 Free induction decays before and after annealing for a samples in which hydrogen diffuses (B) and does not diffuse (D). (From Ref. 84).

Table X. ^{1}NMR lineshape parameters in four undoped a-Si:H samples (from Ref. 84)

	Linewidth (kHz)		
	Broad Gaussian Line	Narrow Gaussian Line	Intensity Ratios (Broad/Narrow)
Sample A	27	6.4	1.6
Sample B	30	9.1	1.6
Sample C	30	6.1	1.5
Sample D	30	7.9	3.0
Sample B after annealing	41	-	> 10
Sample D after annealing	36	-	> 10

microvoid related deep traps are indeed mono Si-H configurations located at the microvoid surfaces.

C. Boron-doped a-Si:H

Boron-doped a-Si:H/a-Si:(H,D)/a-Si:H multilayers ~ 0.5 - 1.5 μm were prepared by rf sputtering in a mixture of 10mT of argon, ~ 1mT of hydrogen, ~ 0.3 mT of deuterium, and diborane (B_2H_6) diluted in argon. The target to substrate separation was ~ 1.25" and the temperature of the unheated substrates was estimated to be ~ 150°C.[82]

The boron content of the films was controlled either by changing the diborane partial pressure or the sputtering power. The doping level of the samples was determined by comparing the boron SIMS count relative to that of the boron implanted Si standards. The samples were annealed at comparatively low temperatures of 180°C and 225°C in evacuated sealed pyrex tubes. The choice of these low anneal temperatures was motivated by two well established results. First, it is well known that the hydrogen evolution rates are shifted to lower temperatures by as much as 150°C depending on the doping level.[65,87] Second, hydrogen diffusion in boron doped samples is greater than the undoped samples by up to three orders of magnitude, generally increasing with the doping level.[38] Consequently, even moderate annealing at low temperatures ($T \geq 180^{o}C$) results in considerable smearing of the interfaces. However, depth profiles of as deposited samples have indicated that the interfaces remained sharp during deposition indicating little or no diffusion at temperatures less than 150°C.

Two samples, one lightly and the other heavily doped, were studied in detail. Sample 40, having a boron content of 0.3 at. %, was prepared at 100W. The sample was ~ 0.5μm thick and had a high hydrogen content with $[H_T]_o$ and N_{do} of 21 and 4 at. %, respectively. Sample 37 was prepared at 550W with $[H_T]_o$ and N_{do} of 9.4 and 1.5 at. % respectively. It was about ~1.2 μm thick and the boron content was 2 at. %.

The $\log_{10}\Theta$ vs $\log_{10}t$ plot for sample 40 is shown in Fig. 4.25. The value of α is estimated to be ~ 0.62 ± 0.1 at 224°C. As expected, the diffusion of hydrogen is faster in this film than in the undoped films and the value of α is consistent with its high microvoid content. Since the thickness of this sample was small, prolonged annealing was performed only on sample 37.

Sample 37 was annealed at 180° and 225°C and the smeared interfaces were then fitted to Eq. (4.4). The agreement with the predicted curve was generally excellent except for the three shortest annealing times. The total hydrogen content and bonding configurations were determined from the 640 cm^{-1} wagging and 840 - 890 cm^{-1} bond bending scissors mode respectively. The IR spectra was monitored after each annealing step and the results are summarized in Tables XI and XII.

Figs. 4.26 and 4.27 show the $\Theta(t)$ vs t plot at 180° and 225°C, respectively, in the top and bottom layers of sample 37. The above results can be divided into three distinct stages. (i) During the first annealing periods up to ~ 50 hrs at 180° and ~ 30 hrs at 225°C, the slope $(1 - \alpha)$ of $\log_{10}\Theta(t)$ vs $\log_{10}t$ is low, indicating a high value of $\alpha = 0.75 \pm 0.1$. These large values are not surprising in view of the considerable $Si-H_2$ and $Si-H_3$ configuration density N_{do} (see Tables XI

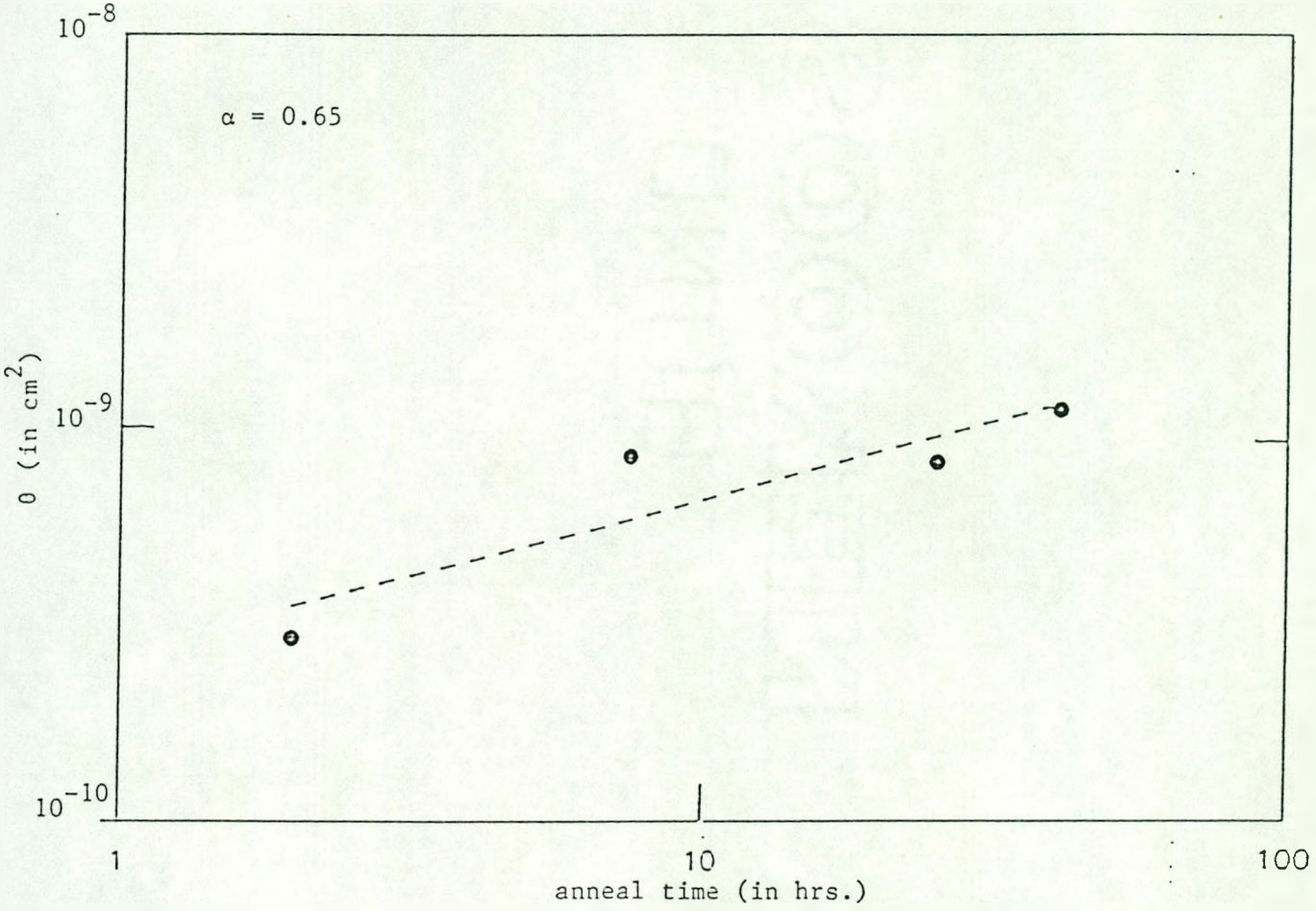

Fig. 4.25 $\theta(t)$ versus t for a boron-doped (0.3 at. %) sample at 225°C

Table XI. Total Si-bonded H concentrations [H_T], SiH_2 and SiH_3 bonding configurations density N_d, and the ratio of I(2100)/I(2000) of the integrated intensity of the 2100 to 2000 cm^{-1} stretch modes, after each annealing step at 180°C for sample 37

Annealing time(hrs)	[H_T] (at. %) (±10%)	N_d (at. %) (±20%)	I(2100)/I(2000) (±30%)
as deposited	9.4	1.7	0.54
6	10.0	1.1	0.62
12	8.0	1.0	0.50
24	8.0	0.9	0.65
48	7.6	0.9	
96	8.5	1.0	0.49
222	8.8	0.7	0.70
516	8.3	0.6	0.57
1080	7.5	0.5	0.62

Table XII. Total Si-bonded H concentrations [H_T], SiH_2 and SiH_3 bonding configuration density N_d, and the ratio I(2100)/I(2000) of the integrated intensity of the 2100 to 2000 cm^{-1} stretch modes, after each annealing step at 225°C for sample 37

Annealing time(hrs)	[H_T] (at. %) (±10%)	N_d (at. %) (±20%)	I(2100)/I(2000) (±30%)
2	8.9	1.4	0.45
4	8.9	1.6	0.57
8	9.9	1.2	0.75
16	8.5	1.3	0.47
32	8.5	1.0	0.47
552	5.7	0.4	0.52
1100	6.9	trace	0.44

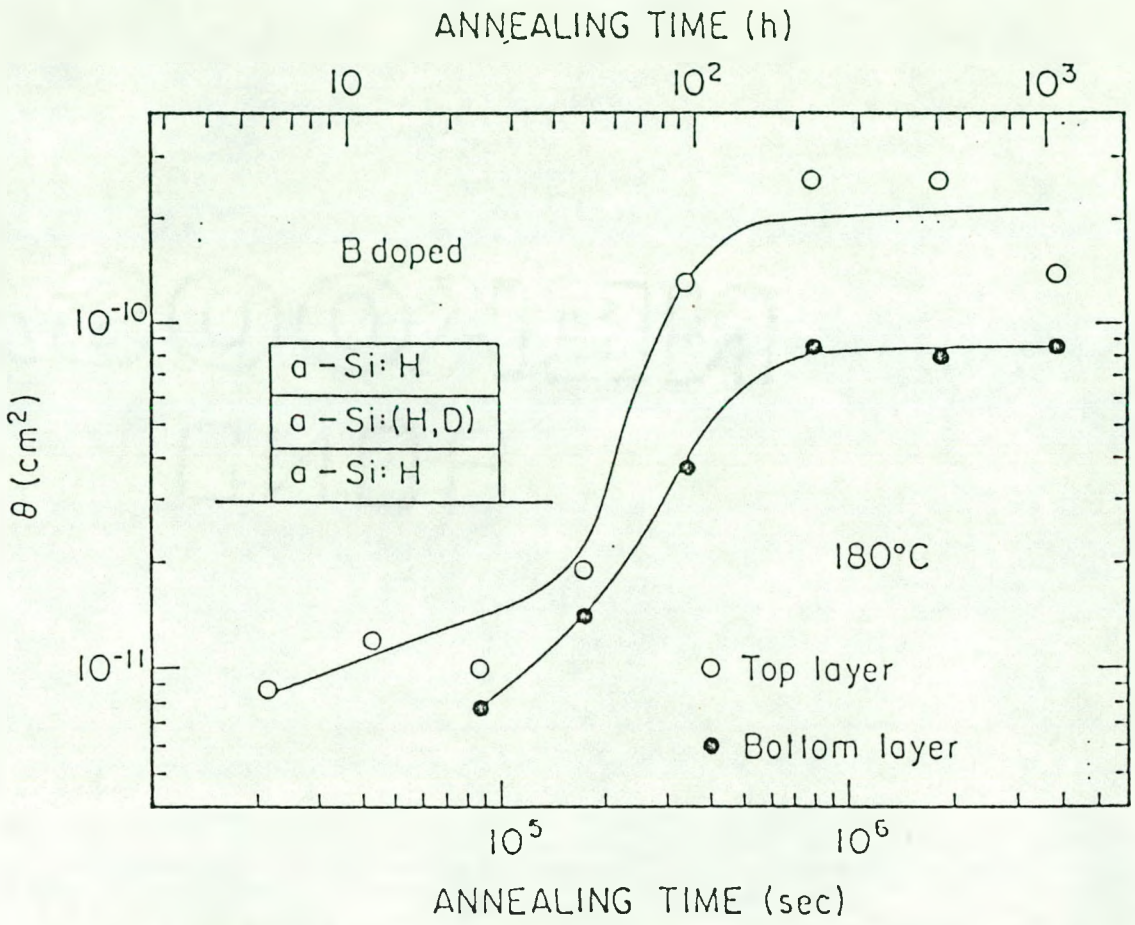

Fig. 4.26 θ(t) versus t for sample 37 (2 at. %) boron-doped at 180°C

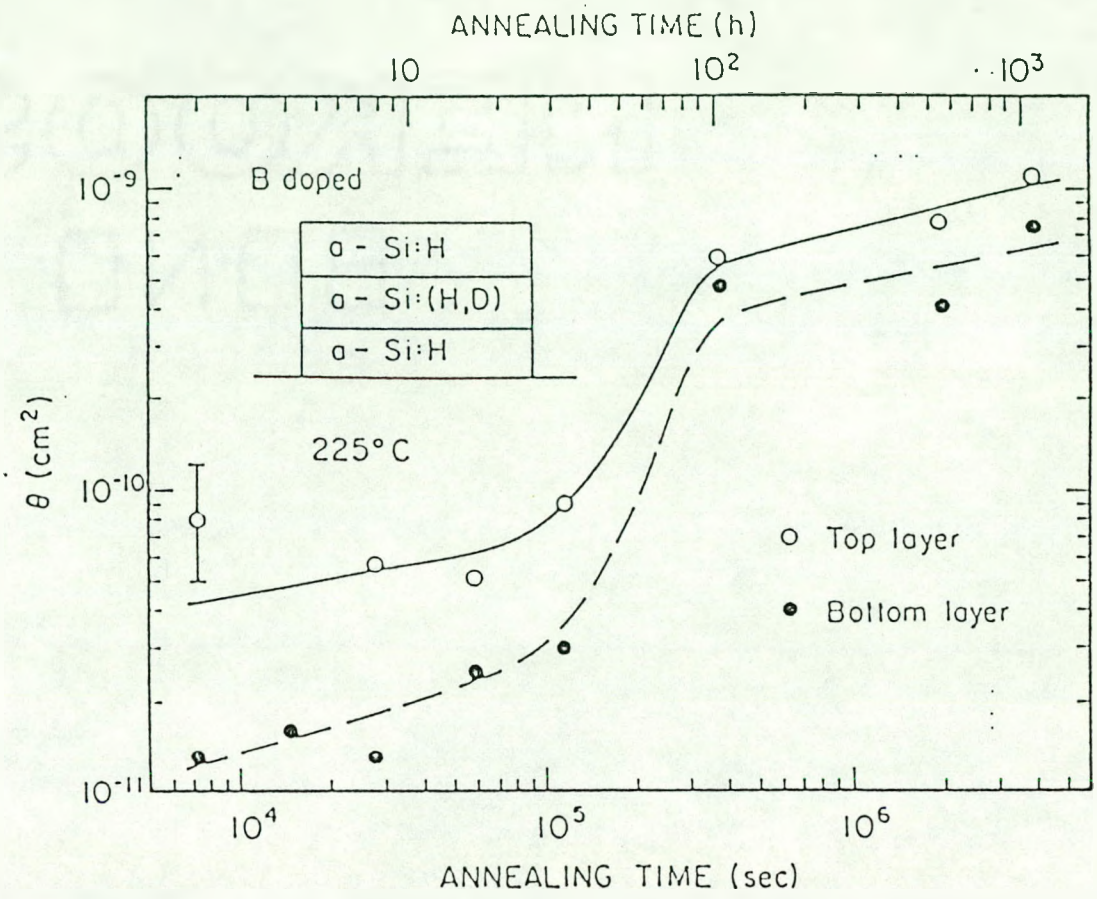

Fig. 4.27 θ(t) versus t for sample 37 (2 at. %) boron-doped at 225°C

and XII), indicating a significant microvoid content. (ii) The second stage is characterized by a sharp rise of $\Theta(t)$ with time, i.e., a sharply decreasing α. (iii) Following prolonged annealing, the diffusion of hydrogen drastically slows down beyond ~ 100 hrs at 225° (α ~ 0.8) and is essentially quenched beyond ~ 200 hrs at 180°C (α ~ 1). As has been mentioned earlier in the chapter, the values of $\Theta(t)$ in the top layer are consistently higher than those in the bottom layer. This observation is not understood at this time.

The average value of $[H_T]$ and N_d in the as deposited samples were found to be 9.4 ± 1.0% and 1.7 ± 0.3%, respectively, indicating significant microvoid content. $[H_T]$ decreased slightly during the initial annealing step of 2 hrs at 225°C and 6 hrs at 180°C. N_d decreased significantly during this annealing. $[H_T]$ and N_d then remained constant for at least ~ 100 hrs at 180°C and ~ 30 hrs at 225°C. During prolonged annealing beyond these periods, $[H_T]$ decreased by evolution of hydrogen from $Si-H_2$ and $Si-H_3$ bonding configurations. However, the ratio I(2100)/I(2000) of the integrated intensity of the 2100 cm^{-1} to the 2000 cm^{-1} stretch modes, with the latter being the dominant peak, did not change beyond the 30% margin of error during the entire annealing procedure.

It is interesting to compare these observations with recent IR results of Fritzsche and Deng[88] on various gd films annealed for moderate periods at 220°C. They reported that in boron-doped films, some hydrogen irreversibly converts <u>from</u> bulk mono-H <u>to</u> $Si-H_2$ and $Si-H_3$ configurations during annealing at 220°C. Although no emergence of a bond bending scissors mode was observed in n-type films, the stretch

peak at 2100 cm^{-1} did increase. These processes were faster in p-type films (< 20 hrs) than in n-type-doped films. Thus, even moderate annealing of these doped gd films resulted in changes in the Si network consistent with the rise in the microvoid related hydrogen content. Since hydrogen diffusion is most rapid in p-type films, slower in n-type films, and slowest in undoped films, it appears to be controlling the above changes and the consequent evolution of the Si network. Like their undoped counterparts, N_d in the boron doped rf sputtered films decreased during the initial annealing steps at each temperature. This behavior may be intrinsic to rf sputtered films since the plasma-film interaction is significant. Also in sample 37, the intensity of the 840 - 890 cm^{-1} bond bending scissors mode, characteristic of microvoids, was significant. The gd films were apparently device quality containing few microvoids as deposited.

The observation that I(2100)/I(2000) does not change beyond a 30% margin of error is considered to be significant. It indicates that most of the contribution to the peak at 2100 cm^{-1} is due to mono-H bonds at the surfaces of large microvoids (radius $\geq$ 2Å), rather than to $Si-H_2$ and $Si-H_3$ configurations. It does not, however, mean that the distribution of hydrogen among bulk sites and voids of various sizes is largely unchanged: A hydrogen atom moving from the bulk site to the surface of a "compact" microvoid would still yield a stretch vibration frequency of 2000 cm^{-1}.[62] Even the distribution of hydrogen from bulk or compact voids on one hand, and large microvoids on the other hand, is qualitative only, since the oscillator strength varies with the size of the void around the hydrogen atom.[64,83] Thus, although the 2000 cm^{-1}

dominates the stretch band, it only suggests that a significant fraction of hydrogen atoms is either bonded in the bulk or on compact microvoid surfaces.

No deviation from the power-law time dependence (Eq. 4.6) had been previously reported. Results of prolonged annealing extending up to 500 hrs at 275°C on undoped samples, described earlier in the chapter, show no departure from Eq. (4.6). The sharp rise in $\Theta(t)$ during the annealing beyond ~ 50 hrs at 180°C (Fig. 4.27) and ~ 30 hrs at 225°C (Fig. 4.28) is thus unprecedented. Indeed, during some period of this of this second stage, the slope $(1 - \alpha)$ of the $\log_{10}\Theta$ vs $\log_{10}t$ plot appears to be larger than unity. Eq. (4.6) would then imply that $\alpha < 0$, and that D(t) increases with time (Eq. 1.3). Although this extraordinary behavior cannot be ruled out, the current results are insufficient to firmly establish it. These results, however, do indicate that α is not significantly greater than zero. D(t) is then roughly constant during this period. A constant D(t) may indicate that the hydrogen atoms may have reached the bottom of the trapping distribution following the initial dispersive motion in the relaxing network. We note, however, that the high value of α in both the first and third stages of annealing indicates strong effects of microvoids. Thus the transition between these stages is believed to involve structural relaxation processes which rearrange the microvoid system. During this period, as the structure relaxes, some of the immobile hydrogen trapped in deep microvoid related sites is released and become relatively mobile. This results in a rapid rise of $\Theta(t)$. Following these processes, the system reaches a quasiequilibrium state, i.e., a

local minima in configuration space. The diffusion of hydrogen may then become nearly quenched, if most of the hydrogen atoms reoccupy deep microvoid related sites. Recent results on moderately annealed boron-doped gd films suggests that a consequence of structural relaxations of the Si network is an increase in the doping efficiency.[89] Since hydrogen diffusion increases with the doping level,[38] the rapid rise in $\Theta(t)$ in the second stage of annealing may, in part, be related to changes in the doping efficiency. In that case the time dependent diffusion constant $D(t)$ would indeed be expected to increase with time (i.e., $\alpha < 0$).

Recent theoretical work by Chang and Chadi[90] on hydrogen diffusion in c-Si has suggested the dissociation of hydrogen complexes (H_2^*) as a mechanism of hydrogen diffusion. Jackson[91] has extended this idea to hydrogen diffusion in a-Si:H. One of the important points made by these authors is that the charge of the diffusing species is positive, negative, or neutral, if the material is p-type, n-type, or undoped, respectively. It is obvious that biased annealing experiments on doped material are needed to check the validity of the H_2^* dissociation model.

D. Concluding Remarks

In this work we studied long range hydrogen motion in undoped and boron-doped a-Si:H with varying microstructure. The results indicate that microvoids play an important role in the diffusion process. It has been shown convincingly that an excess of microvoids quench the diffusion entirely even though a large fraction of the hydrogen reside in mono Si-H bulk sites or on "compact" microvoid surfaces.

It is clear from this work that there are at least two different types of hydrogen trapping sites. One class of sites are relatively shallow and may roughly be exponentially distributed in energy. As hydrogen diffuses, it samples deeper and deeper sites which then give rise to a diffusion constant which decreases with time. The measured activation energy E_{diff} is then the depth of the deepest site visited by the migrating hydrogen atom. Hence E_{diff} is expected to increase as the diffusion length increases (Table IX). Also E_{diff} decreases (at constant diffusion length) as the total hydrogen content increases. However, the value of the exponent α also generally decreases with $[H_T]_o$ suggesting that in hydrogen migration in the hydrogen poor samples is dominated by the multiple trapping transport of hydrogen among the deeper sites of the distribution.

The other class of sites are the microvoid-related deep trapping sites for hydrogen. Though the nature of these sites is still not well established, evidence from this work points to multivacancies with largely unhydrogenated surfaces. Once hydrogen atoms are trapped in these sites they become relatively immobile and thus the value of α increases. However, rearrangement of these microvoids upon annealing, as in boron-doped samples, may release the trapped hydrogen which then becomes relatively mobile.

This scenario also explains the drastic reduction of the ESR signal during initial annealing. In the hydrogen rich samples, a small fraction of the hydrogen remains trapped in interstitial sites. Upon annealing, these atoms migrate quickly and are trapped in these multivacancies resulting in a decrease in the ESR signal. It should be

noted that hydrogen in c-Si diffuses via intersitial sites with a relatively low activation energy of 0.5 eV.[92] It has been shown that as the quality of gd deposited films deteriorates, both the size and number of clustered hydrogen (and hence multivacancies) increases.[67] This, then, may explain the observation that the drop in the ESR signal upon annealing above 300°C is seen only in "non-device quality" a-Si:H and is irreversible.[36] In device quality material, the ESR signal will actually increase if the film is rapidly quenched from temperatures above ~300°C.[36]

Although the results presented in this chapter are better understood within the multiple trapping transport of hydrogen, the floating bond model, however, cannot be ruled out. The results, however, cast serious doubts regarding the validity of the "Hydrogen Glass Model" (see Chapter I). To be describable as a glass, the hydrogen in a-Si:H must satisfy two key conditions.[93] First, the equilibration of excess charge carriers must be caused by the motion of hydrogen. Second, most of the hydrogen, and not just a small subset residing in special sites, must be involved in the equilibration process. Though this work does not address the first issue, it does provide an answer for the second issue. It is clear that some hydrogen remains trapped in microvoid related deep trapping sites and does not take part in the diffusion process. Hence, these hydrogen atoms probably do not contribute significantly to the electronic relaxation processes.

Questions still remain on the role of boron in boron-doped films. Prolonged annealing on boron-doped a-Si:H, unlike undoped material, has exhibited a marked departure of the diffusion from the power-law time

dependence. Open question on how structural relaxation, which is thought to be the origin of this extraordinary behavior, depends on the boron content. It is not clear at this time if the microvoids affect the relaxation of the silicon network. Obviously, more studies are required to address these important issues. These should obviously include studies of hydrogen diffusion in n-type and compensated films.

V. REFERENCES

1. D. Adler, Amorphous Semiconductor for Microelectronics, D. Adler editor, Proc. SPIE 617, v (1986), Introduction.

2. A. P. Thakoor, Bull. Am. Phys. Soc. 33, 343 (1988).

3. G. C. Chittick, J. H. Alexander, and H. F. Sterling, J. Electrochem. Soc. 116, 77 (1969).

4. W. E. Spear and P. G. LeComber, Solid State Commun. 17, 1193 (1975).

5. W. Paul, A. J. Lewis, G. A. N. Connell, T. D. Moustakas, Solid State Comm. 20, 969 (1976).

6. C. Kittel, Introduction to Solid State Physics (Wiley, New York, 1976).

7. R. J. Temkin, W. Paul, and G. A. N. Connell, Adv. Phys. 22, 581 (1973).

8. P. W. Anderson, Phys. Rev. 109, 1492 (1958).

9. N. F. Mott and E. A. Davis, Phil. Mag. 17, 1269 (1968).

10. S. T. Pantelides, Phys. Rev. Lett. 57, 2979 (1986); Phys. Rev. Lett. 13, 1344 (1987).

11. P. C. Kelires and J. Tersoff, Phys. Rev. Lett. 61, 562 (1988).

12. S. T. Pantelides, Phys. Rev. B 36, 3479 (1987).

13. Y. Bar-Yam, D. Adler, and J. D. Joannopoulos, Phys. Rev. Lett. 57, 467 (1986).

14. R. Biswas, G. S. Grest and C. M. Soukoulis, Phys. Rev. B 36, 7437 (1987).

15. A. Matsuda, M. Matsumura, K. Nagiakgaqwa, T. Imura, H. Yamanoto, S. Yamusaki, H. Okushi, S. Iizima, and K. Tananaka, in Tetrahedrally Bonded Amorphous Semiconductors, edited by R. A. Street, D. K. Biegelson, and J. C. Knights (American Institute of Physics, New York, 1981), p. 192.

16. S. Zhao and S. Hunklinger, Solar Energy Mater., 6, 233 (1982).

17. G. D. Cody, T. Tiedje, B. Abeles, T. D. Moustakas, B. Brooks, and Y. Goldstein, J. De Physique 42(C4), 301, (1981).

18. M. Albers, Ph.D. Thesis, Iowa State University, (1987) unpublished.

19. R. C. Ross and R. Meisser, J. Appl. Phys. 52, 8 (1981).

20. R. Meisser and R. C. Ross, J. Appl. Phys. 53, 9 (1982).

21. J. C. Knights and R. A. Lujan, Appl. Phys. Lett. 35, 244 (1979).

22. J. A. Reimer, R. W. Vaughn, and J. C. Knights, Phys. Rev. Lett. 44, 193 (1980).

23. D. L. Staebler and C. R. Wronski, Appl. Phys. Lett. 31, 292 (1977).

24. M. Stutzmann, W. B. Jackson, and C. C. Tsai, Phys. Rev. B 32, 6062 (1985).

25. N. B. Goodman, Philos. Mag. B 45, 407 (1982).

26. M. Grunewald, K. Weber, W. Fuhs, and P. Thomas, J. Phys. (Paris) Colloq. 42, C4-523 (1981).

27. D. V. Lang, J. D. Cohen, J. P. Harbison, and A. M. Sergent, Appl. Phys. Lett. 40, 474 (1982).

28. J. I. Pankove and J. E. Berkeyheiser, Appl. Phys. Lett. 37, 705 (1980).

29. N. M. Amer, A. Skumanich, and W. B. Jackson, Physica (Utrecht) 117 & 118B 897 (1983).

30. I. Hirabayashi, K. Morigaki, and S. Nitta, Jpn. J. Appl. Phys. 19, L357 (1980).

31. H. Dersh, J. Stuke, and J. Beichler, Appl. Phys. Lett. 38, 456 (1980).

32. D. Adler, M. E. Eberhart, K. H. Johnson, and S. A. Zygmunt, J. Non-Cryst. Solids 66 273 (1984).

33. R. S. Crandall, D. E. Carlson. A. Catalano, and H. A. Weakliem, Appl. Phys. Lett. 44 200 (1984).

34. K. Morigaki, Jpn. J. Appl. Phys. 27 163 (1988).

35. D. E. Carlson, Appl. Phys. A 305 (1986).

36. R. A. Street and K. Winer, Phys. Rev. B 40 6236 (1989).

37. G. Muller, S. Kalbitzer, and H. Mannsperger, Appl. Phys. A 39 243 (1986).

38. R. A. Street, C. C. Tsai, J. Kakalios, and W. B. Jackson, Phil. Mag. B 56, 305 (1987).

39. J. Kakalios, R. A. Street, and W. B. Jackson, Phys. Rev. Lett. 59, 1037 (1987).

40. W. B. Jackson, Phys. Rev. B 38, 3595 (1988).

41. W. B. Jackson and J. Kakalios, Phys. Rev. B 37, 1020 (1988).

42. J. Shinar, R. Shinar, S. Mitra, and J. Y. Kim, Phys. Rev. Lett. 62, 2001 (1989).

43. R. Kirchheim and X. Y. Huang, Phys. Status Solidi (b) 144, 253 (1987).

44. M. Stutzman and D. K. Biegelson, Phys. Rev. Lett. 60, 1682 (1988).

45. J. H. Stathis and S. T. Pantelides, Phys. Rev. B, 37, 6567 (1988).

46. W. B. Jackson, C. C. Tsai, and R. Thompson, Phys. Rev. Lett. 64, 56 (1990).

47. T. D. Moustakas, J. Electronic Mat. 8, 391 (1979).

48. T. D. Moustakas, T. Tiedje, and W. A. Lanford, in Tetrahedrally Bonded Amorphous Semiconductors, edited by R. A. Street, D. K. Biegelson, and J. C. Knights, (AIP Conference Proceedings no.73, p. 20, 1981)

49. T. D. Moustakas, Solar Energy Mater. 8, 187 (1982).

50. D. W. Anderson, G. Moddel, M. A. Paesler, and W. Paul, J. Vac. Sci. Tech. 16, 906 (1979).

51. H. S. Wu, Ph.D. Thesis, Iowa State University, (1988) unpublished.

52. J. Shinar, S. Mitra, and H.-S. Wu, Optical Materials Technology for Energy Efficiency and Solar Energy Conversion VII, C. G. Granqvist and C. M. Lampert, eds., Proc SPIE 1016, 115 (1988).

53. W. Paul and D. W. Anderson, Solar Energy Mater. 5, 229 (1981).

54. R. A. Rudder, J. W. Cook, and G. Lucovsky, Appl. Phys. Lett. 43, 871 (1983).

55. R. A. Rudder, J. W. Cook, and G. Lucovsky, Appl. Phys. Lett. 45, 887 (1984).

56. J. I. Pankove, Optical Processes in Semiconductors (Dover, New York 1971).

57. J. Tauc, R. Grigorovicci, and A. Vancu, in Amorphous and Liquid Semiconductors, edited by J. Tauc (Plenum, New York, 1974).

58. G. D. Cody, Mat. Res. Soc. Symp. Proc. **192**, 113 (1990).

59. H. R. Park, J. Z. Liu, P. R. Cabarrocas, A. Maruyama, M. Isomura, S. Wagner, J. R. Abelson and F. Finger, Mat. Res. Soc. Symp. Proc. **192**, 751 (1990).

60. M. H. Brodsky, M. Cardona, and J. J. Cuomo, Phys. Rev. B **16**, 3556 (1977).

61. H. R. Shanks, C. J. Fang, L. Ley, M. Cardona, F. J. Demond, and S. Kablitzer, Phys. Status Solidi (b) **100**, 43 (1980).

62. A. H. Mahan, D. L. Williamson, B. P. Nelson, and R. S. Crandall, Phys. Rev B **40**, 12024 (1989).

63. H. R. Shanks, F. R. Jeffrey, and M. E. Lowry, J. de Physique **42**, C4-773 (1981).

64. M. Cardona, Phys. Status Solidi (b) **118**, 463 (1983).

65. H. Wagner and W. Beyer, Solid State Commun. **48**, 585 (1983).

66. J. Baum, K.K. Gleason, A. Pines, A. N. Garroway, and J. A. Reimer, Phys. Rev. Lett. **56**, 1377 (1986).

67. K. K. Gleason, M. A. Petrich, and J. A. Reimer, Phys. Rev. B **36**, 3259 (1987).

68. G. Lucovsky, R. J. Nemanich, and J. C. Knights, Phys. Rev. B **19**, 2064 (1979).

69. M. H. Brodsky and R. S. Title, Phys. Rev. Lett. **23**, 581 (1969).

70. R. A. Street and D. K.Biegelsen, in Physics of Hydrogenated Amorphous Silicon II, edited by J. D. Joannopoulos and G. Lucovsky (Springer-Verlag, New York, 1984) Vol. 56, p. 199.

71. P. J. Caplan, E. H. Poindexter, B. E. Deal, and R. R. Razouk, J. Appl. Phys. **50**, 5847 (1979).

72. R. A. Street, D. K. Biegelson, and J. D. Zesch, Phys. Rev. B **25**, 4334 (1982).

73. S. Hasegawa and S. T. Yazaki, Thin Solid Films **55**, 15 (1978).

74. C. P. Poole, Jr., in Electron Spin Resonance, 2nd Ed. (Wiley, New York, 1983), p. 409.

75. D. G. Welkie, Secondary Ion Mass Spectrometry, SIMS IV, A. Benninghoven et al., eds. (Springer, Berlin, 1984), p. 296.

76. R. G. Wilson, F. A. Stevie, and C. W. Magee, in Secondary Ion Mass Spectrometry: A Practical Handbook for Depth Profiling and Bulk Impurity Analysis (Wiley, New York, 1989), p. 2.1-1.

77. W. Vandervorst and F. R. Shepherd, J. Vac. Sci. Technol. A5, 313 (1987).

78. D. E. Carlson and C. W. Magee, Appl. Phys. Lett. 33, 81 (1978).

79. P. G. Shewmon, Diffusion in Solids (McGraw Hill, New York, 1963) p. 6.

80. J. Crank, Mathematics of Diffusion (Claredon, Oxford, England, 1975) Chap. 2.

81. R. Biswas, I. Kwon, A. M. Bouchard, C. M. Soukoulis, and G. S. Grest, Phys. Rev. B 39, 5101 (1989).

82. M. Albers, J. Shinar, and H. R. Shanks, J. Appl. Phys. 64, 1859 (1988).

83. M. J. Thompson, in The Physics of Hydrogenated Amorphous Silicon I, edited by J. D. Joannopoulos and G. Lucovsky (Springer-Verlag, New York, 1984) Chap. 4.

84. X. -M. Tang, J. Weber, Y. Baer and F. Finger, Phys. Rev. B 41, 7945 (1990).

85. J. Shinar, R. Shinar, X. -L. Wu, S. Mitra and R. F. Girvan, Phys. Rev. B (in press).

86. M. Zheng, E. J. VanderHeiden, P. C. Taylor, R. Shinar, S. Mitra, and J. Shinar, in Amorphous Silicon Technology - 1990, edited by P. C. Taylor, Y. Hamakawa, M. J. Thompson, A. Madan, and P. G. LeComber, Mat. Res. Soc. Symp. Proc. (Pittsburgh, PA) 192, 657, (1990).

87. W. Beyer, H. Wagner, and H. Mell, Solid State Commun. 39, 375 (1981).

88. H. Fritzsche and X. -M. Deng, Bull. Am. Phys. Soc. 35, 349 (1981).

89. X. -M. Deng, Phys. Rev. B (submitted).

90. K. J. Chang and D. J. Chadi, Phys. Rev. Lett. 62, 937 (1989); Phys. Rev. B 40, 11644 (1989).

91. W. B. Jackson, Phys. Rev. B 41, 10257 (1990).

92. D. Shaw, Atomic Diffusion in Semiconductors (Plenum, London, 1973) p.217.

93. J. Kakalios and W. B. Jackson, Advances in Amorphous Semiconductors, edited by H. Fritzsche (World Scientific, Singapore, 1989) p. 208.

VI. ACKNOWLEDGEMENTS

I would like to express my gratitude and thanks to those who have helped me in this work.

I would like to thank my thesis advisor Dr. Joseph Shinar for his guidance, encouragement and patience during the course of this work. Thanks are also due to Dr. Ruth Shinar for both her work on the SIMS and the invaluable discussions. I am also very grateful to Dr. Goldman, Dr. Ho, Dr. Hsieh, and Dr. Lewis for serving on my committee. I would also like to acknowledge the stimulating discussions I had with Dr. Rana Biswas over the past few years.

I would also like thank my mother for always encouraging me to do my best and my wife Mahua for her love and support. Finally, I would like to thank are all my friends and colleagues for making my stay at Ames memorable.

DISCLAIMER

Printed in the United States of America

Available from
National Technical Information Service
U.S. Department of Commerce
5265 Port Royal Road
Springfield, VA 22161